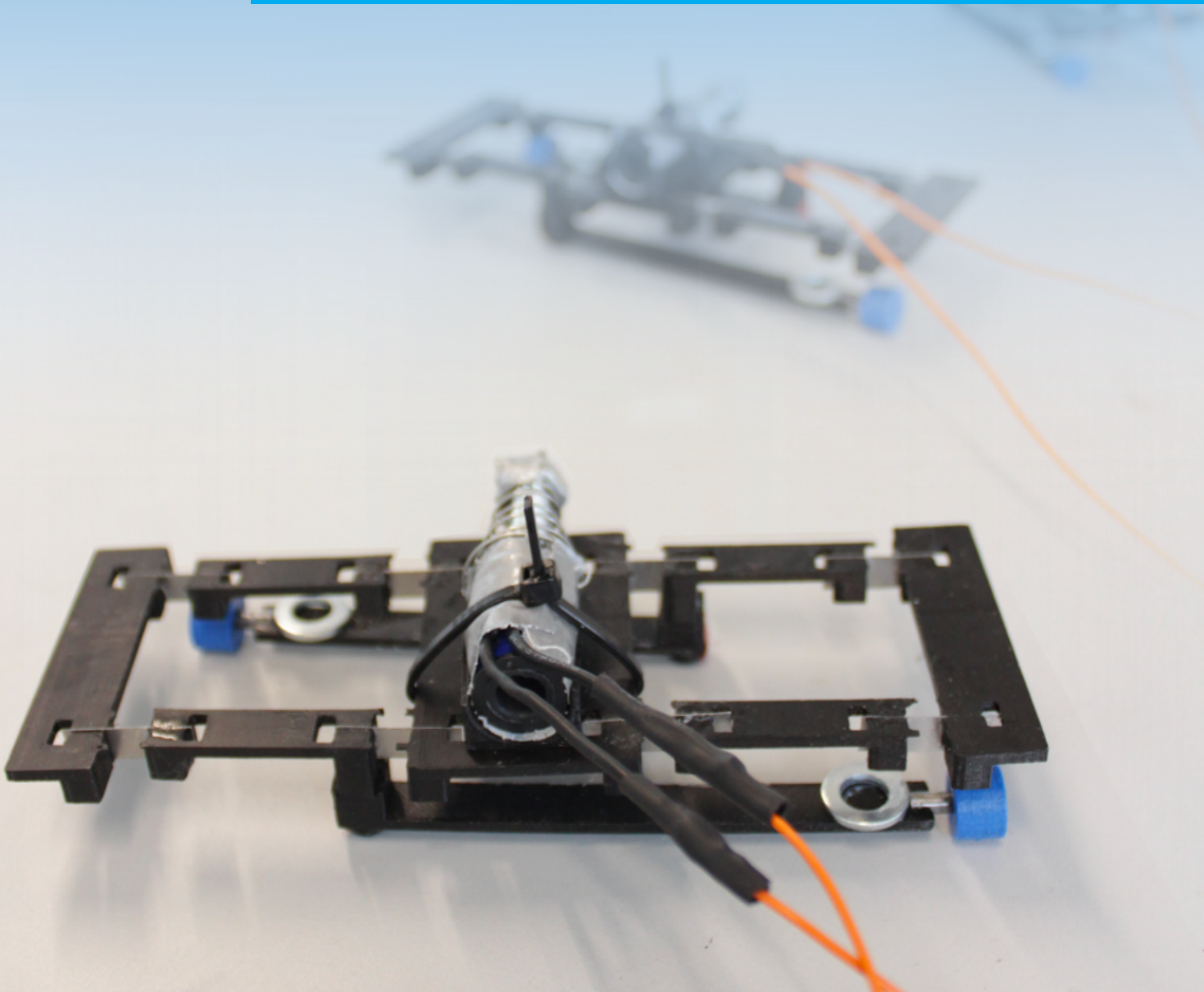


Department of Precision and Microsystems Engineering

Underactuated Compliant Resonant Walking Robot with Steering Mechanism

C.S. Lemmens

Report no : 2023.057  
Coach : Dr.ir G. Radaelli  
Professor : Prof.dr.ir J.L. Herder  
Specialisation : Mechatronic System Design  
Type of report : Master of Science Thesis  
Date : 11 September 2023





# Underactuated Compliant Resonant Walking Robot with Steering Mechanism

Thesis report

by

C. S. Lemmens

to obtain the degree of Master of Science  
at the Delft University of Technology  
to be defended publicly on September 11, 2023 at 13:00

*Thesis committee:*

Chair: Prof.dr.ir J.L. Herder  
Supervisor: Dr.ir G. Radaelli  
External examiner: Dr. S.H. Hossein Nia Kani  
Place: Faculty of Mechanical, Maritime and Materials Engineering (3mE), Delft  
Project Duration: September, 2022 - September, 2023  
Student number: 4720539

An electronic version of this thesis is available at <http://repository.tudelft.nl/>.



Copyright © Department of Precision and Microsystems Engineering (PME)  
All rights reserved.

# Preface

Before I started the Master's program in High-Tech Engineering, I was really excited to begin. However, I did not enjoy the first year of the program as much as I had expected. I did like the theoretical courses, but the projects left me a bit disappointed. I think this dissatisfaction with the projects was due to the Covid-19 restrictions. The part I enjoyed the most during the projects was interacting with fellow students/friends and bringing designs to life, both of which were tough with the restrictions. In that same year, I was a board member of D.S.W.Z. Broach, which also required a lot of determination due to the Covid-19 restrictions. However, being on the board filled the gap of not being able to interact with friends and work on ideas.

The second year of the Master's program was much better. It mostly involved finishing first-year courses, and at the end of the year, I had enough time to go on a three-month road trip through Europe with my girlfriend in a campervan.

After the road trip, I was eager to start a thesis project. The FARbot project caught my attention because in the first-year course Engineering Dynamics, we had to calculate the eigenmodes of the FARbot. I had a lot of fun in that course, so when I found out the project was continuing, I reached out to Giuseppe right away. When I learned that the project was still available, I got really excited since the project included the parts of engineering that I enjoy the most: designing and building.

Giuseppe mentioned that the project could be focused on further miniaturisation or the implementation of a steering mechanism. The steering mechanism got my interest; it seemed like a good way to contribute to the project and add more functionality. Plus, it sounded like a great challenge (which it definitely was). I am very proud to present a physical robot that meets the requirements. The last year was really enjoyable. I ended up loving the thesis project even more than I initially thought I would.

Enjoy reading!

*C. S. Lemmens*  
*Delft, September 2023*



# Acknowledgements

First I would like to thank my supervisor Giuseppe. His well-structured critique helped a lot to increase the level of the work. He was always available when I was stuck or had trouble with something and had a lot of creative input. I enjoyed working together.

Furthermore, I would like to thank the people from the PME Lab support. I want to thank them for the time and knowledge they invested in my project.

I would like to thank the other members of the graduation committee, Just and Hassan, for being part of the committee and for their time.

Moreover, I would like to thank the proofreaders for their time and work to increase the level of my thesis.

Finally, I would like to thank my family and friends for all the support during the last year. I really enjoyed the conversation about the project and appreciate all the input and ideas.

*C. S. Lemmens  
Delft, September 2023*



# Summary

This thesis report presents research on small walking robots. The report begins with an introduction that explains the project's origin, outlines the project's goal, and provides an overview of the report's contents. Following the introduction, a literature study is conducted to investigate the current state-of-the-art steering mechanisms for walking robots.

After the literature study, the research paper is presented, detailing the design process and the robot's performance results. The paper demonstrates the successful design of a frequency-actuated resonance robot with both forward locomotion and steering capabilities, achieved by using only one actuator.

In conclusion, the literature study provides a novel classification and overview of state-of-the-art walking robots. Furthermore, the research paper showcases the successful design of a frequency-actuated resonance robot with a forward locomotion and steering mechanism, all accomplished with the use of a single actuator.



# Contents

<b>Preface</b>	<b>ii</b>
<b>Acknowledgements</b>	<b>iv</b>
<b>Summary</b>	<b>vi</b>
<b>1 Introduction</b>	<b>1</b>
1.1 Idea behind the FARbot-s . . . . .	1
1.2 Goal of literature study . . . . .	1
1.3 Goal of thesis research . . . . .	1
1.4 Overview of report . . . . .	2
<b>2 Literature</b>	<b>3</b>
<b>3 Research paper</b>	<b>19</b>
<b>4 Conclusion</b>	<b>37</b>
<b>A Simulink and generalised stiffness</b>	<b>39</b>
<b>B Friction and voltage experiments</b>	<b>41</b>
B.1 Methodology . . . . .	41
B.2 Results . . . . .	43
B.3 Discussion . . . . .	46
B.4 Conclusion . . . . .	46
<b>C Parameter optimisation</b>	<b>47</b>
<b>D Other designs</b>	<b>51</b>
<b>E Steering analysis</b>	<b>53</b>
<b>F Extra experimental results</b>	<b>55</b>
F.1 Additional trajectory experiments . . . . .	55
F.2 Time response of physical model . . . . .	56
<b>G Equivalent mass calculation</b>	<b>57</b>



# 1

## Introduction

In this chapter, the research which was performed during the thesis is introduced. The chapter starts with the idea behind the project and is followed up by the introduction of the two papers which are presented in chapter 2 and chapter 3. Finally, an overview of the report is provided.

### 1.1. Idea behind the FARbot-s

FARbot, a Frequency Actuated Resonant robot, is a running robot previously developed by Johan Schonebaum[1]. The robot is designed to have its whole-body vibration eigenmode correspond to the motion required to run. By utilising two solenoid actuators that stimulate the system at the appropriate eigenfrequency, the robot achieves efficient and swift movement without the requirement for intricate control mechanisms. Additionally, this robot is constructed as a monolithic compliant mechanism, indicating that all components, excluding the actuators and electronic elements, are crafted from a single uninterrupted material piece.

The research on the FARbot led to many open challenges to increase its performance. The research conducted on the FARbot lead to many open challenges to improve the performance of the robot. The two main limiting factors for further miniaturisation are the size and weight of the solenoid actuators and the stiffness of the compliant hinges, which is limited by the smallest manufacturable thickness of the leaf flexures. With regards to the potential applications of this robot, it lacks manoeuvrability and a way to control the speed. Finally, the current feet are unable to provide the traction forces to actually propel itself.

Because of the enormity of these challenges, the focus of this thesis is increasing manoeuvrability and speed control. An additional goal is to provide a method for the robot to propel itself. This led to the goal of the literature research: a study on steering mechanisms for walking robots.

### 1.2. Goal of literature study

The purpose of the literature study is to provide an overview of different methods for small walking robots, to show the existing steering mechanisms and concepts which can be used as steering mechanisms, to show the non-existing steering mechanisms, and to give an overview of the important properties of steering mechanisms. The important properties interesting for a new design were: size, is a smaller design possible, amount of actuators and amount of actuators used for steering.

Based on the result of the literature study it was chosen to design a small frequency actuated resonant walking robot which is able to propel itself and has a steering mechanism while only having one actuator. This kind of design is novel in the research field. With the upcoming of small walking robots, a simplistic design with the same functionality would be innovative.

### 1.3. Goal of thesis research

The decision of designing a frequency-actuated resonance walking robot with only one actuator while still maintaining the function of being able to propel itself and able to steer led to two main challenges. Firstly, designing a forward locomotion mechanism to propel the robot with one actuator. Secondly,

designing a steering mechanism which is able to function using the same actuator used for the forward locomotion mechanism. This led to the goal of the thesis project: Design a forward locomotion and steering mechanism for a small compliant resonant walking robot without the addition of extra actuators.

## 1.4. Overview of report

Chapter 2 contains the literature study of the thesis. Chapter 3 contains the research paper. In the research paper the design of the FARbot-s is shown and design choices are explained. The paper also shows the performance of the FARbot-s and how it compares to walking robots of similar size. The supplementary material contains all the research which did not fit into the research paper. In Appendix A the Simulink model is shown together with the Matlab script to calculate the generalised stiffness matrix. In Appendix B the study into the influence of friction and voltage on the FARbot-s model is presented. Appendix C contains a more results of the parameter optimisation. In Appendix D other kinematic designs are presented. In Appendix E additional results of the steering mechanism results are shown. In Appendix F additional experimental results of the FARbot-s are shown. Finally, in Appendix G the mass calculation for the solenoid model is explained.

# 2

## Literature

In this chapter, the literature paper is presented. The goal of the paper is to give a complete overview of existing steering mechanisms for small walking robots.

# Literature Study on Steering Mechanisms for Walking Robots

C.S. Lemmens

4720539

C.S.Lemmens@student.tudelft.nl

**Abstract** The control of mobile walking robots is key to their usability and versatility. One of the most important aspects of controlling a robot is the steering function. Based on their physical principles, six subcategories of steering mechanisms are categorised in this paper. It provides examples of existing steering mechanisms for these subcategories found in the literature. Additionally, non-existent conceptual steering strategies are presented, and a general overview of all the steering mechanisms is provided. This overview shows the important properties of small walking robots. This paper can be used as an aid to design a steering mechanism for a small walking robot.

## 1 Introduction

Small walking robots with a steering mechanism have been researched, developed and designed for about twenty years [1]. There is a large interest in these robots, because of their possibilities. Their size makes them great for exploring tight, narrow, and hazardous areas. The small actuators make that they have low energy consumption, and the low mass-to-body size ratio makes them durable and robust [2].

However, to have a robot carry out these tasks, control of the robot is very important. Control of the robot gives it the possibility to choose its direction and path [3]. A fundamental part of a robot's control is the steering mechanism. Without it, a change of direction would not be possible. Moreover, the robot can not be large as the purpose of the robot is to fit into tight and narrow places. Furthermore, the complexity of the robot is important. The complexity of a robot is determined by the amount of actuators and other parts, the fabrication and assembly time, and therefore ultimately the costs.

Prior to this paper, a literature review and classification of mobile robots has been made by J.K. Schonebaum et al. [2]. A literature review on the steering mechanisms of jumping robots has been done by M. Kovac et al. [4]. N.J. Kohut et al. [5] compares their steering mechanism to some other mechanisms. The paper of A.O. Pullin et al. [6] shows an overview of small dynamic-legged robots with a steering mechanism. The paper of A.O. Pullin et al. is similar to this paper. However, in this literature study, the overview includes more steering mechanisms, conceptual steering mechanisms, and steering mechanisms which are currently not used in walking robots.

The definition of steering according to Merriam-Webster's dictionary, is: "to control the course

of [7]". The course can be changed by the use of a steering mechanism. The mechanism is used to create an asymmetry within the robot's actuation. The asymmetry causes the robot to steer.

The purpose of this paper is to provide an overview of different methods for small walking robots, to show the existing steering mechanisms and concepts which can be used as steering mechanisms, to show the non-existing steering mechanisms, and to give an overview of the important properties of steering mechanisms. For small walking robots, the conventional biggest dimension is between 50 mm and 500 mm. The research method and characterization of steering mechanisms is provided in Chapter 2. The results of the research are presented in Chapter 3 and 4. The non-existing steering mechanisms and overview of important properties is given in Chapter 5. In Chapter 6 the conclusion will be drawn.

## 2 Methods

In this chapter, the characterisation of steering mechanisms and the research method is presented.

The characterisation of steering mechanisms is shown in a tree structure and can be found in Figure 1. This classification distinguishes between steering with the legs and steering with an added mechanism which is actuated separately from the legs. The second division is based on the physical principle of what is changed to steer. For simplification, these are called basic physical principles (BPP). The third division is the different steering mechanisms. The BPP are described below:

- **Internal displacement:** A change in the leg step size in the horizontal plane.
- **Internal force:** A change of the force between the body and legs or legs and ground.
- **Internal velocity:** A change in the velocity of the leg's movement.
- **Added displacement:** A change in the horizontal plane with the use of something other than the walking legs.
- **Added force:** A change of force exerted on the robot by the use of the added mechanisms.
- **Added velocity:** A change in velocity of the added mechanism which causes the robot to steer.

To carry out the literature study of this paper, a combination of search terms was used. These

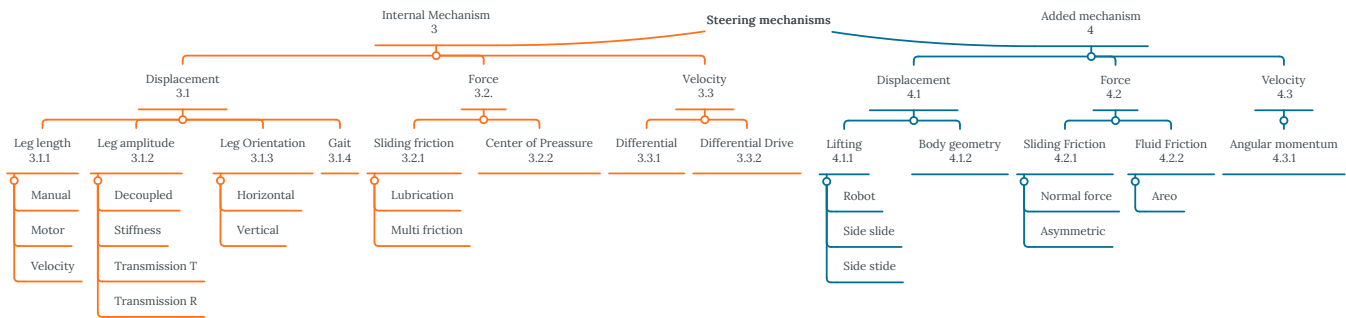


Figure 1: Tree diagram of steering mechanisms for walking robots. The first division distinguishes the mechanisms which use the legs to steer or an added mechanism to steer. The second division is based on the basic physical principles (BPP). The third division is based on the method on how the BPP is changed. The numbers underneath each division indicates the chapter or section.

combinations consist of synonyms displayed in Table 1. Each column contains synonyms and the terms from each of these three columns were combined in this research. The search terms have been carried out on Scopus, Google Scholar, the online TU Delft library, and the TU Delft repository. The results of the literature study are presented in Chapter 3 and 4. The chapters are divided into sections based on the second division of the tree structure, see Figure 1.

Table 1: Search terms for literature search.

AND			
	Mobile robot	Steering	Milli
OR	Walking robot	Turning	Miniature
	Jumping robot	Rotating	Small

### 3 Internal mechanisms

In this chapter the internal steering mechanisms are presented. The internal displacement, force and velocity are presented in Sections 3.1, 3.2, and 3.3, respectively.

#### 3.1 Displacement

The steering mechanisms which change leg step in the horizontal plane to steer, are categorised under the section Displacement. The step can either be smaller or larger in the forward direction or translated in the lateral direction. By changing the contact point of the leg or the leg amplitude an asymmetry between the left and the right side is created within the locomotion of the robot. The asymmetry causes the robot to turn.

The mechanisms can be categorised by the method on how they change the BPP. The methods are the change of leg length, the change of leg orientation, the change of step amplitude, and a change of gait. These steering methods are presented in Section 3.1.1, 3.1.2, 3.1.3 and, 3.1.4, respectively.

##### 3.1.1 Leg length

Under section 3.1.1 the mechanisms change the leg length to steer. The mechanisms create an asymmetry by

changing the leg length of the walking robot. By changing the leg length on one side of the robot, the side with the longer legs has a larger step size. Thus, this side will displace more than the side with the shorter leg length, causing the robot to turn.

There are three distinct methods to change the leg length: manually, with a motor, and with a change in velocity. These methods are discussed in the following paragraphs.

**Manual** The most obvious method to change the leg length is by swapping the legs. By simply swapping one side of the robots' legs for shorter or longer legs it can turn. Despite the simplicity of this steering mechanism it has not been used by scholars and therefore, has not been found in literature.

**Motor** With the use of an actuator the leg length can also be varied. The actuator can be used to make the legs longer or shorter depending on which side the robot needs to turn. There is no literature found of a walking robot which steers by changing its leg length with a motor.

**Velocity** Perhaps a less obvious method to change the leg length is by a change in velocity. Such a robot would have compliant legs with a certain stiffness and mass at the location of the feet. Under a certain velocity the mass at the feet will undergo a centrifugal force higher than the spring force. At this velocity the leg length will become longer. If these compliant legs are only at one side of the robot, the legs are asymmetric under a certain velocity. This steering mechanism is not found in literature.

##### 3.1.2 Step amplitude

Changing the step amplitude on one side of the robot causes this side to move less or more, resulting in a rotation. Steering by changing the step amplitude has been achieved in four different ways. The step amplitude can be changed by changing the stiffness in a joint, having decoupled sides, a translational transmission or a rotational transmission.

**Stiffness joint** By introducing stiffer joints in the connection between the robot's body and legs, a steering motion can be induced. The stiffer joints need to be applied asymmetrically. The robot of D. Zarrouk and S. Ronals [8] uses this as a steering mechanism, see Figure 2. The robot steers by accelerating and decelerating. Since the stiffness of the joints is asymmetric, the amplitude of the step size on one of the sides is shorter, causing the robot to rotate to the side of the stiffer joint. The robot legs are not tunable during movement, so the joints are swapped manually if a turn in the other direction is desired. The robot by D. Zarrouk and S. Ronals is only a mathematical model of the robot, there is no prototype. The amount of actuators and the size of this robot is not mentioned in the paper.

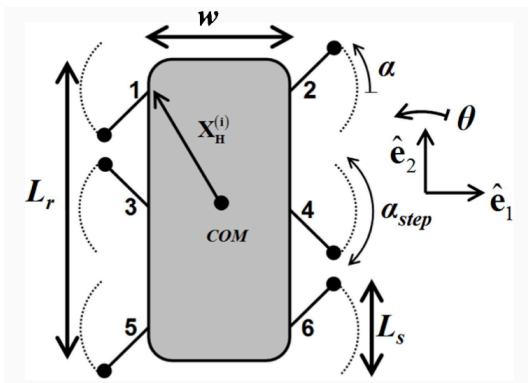


Figure 2: Robot with asymmetric stiffness joints [8]. The numbers one to six are the names for the legs.  $L_r$  is the length of the robot and  $w$  is the width.  $\alpha_{step}$  is the step angle and  $\alpha$  is half of  $\alpha_{step}$ .  $L_s$  is the step size.

**Decoupled sides** The steering mechanism in this category performs a turn by actuating one side of the robot, or by moving its sides in opposite direction. As a result, a robot which has a decoupled sides steering mechanism always has at least one extra actuator.

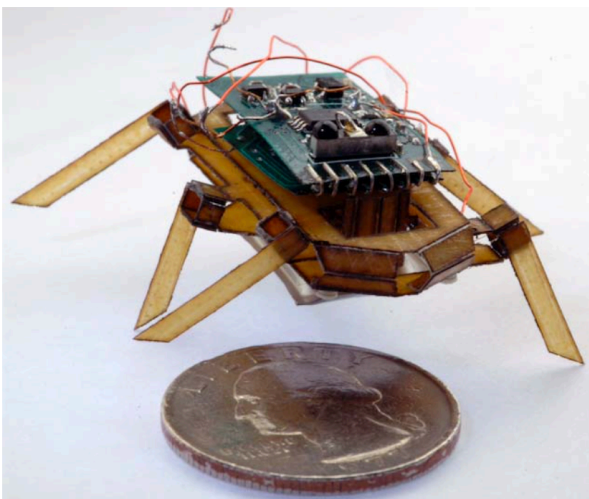


Figure 3: Picture of RoACH [9]. A robot with decoupled sides.

The RoACH by A.M. Hoover et al. [9], see Figure 3, has decoupled sides. RoACH has two actuators, both are used for steering. The size of RoACH is [L-W-H]=[3-?-?] mm. The width and height of RoACH is unknown and indicated with a question mark. RoACH can steer during walking, but is also able to rotate without any forward velocity.

Other robots which have decoupled sides to be able to steer are the TITAN-VIII by K. Arikawa et al. [10], the LEMUR IIb by T. Bretl et al. [11], and the SCOUT and SCOUT II [12], [13] by M. Buehler et al. The TITAN-VIII has eight actuators, of which four are for steering. The size of TITAN-VIII is [L-W-H]=[600-400-250] mm. The LEMUR IIb has eight actuators, all are used to steer. The size of the LEMUR IIb is [L-W-H]=[510-880-150] mm. The SCOUT II has four actuators, of which it uses all four to steer. The size of the SCOUT II is [L-W-H]=[200-140-190] mm.

**Translational transmission** Changing the amplitude with a lever transmission is a simple method to allow a robot to steer. An example of a lever transmission can be found in Figure 4. For the configuration in Figure 4a, the black triangle is in the middle and therefore, the amplitude of the leg step size is the same on both sides. For the configuration in Figure 4b the black triangle is moved to the left and the amplitude of the left side is shorter than the right side. The transmission ratio is determined by the position of the black triangle. The robot can be steered by changing the transmission ratio.

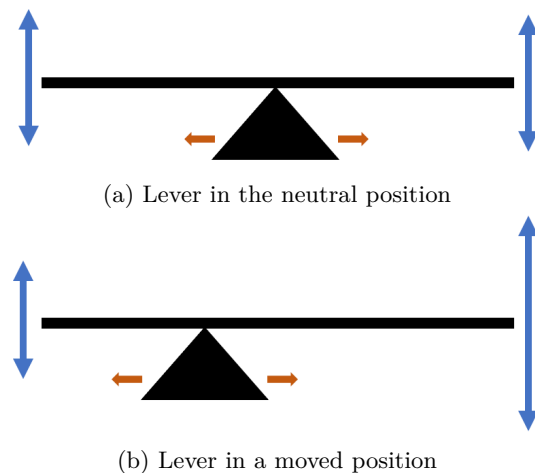


Figure 4: Lever transmission in two configurations. The red arrows indicate the direction of movement of the triangle. The blue arrows on either side of the bar show the direction of movement of the bar. The length of the blue arrow indicates the amplitude of the displacement.

The lever transmission system is used in Dash by P. Birkmeyer et al. [14], see Figure 5. The light grey bar with the strings on it represents the triangle and when it moves the step amplitude of the legs of one side changes with respect to the other side. Dash has two actuators, of

which one is used to actuate the transmission. The size of Dash is [L-W-H]=[100-100-50] mm.

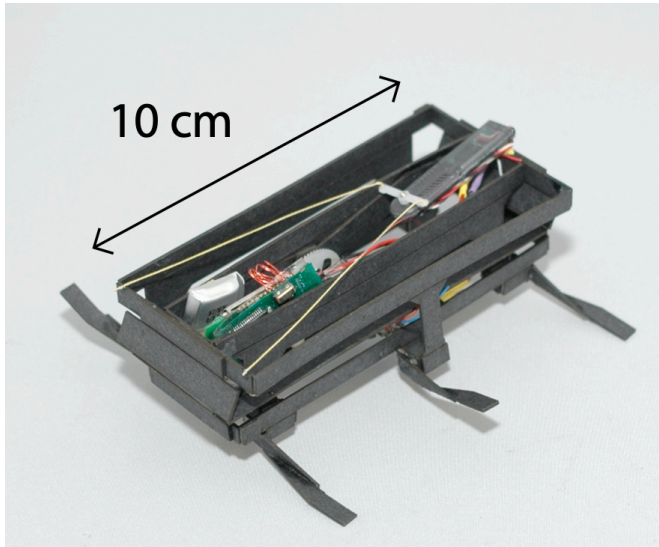


Figure 5: Picture of Dash with lever transmission system [14]. The lever transmission consists of the light grey bar on top and the two yellow ropes.

**Rotational transmission** A rotational transmission system can also be used to steer. The transmission system can change the amplitude ratio between each side. Although this mechanism is possible to use as a steering mechanism, no examples have been found in literature.

### 3.1.3 Leg orientation

Steering mechanisms in the category leg orientation change the direction of motion in order to achieve a turn. Changing the direction of motion can be done by rotating the legs, so when the legs are actuated they move in a different direction with respect to the robot's body. A rotation of the leg can be in the horizontal plane or the vertical plane.

**Horizontal rotation** The principle of rotating the legs horizontally is very similar to the steering mechanism in a car. This mechanism is used in Mini-Whegs IV [15], but also in older generation Whegs robots [16]–[19]. The steering mechanism in Mini-Whegs IV can be seen in Figure 6. The top double-sided arrow shows the direction of rotation for the steering mechanism. Mini-Whegs has two actuators, of which one is for steering. The size of Mini-Whegs is [L-B-H]=[90-68-20] mm.

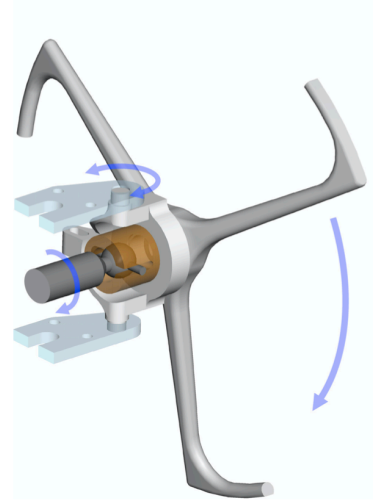


Figure 6: Horizontal rotation steering mechanism of the Mini-Whegs [15]. From left to right the blue arrows show the rotation of the drive shaft, the rotation of steering mechanism, and rotation of the legs.

A similar concept is used in the quasi-passive walking robot of F. Ikeda and S. Toyama [20]. The forward locomotion of this robot is passive, meaning it needs to be on an inclined surface to walk. Therefore, the quasi-passive walking robot only has one actuator to steer. The size of the quasi-passive walking robot is [L-W-H]=[?-?-550] mm.

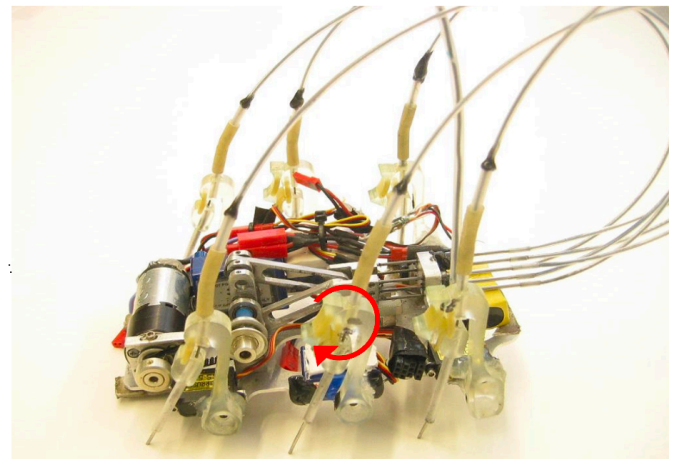


Figure 7: Picture of iSprawl [21] with the vertical rotation steering mechanism. A red arrow was added to show the direction of rotation.

**Vertical rotation** A robot which uses a rotation in the vertical plane is iSprawl [21], by S. Kim et al., see Figure 7. The middle leg can be rotated in the vertical plane. By rotating the middle leg in a different orientation the robot can make a turn [22]. The iSprawl uses three actuators, of which two are used for steering. The size of iSprawl is [L-W-H]=[155-116-70] mm. Sprawlita by J.G. Cham et al. [23] uses the same steering mechanism as the iSprawl.

Sprawlita also has three actuators, of which two are for steering. The size of Sprawlita is unknown.

### 3.1.4 Gaits

Gaits, also known as walking patterns, have been researched extensively in the past. A gait is a way of walking or moving on foot. This way is different for walking on a straight or curved path. By changing a gait a steering motion can be induced. Gait patterns of insects have been studied extensively [24]–[30]. For walking robots, it is interesting to look at insects and their gaits because insects have multiple legs. Changing the gait can be achieved by using a different timing between each step.

A robot which uses a turning gait to steer is the MEDIC, designed by N.J. Kohut [31], see Figure 8. The MEDIC has four actuators and uses all these actuators to steer. The dimensions of MEDIC are [L-W-H]=[55-35-18] mm.

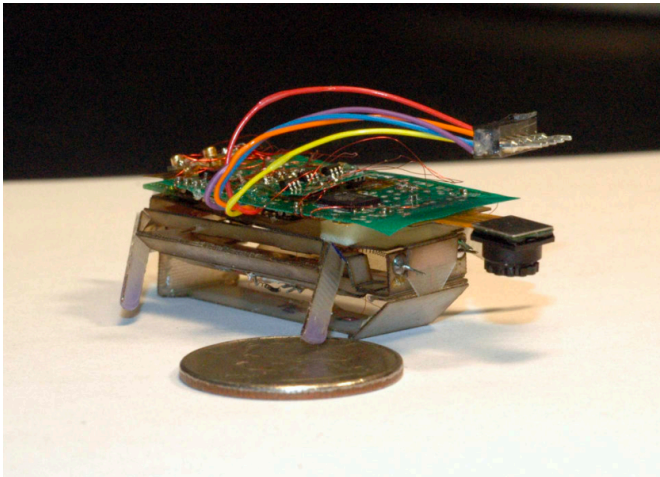


Figure 8: Picture of MEDIC [31] which uses a gait change to steer.

Other walking robots which use gaits as their turning mechanism are the six-legged walking robot of G. Chen et al. [32] and the quadruped robot of C. Chan et al. [33]. The six-legged walking robot has twelve actuators, of which six are used for walking and for the gait pattern. The size of the six-legged walking robot is [L-W-H]=[595.2-395-?] mm. The quadruped robot uses four actuators and these four are used for the gait pattern. The size of the quadruped robot is not mentioned in the literature.

## 3.2 Force

The internal steering methods which are categorised in the force section use a change in force to allow the robot to steer. The change in force can be either at the contact point between the leg and the ground or the point between the leg and the body. These steering mechanisms are described in Section 3.2.1 and 3.2.2.

### 3.2.1 Sliding friction

Sliding friction steering mechanisms use the method of creating asymmetry in the friction force. By reducing the friction force between the leg and the ground slipping behaviour can be introduced. This slip causes the robots to displace less while the leg step size stays the same. If this happens on only one side of the robot it causes the robot to steer.

The friction force can be changed by changing the dynamic friction coefficient. As can be seen in Equation 1 a lower dynamic friction coefficient  $\mu_k$  lowers the friction force. The dynamic friction coefficient can be lowered by the use of lubrication or by changing the material since the friction coefficient is related to a combination of materials. We can divide the sliding friction steering mechanisms into two subcategories, namely robots that have feet with multiple friction coefficients and robots that use lubrication.

$$F_{friction} = \mu_k * N \quad (1)$$

**Multi-friction legs** A difference in friction force can be created with legs which can change the friction coefficient. This steering mechanism would for example have a foot with two different friction coefficients. Depending on the placement angle of the leg either the high friction coefficient part or the low friction coefficient part touches the ground. The low friction coefficient part can cause the robot to slip and turn. A robot which uses this principle as a steering mechanism has not been found in literature.

**Lubrication** The use of lubrication in a robot is not unusual, but using it to make a robot steer has never been done. Lubrication can be used to reduce friction force. By the use of Lubrication between the contact point of the leg and the ground, the friction force can be lowered. This causes this side to slip and the robot to turn. This steering mechanism used in a robot has not been found in literature.

### 3.2.2 Centre of pressure

By exchanging one of the legs for a stiffer one, the centre of pressure (CoP) of the robot moves. The CoP is determined by the touchdown and takeoff angle of the leg. By changing the stiffness of the leg the touchdown and takeoff angles are changed and therefore the CoP is changed. J. Protoc and P. Holmes [34] showed that by moving the CoP, the translational kinetic energy can be exchanged for rotational kinetic energy. A change in CoP of 10% of body length, combined with a stiffer leg, can produce a turn of almost 90° in three strides.

**Stiffness legs** An example of a robot which uses different leg stiffness is the DynaRoACH[35] by Aaron M. Hoover et al, see Figure 9. Stiffening one of the middle legs results in consistent turning behaviour. The DynaRoACH has one actuator and it is not used for the

steering mechanism. The stiffening of the legs is done manually, replacing the leg with a stiffer one. The size of the DynaRoACH is [L-W-H]=[100-45-30] mm.

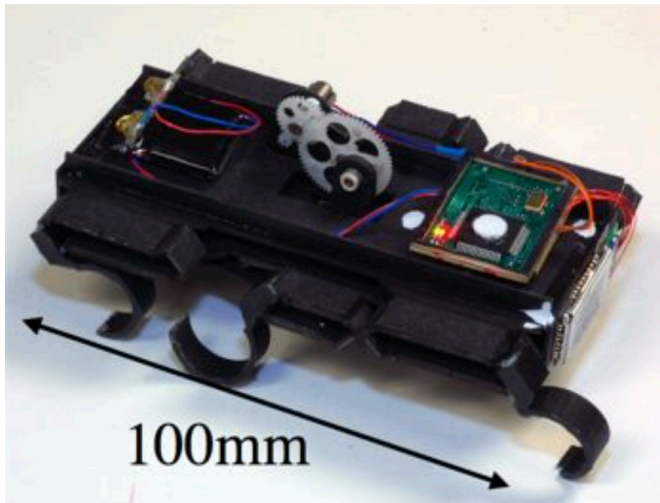


Figure 9: DynaRoACH with legs of different stiffness [35].

### 3.3 Velocity

Steering with a change in velocity is quite common in small walking robots. An asymmetric velocity of leg actuation can induce a rotation since one side displaces more distance. There are two mechanisms under the section that employ asymmetric velocity, namely, a differential mechanism and a differential drive. These mechanisms are discussed in Section 3.3.1 and 3.3.2 respectively.

#### 3.3.1 Differential mechanism

A differential mechanism can be found in all modern cars. It is used to go from one input to two output velocities. The output velocities are not necessarily the same. If one output velocity is larger than the other a robot can make a turn. A differential mechanism, as described in this section, is currently not used in a walking robot.

#### 3.3.2 Differential drive

A differential drive is essentially a robot with separate motors for each side. The separate motor allows the robot to change the velocity on each side independently. By making the velocity on one side larger than the other side, the robot will make a turn. Because the velocity of one side is larger, this side will displace more distance in a shorter time, resulting in a turn. It is the other way around for a smaller velocity. This working mechanism is illustrated in Figure 10.

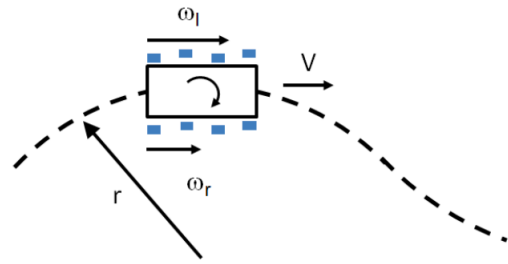


Figure 10: Alternating steering concept[6]. The angular velocity of the outer leg  $\omega_l$  is greater than  $\omega_r$ , resulting in a turn with radius  $r$ .

The OctoRoACH by A.O. Pullin et al. [6], see Figure 11, uses a differential drive as a steering mechanism. The OctoRoACH has three actuators, of which two are used for the differential drive steering mechanism. The size of the OctoRoACH is [L-W-H]=[100-45-30] mm.

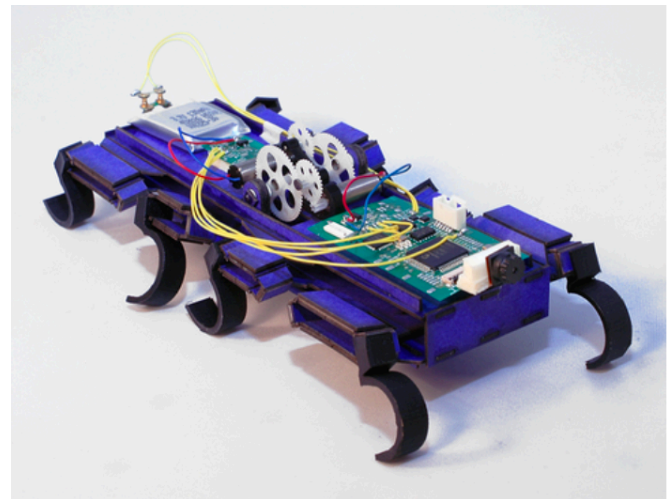


Figure 11: Picture of the OctoRoACH [6] with a differential drive steering mechanism.

Other walking robots which use a similar differential drive system are RHex [1], [36]–[38] by U. Saralini et al, the LoadRoACH by C.S. Casarez et al [39], the SailRoACH by N.J. Kohut et al [5], and the VelociRoACH by D.W. Haldane [40].

RHex has six actuators and all six are used for the differential drive. The size of RHex [L-W-H]=[530-?-?] mm. LoadRoACH has three actuators of which it uses two for the differential drive. The size of LoadRoACH [L-W-H]=[150-?-?] mm. The SailRoACH has three actuators of which it uses two to actuate the differential drive. The size of the SailRoACH is [L-W-H]=[210-45-80] mm. The VelociRoACH has two actuators and both are used to actuate the differential drive. The size of VelociRoACH is [L-W-H]=[100-65-42] mm.

## 4 Added mechanisms

In this chapter, all the added steering mechanisms are described. The added displacement, force and velocity are discussed in Section 4.1, 4.2, and 4.3, respectively.

### 4.1 Displacement

Displacement steering mechanisms which are categorised under the Added mechanisms chapter use a change in the added mechanism to take a step. The steering methods either make use of changing the step direction in the horizontal plane or use an added mechanism which can also take a step.

The mechanisms can be categorized by the use of their working principle. The first mechanism has an extra leg which is only used for steering. The second mechanism changes the direction of the step within the horizontal plane with the use of the added mechanism. These mechanisms are discussed in Section 4.1.1 and 4.1.2.

#### 4.1.1 Lifting

The added mechanism lifting signifies that the robot is lifted and after lifting either rotates or actuates like normal. The robot can either be completely lifted or partially lifted.



Figure 12: Picture of EPFL jumping robot [4], with lifting mechanism. The cage around the robot lifts the robot off the ground.

**Lift and rotate** An added mechanism which lifts and rotates the robot allows for efficient steering because it enables turning without any horizontal displacement. This mechanism is used by the EPFL jumping robot of M. Kovac et al. [4], see Figure 12. Although, it is a jumping robot and not a walking robot, the steering mechanism

itself is also operable for walking robots. The robot gets lifted by the cage and then rotated. The EPFL robot has two actuators, both are used to make the robot rotate. The dimensions of the robot are [L-W-H]=[180-180-180] mm.

**Arm and slide** An extra leg lifting the robot and moving it to the side is also a mechanism which makes a robot turn. If this process is repeated it can cause a robot to rotate. This mechanism is used in the robot presented by J. Zhang et al. [41], see Figure 13. The steering movement is also visible in Figure 13. The robot has two actuators of which one is for steering. The size of the robot is [L-W-H]=[120-90-70] mm.



Figure 13: Robot by J. Zhang et al. [41] with lifting arm. The arm is visible in grey and the red arrow indicates the direction of rotation of the arm. On the left, the robot is in an unturned position. On the right, the arm has made a full rotation and the robot is rotated a bit.

**Side and actuate** For a robot layout with legs on either side of the robot a steering mechanism can be created by lifting one of its sides and actuating the other side like normal. The lifting of the robot can be done by an external arm. Because only one side of the robot makes contact with the ground, only this side moves the robot. This makes the robot turn around the contact point of the lifting arm. Such a steering mechanism has not been found in literature.

#### 4.1.2 Body geometry

Changing the geometry of a robot's body could change the leg orientation and, therefore, change the direction of the step in the horizontal plane. A robot with this steering mechanism could, for example, have a rotational joint in the middle of its body. An actuator could move the robot around this joint, folding the robot, and create an asymmetry within the leg displacement, resulting in a turn. The mechanism can be compared to an articulated vehicle. It could be expected that such a system would have been used in a robot's steering mechanism. However, no evidence has been found in literature.

## 4.2 Force

Steering mechanisms which are categorised under section 4.2 have a mechanism in place which allows them to apply another force without using the legs. This extra force creates an asymmetry and allows the robot to steer. The external force mechanisms are discussed in Section 4.2.1 and 4.2.2.

### 4.2.1 Sliding friction

Similarly, as with the internal sliding friction discussed in Section 3.2.1, external sliding friction steering methods create an asymmetry in the friction force. Instead of using the robot's legs to change the friction force it uses the added mechanism. This can be done by having a mechanism which creates a larger friction force on one side or changes the normal force.

**Friction force** Asymmetric friction can be created by adding an extra contact point on one side of the robot. If this point remains in contact with the ground during walking the robot will steer in the direction of the contact point.

The LoadRoACH by C.S. Casarez and R. S. Fearing [39], see Figure 14, has a drag tail which allows the robot to create more friction on one side. This allows the LoadRoACH to steer. The LoadRoACH has three actuators, of which one is used for the drag tail steering mechanism. The size of the LoadRoACH is [L-W-H]=[150-?-?] mm.

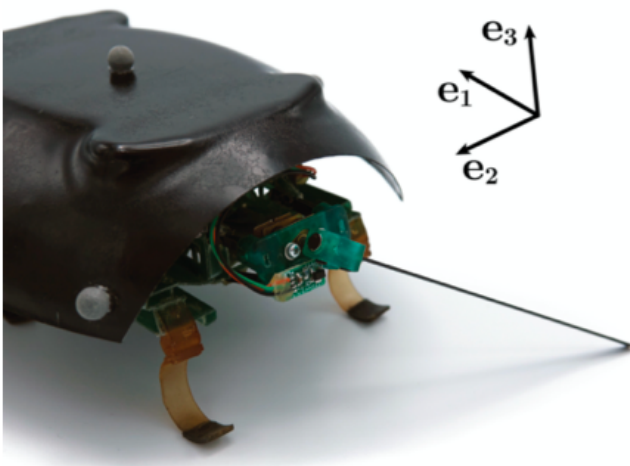


Figure 14: Picture of LoadRoACH [39], with drag tail.

**Changing normal force** By changing the centre of gravity (CoG), the distribution of the normal force on the legs can be changed from a symmetric set-up to an asymmetric set-up. Changing the normal force will change the friction force because they are related by the dynamic friction coefficient  $\mu_k$  as can be seen in Equation 1. So, by changing the CoG, an asymmetry in the friction force can be created, causing one side to slip more and as

a result, induce a turn. This steering mechanism is not found in literature.

### 4.2.2 Fluid friction

Steering with fluid friction is done by creating asymmetric aerodynamic drag. Aerodynamic drag is formed by velocity, surface area and shape. When this area is asymmetric the aerodynamic drag, and therefore fluid friction, causes the robot to turn.

The SailRoACH designed by N.J. Kohut et al.[5], see Figure 15, uses fluid friction as a steering method. The SailRoACH has an aerosail which can rotate from side to side to create drag. The sail becomes most effective around a forward velocity of  $2ms^{-1}$ , which is equal to 20 body lengths per second. The aerodynamic effects are greatly influenced by the scale of the robot. Aerodynamic steering is most effective for small robots. For example, if the SailRoACH would be twice its size, the turning radius would increase five times for a velocity of  $1ms^{-1}$  and two and a half times for a velocity of  $2ms^{-1}$ . Refer to the paper of N.J. Kohut et al. [5] for more details. The SailRoACH has three actuators, of which one is used to control the aerosail. The size of the SailRoACH is [L-W-H]=[100-45-30] mm and the aerosail is [L-H]=[50-50] mm. This brings the total size to [L-W-H]=[210-45-80] mm.

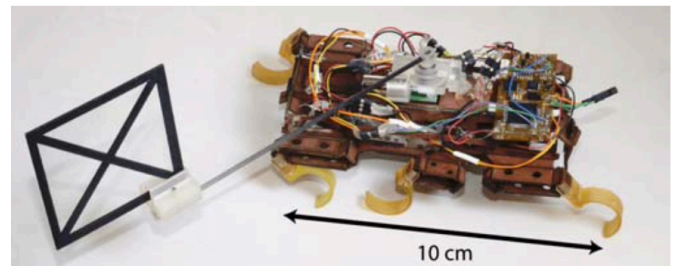


Figure 15: Picture of the SailRoACH [5] with aerosail. The sail is made from black cardboard and transparent PET.

## 4.3 Velocity

An added steering mechanism which uses a change in its velocity to steer a robot is not common in literature. However, with the use of angular momentum which is a multiplication of mass, arm, and velocity there are some robots which use this as a steering mechanism.

### 4.3.1 Angular momentum

Steering with the change of angular momentum is done by having a mass on a rotating arm. This change in angular momentum is converted to a moment on the robot in the opposite direction, which causes the robot to turn a little bit. The mass moves slowly back to its original position and repeats the process, causing the robot to steer.

The OctoRoACH by A.O. Pullin et al.[6], see Figure 16, uses a tail to induce a large change in angular momentum in a short time. The OctoRoACH has been

mentioned before in Section 3.3, it has a configuration with and without the tail. The OctoRoACH has three actuators of which one is used to control the tail. The size of the OctoRoACH with the tail is [L-W-H]=[230-45-30] mm.

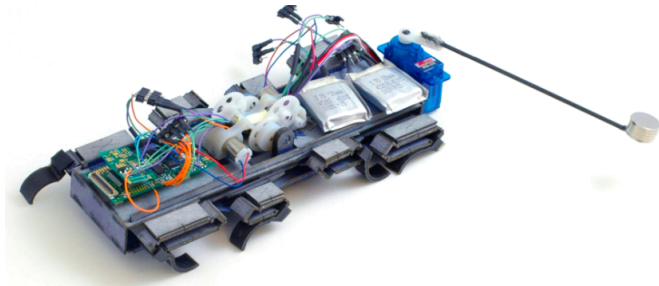


Figure 16: Picture of the OctoRoACH with angular momentum tail [6].

Another robot which uses the same steering mechanism is the TAYLRoACH[42] by N.J. Kohut et al. The TAYLRoACH has three actuators of which one is used to control the tail. The size of the TAYLRoACH's body is [L-W-H]=[100-45-30] mm. The tail has a length of 102 mm. So, the total size of the TAYLRoACH is [L-W-H]=[202-45-30] mm.

## 5 Discussion

The steering mechanisms tree diagram, see Figure 1, has been updated with the literature, see Figure 17. The missing mechanisms have been coloured red. These mechanisms are deemed missing as there was no evidence found in the literature which could confirm the use of these steering mechanisms. However, some literature can be interpreted or used in a different way to support the possibility of using alternative concepts as steering mechanisms. These concepts are presented in Section 5.1. An overview of all the steering mechanisms and properties can be found in Section 5.2.

### 5.1 Additional concepts

The results from the literature study show that quite a lot of robot steering mechanisms have not been explored (yet). In this section additional concepts to enable steering are added to complete the figure. The additional concepts are a contribution to make the overview more complete. These concepts are currently not used as steering mechanisms for robots however, when modified, could potentially be implemented to serve that purpose.

#### 5.1.1 Leg length: Motor

Leg length actuated by a motor has not been used in a robot. However, the EduBot [43] by K. Galloway et al., see Figure 18, changes the length of the legs to change the stiffness. The EduBot uses a DC motor to deform the legs, causing stiffer legs. The legs deform symmetrically. The EduBot uses the change in stiffness to make the robot go

faster on different terrains. However, if the mechanism of the EduBot is used asymmetrically the robot would have longer legs on one side, causing the robot to make a turn. EduBot has twelve actuators of which six are used to change the leg length. The size of EduBot is unknown.

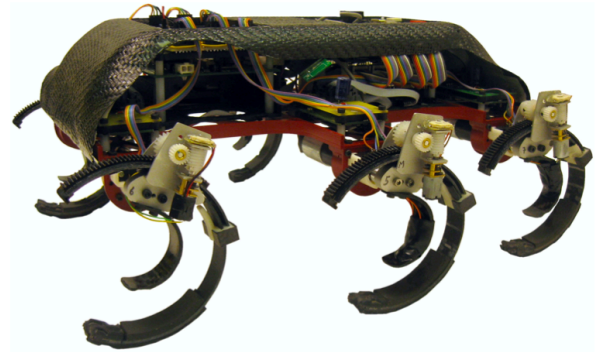


Figure 18: The EduBot with tuneable stiffness C-legs [43].

#### 5.1.2 Rotational transmission

A different type of transmission which can be used as a steering method for walking robots is a compliant Continuously Variable Transmission (CVT) [44]. A basic warping beam transmission can be seen in Figure 19. The transmission ratio is determined by the location of the black triangle. For a transmission ratio 1:3 left in Figure 19, the input angular rotation is less than the output angular rotation. For the transmission ratio 1:1 on the right in Figure 19, the input angular rotation is the same as the output angular rotation. A CVT can be used as a steering mechanism if it is implemented between the actuator and the legs.

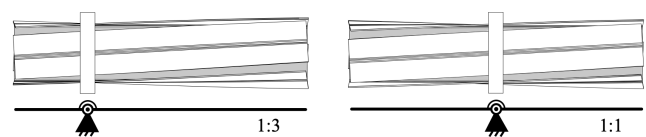


Figure 19: Warping displacement of a member subjected to a torsional moment [44].

#### 5.1.3 Sliding friction: Multi-friction legs

A multiple-friction leg has not been used in walking robots. However, it has been used in crawling robots. The Printed Soft robot (PS robot) [45], [46] has multiple materials within the surface which make contact with the ground, see Figure 20. Depending on the orientation of this surface, the surface either has a high or low friction coefficient. This method of changing the surface orientation to increase or decrease the friction coefficient can be used to steer a robot. Decreasing the friction force on one side, causes this side to slip.

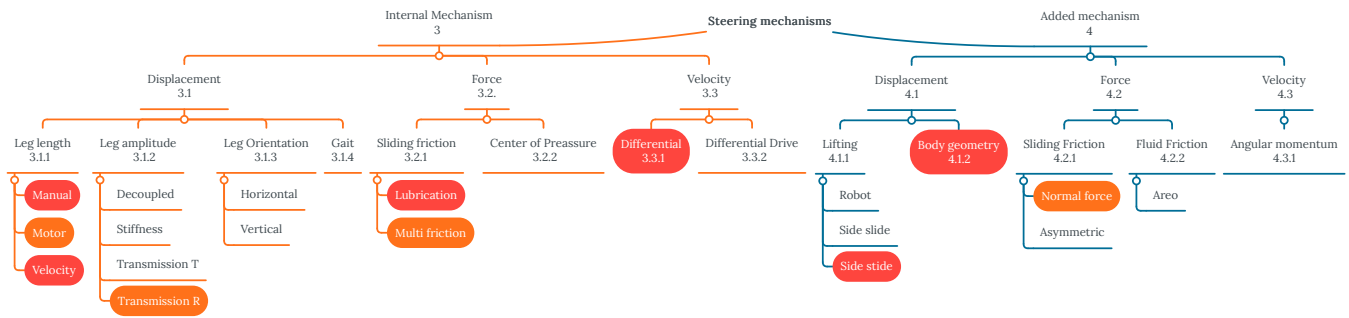


Figure 17: Tree of steering mechanisms with missing mechanisms in red and the additional concepts in orange. The additional concepts of steering mechanisms are described in Section 5.1.

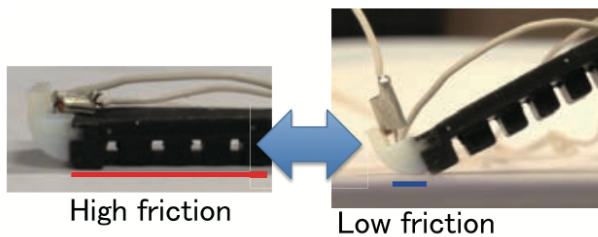


Figure 20: PS robot with variable friction legs [45]. The white part has a different friction coefficient than the black part.

The soft crawling robot presented by Xinjun Sheng et al. [47] also has various friction feet, but instead of changing the orientation of the surface by the use of the body itself, it uses a pneumatic pump.

#### 5.1.4 Sliding friction: normal force

Changing the normal force has not been used to make walking robots steer. Nevertheless, it has been used as traction control for mobile robots with wheels. This traction control system changes the normal force with the change of CoG or a change of the rotation of a gyroscope.

An example of this traction control in use is in the two-wheeled robot of A.M.H.S. Abeykoon et al. [48]. The mechanism is visible in Figure 21. The black rod moves to the right side and increases the normal force on the right wheel. Because the wheels are actuated separately the change in normal force can cause the side with a smaller force to slip. This slip can induce a turn. Although this robot has wheels and no legs the mechanism itself can be used for a walking robot as well. The amount of actuators in the robot is unknown. The size of the robot is also unknown.

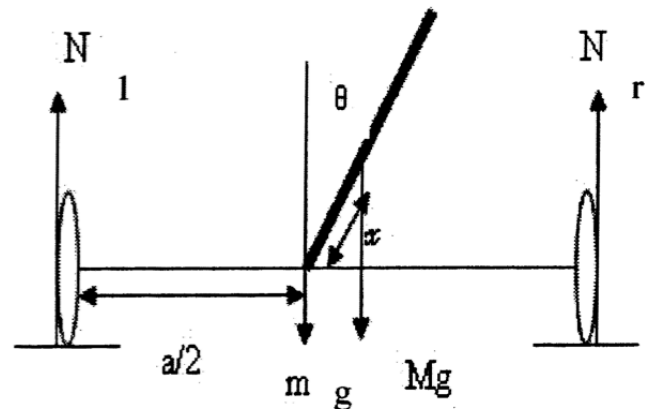


Figure 21: Changeable normal force distribution[48]. The black rod can be changed by angle  $\theta$ . If  $\theta$  is positive the normal force on the left is larger than on the right. If  $\theta$  is negative the opposite effect can be observed.

Similar mechanisms of changing the centre of gravity are in the Mars Exploration Rover Spirit by K. Skonieczny and G.M.T. D'Eleuterio [49] and the Nexus 6 by K. Yoshida and H. Hamano [50].

A gyroscope is a flywheel that is gimbaled in such a way that the angular momentum vector direction can be reoriented. If the flywheel is spinning at constant velocity and gets reoriented with a roll or pitch rotation it exerts a vertical force. This force can be used to change the normal force on the legs. Changing the normal force can cause a robot to steer as mentioned in Section 4.2. The Wheeled Rover of C. A. Cao [51] uses a gyroscopic system as traction control. The gyroscopic system is used to increase the normal force for extra traction. This system can be used in a walking robot to increase the normal force and, therefore, increase friction on one side.

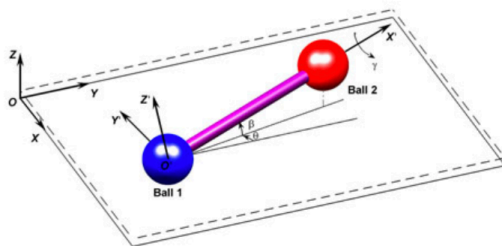
#### 5.1.5 Sliding friction: Normal vibrations

A conceptual design for steering with sliding friction would be to introduce normal vibrations. The work of M. Chowdhury and M. Helali [52] examines how friction coefficients are affected by the amplitude of normal vibrations at different frequencies. They found that there is a relation between the friction coefficient and the

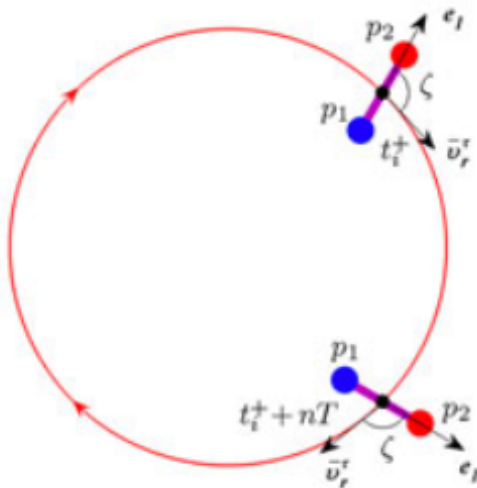
amplitude of normal vibrations at different frequencies. In their work they conclude that the percentage of friction coefficient decreases almost linearly. By implementing these vibrations on the legs at only one side of the robot, this side has less friction and will start to slip, inducing a turn.

### 5.1.6 Sliding friction: Bouncing vibrations

Another conceptual design of a steering mechanism can be made with a bouncing dimer and vibrations. A study by J. Wang et al. [53], shows that a bouncing 3D dimer, see Figure 22a, upon a horizontal plate which is undergoing a vertical harmonic vibration, will follow a circular orbit, see Figure 22b.



(a) An image of a 3D dimer [53]



(b) Circular orbit of a bouncing 3D dimer [53] on a vibrating plate. The 3D dimer is shown for two different time frames. The red line shows the circular orbit.

Figure 22: A 3D dimer and its circular orbit.

## 5.2 Steering mechanisms

The additional concepts are added to the tree and marked in orange, see Figure 17. An explanation for these missing concepts might be that they are simply too inconvenient, too complicated or are easily replaced with a better steering mechanism.

### 5.2.1 Overview of steering mechanisms

To evaluate and compare the presented steering methods, Table 2 shows a summary of the important properties

of each method. The complexity is determined by the amount of total actuators and the amount of actuators necessary to steer. Furthermore, the robot size is important. The column 'Smaller possible' is added to check if it is likely that it is possible to downscale the design of the robot and the steering mechanism. The steering mechanisms have been divided into three categories: concept, used in different robots and used in walking robots. This is based on how the mechanism is used in the literature: Is the mechanism never used in a mobile robot, is the mechanism used in a different kind of robot or is it used in a walking robot.

### 5.2.2 Trends in the overview

While looking at the overview it becomes clear that every steering mechanism that already exists needs at least one extra actuator or needs a manual action. The existing robots have an actuator besides the locomotion actuators. The only one which does not have an extra actuator is the DynaRoACH. However, DynaRoACH requires a manual action to perform a turn.

It is remarkable that steering mechanisms which have decoupled sides or a differential drive to steer have at least two extra actuators. Steering mechanisms which use a gait change to steer have at least four extra actuators.

Also notable, but logical, for bigger size robots it is possible to scale down. Smaller size robots are not likely to be scaled down compared to the bigger robots with the same steering mechanism.

## 6 Conclusion

The purpose of the paper is to give an overview of different methods to make a robot steer, to show the existing steering mechanisms and concepts which can be used as steering mechanisms, to show the non-existing steering mechanisms, and to give an overview of important properties. To provide a good overview a classification is introduced based on the physical ways to make a walking robot steer. The steering mechanisms that populate the tree diagram show the possible methods of enabling directional control, based on their respective basic physical principles.

Section 5.1 adding concepts shows conceptual ideas that can be used as a steering method. However, these concepts are not proven and this set of ideas is not complete. Nevertheless, when new concepts are thought of or tested, the classification helps to categorise and compare it to other steering mechanisms.

Another purpose of the paper is to give an overview of important properties. The presented examples provide a representation of the existing steering mechanisms. The overview of the presented existing examples and the conceptual additional concepts can serve as a useful reference when deciding on a steering mechanism. The overview can be used during the design phase of a small walking robot.

Table 2: Table with all the steering mechanisms and their properties.

Category	Name	Actuators	Actuators steering	Size [L-W-H] [mm]	Smaller possible
Concept	Stiffness joints [8]	-	-	?-?-?	-
	Rotational transmission [44]	-	-	?-?-?	-
	Bouncing vibrations [53]	-	-	?-?-?	-
	Leg length motor [EduBot] [43]	12	6	?-?-?	Yes
	MFL motor [46]	-	-	?-?-?	-
	Normal vibrations [52]	-	-	?-?-?	-
Used in different robot	Wheeled rover [51]	-	-	?-?-?	-
	Change of CoG [49]	2	1	900-600-300	Yes
	Lift legs and slide [41]	2	1	120-90-70	Yes
	Lift robot and rotate [4]	2	1	180-180-180	Yes
Used in walking robot	Drag tail [LOADRoACH] [39]	3	1	150-?-?	No
	Lever transmission [Dash] [14]	2	1	100-100-50-	No
	Aero sail [SAILRoACH] [5]	3	1	210-45-30	No
	Angle moment [OctoRoACH] [6]	3	1	230-45-30	No
	Angle moment [TAYLRoACH] [42]	3	1	202-45-30	No
	Differential drive [OctoRoACH] [6]	3	2	100-45-30	No
	Differential drive [RHex] [37]	6	6	530-?-?	Yes
	Differential drive [VelociRoACH] [40]	2	2	100-65-42	No
	Decoupled sides [RoACH] [9]	2	2	3-?-?	No
	Decoupled sides [TITAN-VII] [10]	8	4	600-400-250	Yes
	Decoupled sides [LEMUR IIB] [11]	8	8	510-880-150	Yes
	Decoupled sides [SCOUT] [12]	4	4	200-140-190	Yes
	Rotate legs vertical [iSprawl] [21]	3	2	155-116-70	No
	Rotate legs vertical [Sprawlita] [23]	3	2	?-?-?	No
	Rotate legs horizontal [whegs] [15]	2	1	90-68-20	No
	Rotate legs horizontal [Quasi] [20]	1	1	?-?-550	Yes
	Variable stiffness [DynaRoACH] [35]	1	Manual	100-45-30	No
	Turning gaits [6-legged robot] [32]	12	6	595.2-395-?	Yes
	Turning gaits [MEDIC] [31]	4	4	55-53-18	No
	Turning gaits [Quadruped robot] [33]	4	4	?-?-?	Yes

## References

- [1] R. Altendorfer, N. Moore, H. Komsuolu *et al.*, ‘RHex: A Biologically Inspired Hexapod Runner,’ *Autonomous Robots*, vol. 11, no. 3, pp. 207–213, 2001, ISSN: 09295593. DOI: 10 . 1023 / A : 1012426720699.
- [2] J. K. Schonebaum, ‘Challenge the future Department of Precision and Microsystems Engineering The design of a monolithic, compliant, resonant running robot at insect scale,’ Tech. Rep., 2019.
- [3] F. Delcomyn, ‘Walking Robots and the Central and Peripheral Control of Locomotion in Insects,’ *Autonomous Robots*, vol. 7, no. 3, pp. 259–270, 1999, ISSN: 09295593. DOI: 10.1023/A:1008928605612.
- [4] M. Kovač, M. Schlegel, J. C. Zufferey and D. Floreano, ‘Steerable miniature jumping robot,’ *Autonomous Robots*, vol. 28, no. 3, pp. 295–306, Apr. 2010, ISSN: 09295593. DOI: 10.1007/s10514-009-9173-4.
- [5] Kohut N. J., Zarrouk D., Peterson K.C. and Fearing R. S., ‘Aerodynamic Steering of a 10 cm High-Speed Running Robot,’ 2013. [Online]. Available: <https://ieeexplore.ieee.org/document/6697167>.
- [6] A. O. Pullin, N. J. Kohut, D. Zarrouk and R. S. Fearing, ‘Dynamic turning of 13 cm robot comparing tail and differential drive,’ in *Proceedings - IEEE International Conference on Robotics and Automation*, Institute of Electrical and Electronics Engineers Inc., 2012, pp. 5086–5093, ISBN: 9781467314039. DOI: 10.1109/ICRA.2012.6225261.
- [7] Noah Webster, *Webster’s New International Dictionary of the English Language*. G. & C. Merriam Co, 1959.
- [8] D. Zarrouk and R. S. Fearing, ‘Compliance-based dynamic steering for hexapods,’ in *IEEE International Conference on Intelligent Robots and Systems*, 2012, pp. 3093–3098, ISBN: 9781467317375. DOI: 10 . 1109 / IROS . 2012 . 6385663.

- [9] A. Hoover, E. Steltz and R. Fearing, ‘RoACH: An autonomous 2.4g crawling hexapod robot,’ in *2008 IEEE/RSJ International Conference on Intelligent Robots and Systems*, IEEE, Sep. 2008, pp. 26–33, ISBN: 978-1-4244-2057-5. DOI: 10.1109/IRoS.2008.4651149.
- [10] K. Arikawa and S. Hirose, ‘Development of quadruped walking robot TITAN-VIII,’ *IEEE International Conference on Intelligent Robots and Systems*, vol. 1, pp. 208–214, 1996. DOI: 10.1109/IRoS.1996.570670.
- [11] T. Bretl, S. Rock, J.-C. Latombe, B. Kennedy and H. Aghazarian, ‘Free-Climbing with a Multi-Use Robot,’ Tech. Rep.
- [12] M. Buehler, R. Battaglia, A. Cocosco, G. Hawker, J. Sarkis and K. Yamazaki, ‘SCOUT: A simple quadruped that walks, climbs, and runs,’ in *Proceedings - IEEE International Conference on Robotics and Automation*, vol. 2, Institute of Electrical and Electronics Engineers Inc., 1998, pp. 1707–1712, ISBN: 078034300X. DOI: 10.1109/ROBOT.1998.677408.
- [13] I. Poulakakis, E. Papadopoulos and M. Buehler, ‘On the Stability of the Passive Dynamics of Quadrupedal Running with a Bounding Gait,’ *The International Journal of Robotics Research*, vol. 25, no. 7, pp. 669–687, Jul. 2006, ISSN: 0278-3649. DOI: 10.1177/0278364906066768.
- [14] P. Birkmeyer, K. Peterson and R. S. Fearing, ‘DASH: A dynamic 16g hexapedal robot,’ in *2009 IEEE/RSJ International Conference on Intelligent Robots and Systems*, IEEE, Oct. 2009, pp. 2683–2689, ISBN: 978-1-4244-3803-7. DOI: 10.1109/IRoS.2009.5354561.
- [15] J. M. Morrey, B. Lambrecht, A. D. Horchler, R. E. Ritzmann and R. D. Quinn, ‘Highly Mobile and Robust Small Quadruped Robots,’ in *IEEE International Conference on Intelligent Robots and Systems*, vol. 1, 2003, pp. 82–87. DOI: 10.1109/iros.2003.1250609.
- [16] K. A. Daltorio, A. D. Horchler, S. Gorb, R. E. Ritzmann and R. D. Quinn, ‘A Small Wall-Walking Robot with Compliant, Adhesive Feet 1,’ Tech. Rep. [Online]. Available: <http://biorobots.case.edu>.
- [17] T. J. Allen, R. D. Quinn, R. J. B and R. E. Ritzmann, ‘Abstracted Biological Principles Applied with Reduced Actuation Improve Mobility of Legged Vehicles,’ Tech. Rep., 2003.
- [18] R. Quinn, J. Offi, D. Kingsley and R. Ritzmann, ‘Improved mobility through abstracted biological principles,’ in *IEEE/RSJ International Conference on Intelligent Robots and System*, IEEE, pp. 2652–2657, ISBN: 0-7803-7398-7. DOI: 10.1109/IRDS.2002.1041670.
- [19] R. Schroer, M. Boggess, R. Bachmann, R. Quinn and R. Ritzmann, ‘Comparing cockroach and Whegs robot body motions,’ in *IEEE International Conference on Robotics and Automation, 2004. Proceedings. ICRA '04. 2004*, IEEE, 2004, pp. 3288–3293, ISBN: 0-7803-8232-3. DOI: 10.1109/ROBOT.2004.1308761.
- [20] F. Ikeda and S. Toyama, ‘A proposal of right and left turning mechanism for quasi-passive walking robot,’ in *2015 International Conference on Advanced Robotics and Intelligent Systems (ARIS)*, IEEE, May 2015, pp. 1–5, ISBN: 978-1-4799-1851-5. DOI: 10.1109/ARIS.2015.7158369.
- [21] J. E. Clark, M. Cutkosky, S. Kim and M. R. Cutkosky, ‘iSprawl: Design and Tuning for High-speed Autonomous Open-loop Running. iSprawl: Design and Tuning for High-Speed Autonomous Open-Loop Running,’ Tech. Rep., 2006. [Online]. Available: <https://www.researchgate.net/publication/220121764>.
- [22] A. J. McClung, M. R. Cutkosky and J. G. Cham, ‘Rapid Maneuvering of a Biologically Inspired Hexapedal Robot,’ in *Dynamic Systems and Control, Parts A and B*, ASME, Jan. 2004, pp. 1195–1202, ISBN: 0-7918-4706-3. DOI: 10.1115/IMECE2004-61150.
- [23] J. G. Cham, S. A. Bailey, J. E. Clark, R. J. Full and M. R. Cutkosky, ‘Fast and Robust: Hexapedal Robots via Shape Deposition Manufacturing,’ *The International Journal of Robotics Research*, vol. 21, no. 10, pp. 869–882, Jul. 2004, ISSN: 02783649. DOI: 10.1177/027836402128964125.
- [24] R. Franklin, W. J. Bell and R. Jandert, ‘ROTATIONAL LOCOMOTION BY THE COCKROACH BLATTELLA GERMANICA,’ Tech. Rep. 4, 1981, pp. 249–255.
- [25] R. N. Hughes, ‘ESSENTIAL INVOLVEMENT OF SPECIFIC LEGS IN TURN ALTERNATION OF THE WOODLOUSE, PORCELLIO SCABER,’ Tech. Rep. 2, 1989, p. 493 491.
- [26] R. Straub and M. Heisenberg, ‘Coordination of legs during straight walking and turning in *Drosophila melanogaster*,’ Tech. Rep., 1990, pp. 403–412.
- [27] M. F. Land, ‘STEPPING MOVEMENTS MADE BY JUMPING SPIDERS DURING TURNS MEDIATED BY THE LATERAL EYES,’ Tech. Rep., 1972, pp. 57–72.
- [28] R. J. Full and M. S. Tu, ‘MECHANICS OF A RAPID RUNNING INSECT: TWO-, FOUR-AND SEX-LEGGED LOCOMOTION,’ Tech. Rep., 1991, pp. 215–231.
- [29] L. I. Frantsevich and P. A. Mokrushov, ‘Turning and Righting in *Geotrupes* (Coleoptera, Scarabaeidae),’ Tech. Rep., 1980, pp. 279–289.

- [30] Holke Cruse and Manuel G. Silva Saavedra, 'CURVE WALKING IN CRAYFISH,' 1996,
- [31] N. J. Kohut, A. M. Hoover, K. Y. Ma, S. S. Baek and R. S. Fearing, 'MEDIC: A legged millirobot utilizing novel obstacle traversal,' in *Proceedings - IEEE International Conference on Robotics and Automation*, 2011, pp. 802–808, ISBN: 9781612843865. DOI: 10 . 1109 / ICRA . 2011 . 5980360.
- [32] G. Chen, B. Jin and Y. Chen, 'Tripod gait-based turning gait of a six-legged walking robot,' *Journal of Mechanical Science and Technology*, vol. 31, no. 3, pp. 1401–1411, Mar. 2017, ISSN: 1738494X. DOI: 10.1007/s12206-017-0241-y.
- [33] C.-Y. Chan and Y.-C. Liu, 'Towards a walking, turning, and jumping quadruped robot with compliant mechanisms,' in *2016 IEEE International Conference on Advanced Intelligent Mechatronics (AIM)*, IEEE, Jul. 2016, pp. 614–620, ISBN: 978-1-5090-2065-2. DOI: 10 . 1109 / AIM . 2016 . 7576836.
- [34] J. Proctor and P. Holmes, 'Steering by transient destabilization in piecewise-holonomic models of legged locomotion,' *Regular and Chaotic Dynamics*, vol. 13, no. 4, pp. 267–282, 2008, ISSN: 14684845. DOI: 10.1134/S1560354708040047.
- [35] A. M. Hoover, S. Burden, X. Y. Fu, S. S. Sastry and R. S. Fearing, 'Bio-inspired design and dynamic maneuverability of a minimally actuated six-legged robot,' in *2010 3rd IEEE RAS and EMBS International Conference on Biomedical Robotics and Biomechanics, BioRob 2010*, 2010, pp. 869–876, ISBN: 9781424477081. DOI: 10 . 1109 / BIOROB . 2010 . 5626034.
- [36] U. Saranlı, A. A. Rizzi and D. E. Koditschek, 'Model-Based Dynamic Self-Righting Maneuvers for a Hexapedal Robot,' *The International Journal of Robotics Research*, vol. 23, no. 9, pp. 903–918, Sep. 2004, ISSN: 0278-3649. DOI: 10 . 1177 / 0278364904045594.
- [37] U. Saranlı, M. Buehler and D. E. Koditschek, 'RHex: A Simple and Highly Mobile Hexapod Robot,' Tech. Rep. [Online]. Available: [www.RHex.net](http://www.RHex.net).
- [38] C. Ordonez, N. Gupta, E. G. Collins, J. E. Clark and A. M. Johnson, 'POWER MODELING OF THE XRL HEXAPEDAL ROBOT AND ITS APPLICATION TO ENERGY EFFICIENT MOTION PLANNING,' in *Adaptive Mobile Robotics*, WORLD SCIENTIFIC, Sep. 2012, pp. 689–696. DOI: 10 . 1142 / 9789814415958{\\_ }0088.
- [39] C. S. Casarez and R. S. Fearing, *Steering of an Underactuated Legged Robot through Terrain Contact with an Active Tail*. 2018, ISBN: 9781538680940. DOI: 10.0/Linux-x86{\\_ }64.
- [40] D. W. Haldane, K. C. Peterson, F. L. Garcia Bermudez and R. S. Fearing, 'Animal-inspired design and aerodynamic stabilization of a hexapedal millirobot,' in *Proceedings - IEEE International Conference on Robotics and Automation*, 2013, pp. 3279–3286, ISBN: 9781467356411. DOI: 10 . 1109/ICRA.2013.6631034.
- [41] J. Zhang, G. Song, Y. Li, G. Qiao, A. Song and A. Wang, 'A bio-inspired jumping robot: Modeling, simulation, design, and experimental results,' *Mechatronics*, vol. 23, no. 8, pp. 1123–1140, 2013, ISSN: 09574158. DOI: 10.1016/j.mechatronics.2013.09.005.
- [42] N. Kohut, A. Pullin, D. W. Haldane, D. Zarrouk and R. S. Fearing, 'Precise dynamic turning of a 10 cm legged robot on a low friction surface using a tail,' in *2013 IEEE International Conference on Robotics and Automation*, IEEE, May 2013, pp. 3299–3306, ISBN: 978-1-4673-5643-5. DOI: 10 . 1109/ICRA.2013.6631037.
- [43] K. C. Galloway, J. E. Clark, M. Yim and D. E. Koditschek, 'Experimental investigations into the role of passive variable compliant legs for dynamic robotic locomotion,' in *Proceedings - IEEE International Conference on Robotics and Automation*, 2011, pp. 1243–1249, ISBN: 9781612843865. DOI: 10 . 1109 / ICRA . 2011 . 5979941.
- [44] A. Amoozandeh Nobaveh, J. L. Herder and G. Radaelli, 'A Compliant Continuously Variable Transmission (CVT),' *SSRN Electronic Journal*, 2022, ISSN: 1556-5068. DOI: 10 . 2139 / SSRN . 4248715. [Online]. Available: <https://papers.ssrn.com/abstract=4248715>.
- [45] Takaya Umedachi, Vishesh Vikas and Barry A. Trimmer, *HighlyDeformable 3-D Printed Soft Robot Generating Inching and Crawling Locomotions with Variable Friction Legs*. IEEE = Institute of Electrical and Electronics Engineers, 2013, ISBN: 9781467363570.
- [46] T. Umedachi and B. A. Trimmer, 'Design of a 3D-printed soft robot with posture and steering control,' in *Proceedings - IEEE International Conference on Robotics and Automation*, Institute of Electrical and Electronics Engineers Inc., Sep. 2014, pp. 2874–2879, ISBN: 9781479936854. DOI: 10 . 1109/ICRA.2014.6907272.
- [47] X. Sheng, H. Xu, N. Zhang, N. Ding, X. Zhu and G. Gu, 'Multi-material 3D printing of caterpillar-inspired soft crawling robots with the pneumatically bellow-type body and anisotropic friction feet,' *Sensors and Actuators, A: Physical*, vol. 316, Dec. 2020, ISSN: 09244247. DOI: 10.1016/j.sna.2020.112398.

- [48] A. M. H. S. Abeykoon<sup>1</sup>, K. O. Fellow and I. A. M. H. S. Abeykoon, ‘Changing the Centre of Gravity,’ Tech. Rep.
- [49] K. Skonieczny and G. M. T. D’eleuterio, ‘DETC2010-28482 IMPROVING MOBILE ROBOT STEP-CLIMBING CAPABILITIES WITH CENTER-OF-GRAVITY CONTROL,’ Tech. Rep., 2010. [Online]. Available: <http://www.asme.o>.
- [50] K. Yoshida and H. Hamano, ‘Motion dynamics and control of a planetary rover with slip-based traction model,’ in *Unmanned Ground Vehicle Technology IV*, vol. 4715, SPIE, Jul. 2002, pp. 275–286. DOI: 10.1117/12.474459.
- [51] C. A. Cao, D. K. Lieu and H. S. Stuart, ‘Dynamic Analysis of Gyroscopic Force Redistribution for a Wheeled Rover,’ in *Earth and Space 2021*, Reston, VA: American Society of Civil Engineers, Apr. 2021, pp. 318–327, ISBN: 9780784483374. DOI: 10.1061/9780784483374.032.
- [52] M. A. Chowdhury and M. Helali, ‘The effect of amplitude of vibration on the coefficient of friction for different materials,’ *Tribology International*, vol. 41, no. 4, pp. 307–314, Apr. 2008, ISSN: 0301679X. DOI: 10.1016/j.triboint.2007.08.005.
- [53] J. Wang, C. Liu, Y. B. Jia and D. Ma, ‘Ratchet rotation of a 3D dimer on a vibrating plate,’ *European Physical Journal E*, vol. 37, no. 1, 2014, ISSN: 1292895X. DOI: 10.1140/epje/i2014-14001-x.

# 3

## Research paper

In this chapter, the research paper is presented. The paper contains the main research of the thesis. It is written as an article and presents the design of the FARbot-s: a Frequency-Actuated Resonance robot with a steering mechanism. The paper contains the design process, experiments to validate the model, experiments to test the robot's performance and finally it is compared to other walking robots of similar size.

# Underactuated Compliant Resonant Walking Robot with Steering Mechanism

C.S. Lemmens

4720539

C.S.Lemmens@student.tudelft.nl

**Abstract** This paper presents the design of a steering mechanism for a small compliant resonant walking robot, called FARbot steering (FARbot-s). The FARbot-s is a frequency-actuated resonance robot that aims to achieve increased stride length at its resonance frequency and therefore higher efficiency. The paper discusses the methodology resulting in the design, including the idea of the steering mechanism and the simplified design of the FARbot-s. Two experiments are described to test the performance of the FARbot-s, a trajectory tracking to test the forward locomotion and steering mechanism and a velocity measurement to see if actuation amplification occurs at the eigenfrequency. The results of the experiments are presented, showing the trajectory changes according to the input frequency and the average velocity for different frequencies. The research is concluded by presenting a physical model with a forward locomotion and steering mechanism for an underactuated resonant robot.

## 1 Introduction

In recent years, there has been a growing interest in the development of autonomous, insect-like robots capable of rapid and agile movement. Due to their small size and lightweight nature, these robots possess a range of advantages over their larger counterparts, including the ability to navigate through confined spaces, climb obstacles, and withstand falls from heights. These features make them particularly suited for deployment in hazardous environments, such as collapsed buildings, natural disaster sites, and war zones, where larger robots are unable to operate[3, 9]. When equipped with advanced sensors, they have the capability to detect a range of hazards, including chemical toxicity and extreme temperatures, and aid in search and rescue operations by locating victims.

The current state-of-the-art small walking robots already show very promising results. Dash, a robot designed by Birkmeyer et al. [3], is 100 mm long robot and is able to climb over obstacles larger than its own body length, showing the potential to explore hazardous areas. Dash is able to remain functional after a fall height of 28 m, which demonstrates a great strength-to-weight ratio. Furthermore, Dash can achieve velocities of 15 body lengths per second (BL/s). Another robot which can achieve up to 15 BL/s is the iSprawl by Clark [4]. However, with almost 1.5 times the length and almost 20 times the weight (300 g) of Dash, it is very fast for such a hefty robot. The iSprawl also shows that it can walk

in different gaits. Then, Roach by Hoover et al[9] is a robot with a length of 3 mm and a velocity of 10 BL/s. Last, the Brusbots by Notomista et al.[16] presents small robots that propel by the use of vibration.

The main challenges for these robots are their complexity[4, 10, 17, 14], scale of efficiency[3, 8, 1], actuation[23], and manufacturing[18, 20]. The complexity of a robot is determined by the number of actuators and other parts, as well as the fabrication and assembly time, which ultimately leads to higher costs. Schonebaum has proposed a solution for the last three challenges with the design of the FARbot[19]: a Frequency Actuated Resonance robot. The FARbot has a compliant monolithic design and is designed in such a way that its first eigenmode is also the eigenmode of the horizontal leg movement. When a system is actuated with a frequency equal to the eigenfrequency the system is most power efficient. This results either in an increase of velocity for constant energy consumption or a reduction of energy consumption for the same velocity, reducing the scale of efficiency. Furthermore, it also implies that the FARbot only needs one actuator to move four legs. The FARbot's compliance contributes to its reduced part count, diminished wear, ease of design concerning resonance frequency, and the capability of efficient monolithic production.

A major limitation of the FARbot is the absence of a steering mechanism and its inability to propel itself. In order to use a robot for the tasks described earlier a forward locomotion and steering mechanism is important. Combined it results in the control of the direction of the robot. Having a minimum amount of actuators is a requirement in the FARbot design because, with the addition of each actuator, the complexity of the robot's design, control and cost are raised. A literature study showed that all the existing walking robots with a steering mechanism have at least two actuators or require some manual adjustments which require the robot to be stopped, in order to change legs. The research aims to design a compliant resonant walking robot (FARbot) capable of forward locomotion and steering without the need for additional actuators. The proposed FARbot design achieves both functionalities using a single actuator for propulsion and steering.

In Section 2 the methodology is described. The section begins with the concept of the FARbot-s' design, a simplified model of the FARbot-s and the implementation of this model in Simulink. Two experiments are described. The first experiment is to evaluate how the

Simulink model compares to the prototype and the second experiment is to test the steering mechanism itself. In Section 3 the results of the Simulink model and of the two experiments are presented. All the results and design choices are discussed in Section 4. This section also contains recommendations for future work. Finally, the conclusions are drawn in Section 5.

## 2 Methodology

This section presents the working principle of the steering mechanism and design of the FARbot-s, with its primary goal to have an increased stride length at the resonance frequency and a steering mechanism.

The section is structured as follows: First, the overview of the mechanical design is presented (Subsection 2.1). Second, the design process of the FARbot-s is described (Subsection 2.2). Finally, three experiments are presented to test the FARbot-s and its performance (Subsection 2.3).

### 2.1 Overview of the mechanical design

The mechanical design of the FARbot-s consists of two parts. A left stage and a right stage. Each stage has a feet pair attached. Different angles of the mechanical design can be seen in Figure 1.

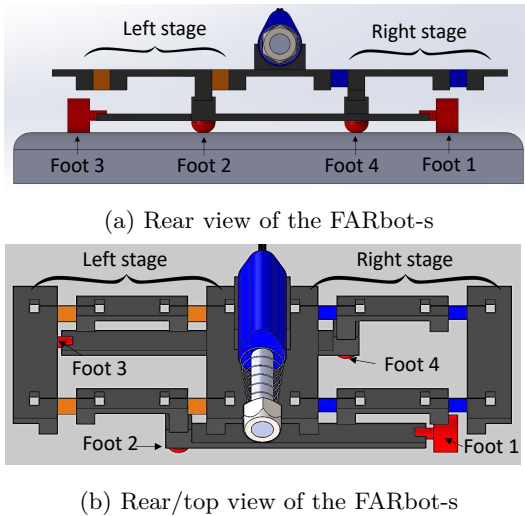


Figure 1: The right stage is marked by blue rectangles. The left stage is marked by orange rectangles. The coloured rectangles are leaf springs. The feet number is indicated with the black arrows. Feet 1 and 2 are connected to the left stage. Feet 3 and 4 are connected to the right stage.

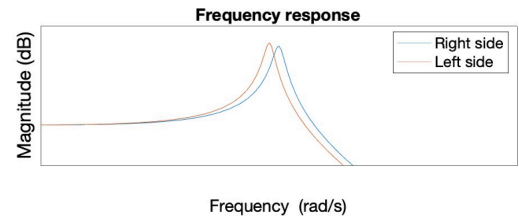
#### 2.1.1 Four feet

FARbot-s is designed with a quadrupedal feet configuration due to its inherent passive stability and the minimal leg count required for achieving it. To ensure stability, the robot must have at least three feet in contact with the ground. In terms of simplicity, having the fewest feet is preferred. While some insects and

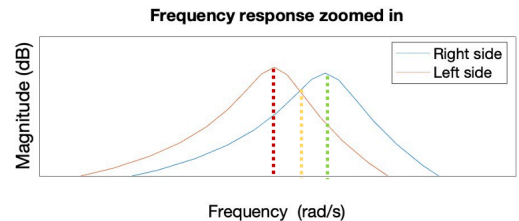
running robots utilise six feet to achieve a tripod gait, often perceived as necessary for stable locomotion, the cockroach *Periplaneta americana* challenges this notion. Despite having six legs, it switches to quadrupedal or bipedal running at higher velocities[7]. This demonstrates that four feet are sufficient for fast locomotion.

#### 2.1.2 Steering mechanism

At resonance, the amplitude is increased and occurs when the frequency of an applied periodic force is equal to the natural frequency of the system on which it acts. This phenomenon of resonance can be observed in Figure 2a. If the frequency of the applied force is matched to the natural frequency of the stride mechanism, an amplified stride can be expected, resulting in a bigger step. The concept of the steering mechanism of the FARbot-s is to have a different natural frequency for the left stride compared to the right stride. In simpler terms, when the frequency of the applied force is equal to the natural frequency of the left side, this side has a larger amplitude than the right. This asymmetry within the system can create an asymmetry in the legs' motion, which can result in the robot making a turn. The resonance peaks should be well-separated to exhibit different maximum amplitudes and frequencies. Simultaneously, they must be sufficiently close to generate an overlapping amplified magnitude frequency, which acts as the forward walking frequency. Consequently, the frequency of the actuator determines the trajectory of the FARbot-s.



(a) Frequency response of two example transfer functions. The left side has a lower mass resulting in a lower natural frequency.



(b) Frequency response zoomed in. The red dotted line shows the natural frequency of the left stage, the green dotted line shows the natural frequency of the right stage and the yellow line shows the intermediate frequency where both stages have an amplified magnitude.

Figure 2: Two frequency responses to demonstrate the concept of the steering mechanism. Subfigure (a) demonstrates two transfer functions with different masses and Subfigure (b) highlights the three different frequencies required for the steering mechanism.

### 2.1.3 Stride mechanism

The feet of the FARbot-s make a horizontal displacement which should be amplified at the resonance frequency. As a result, the front feet have a phase difference of  $180^\circ$  in translational direction and also the hind feet also have a phase difference of  $180^\circ$ , see Figure 3. The front and hind feet are moving in phase.

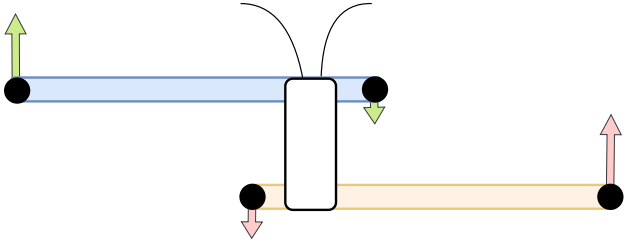


Figure 3: Motion of the four feet at resonance. The left front foot and right front foot are in antiphase, this also applies to the left hind foot and right hind foot.

## 2.2 Design process of FARbot-s

The design is split into steps to guide the reader through the design process. The process is split into six parts:

1. Actuation choice and kinematic model.
2. Steering mechanism.
3. Forward locomotion mechanism.
4. Compliant design.
5. Derivation the eigenmodes.
6. Couple motion and optimise parameters.

### 2.2.1 Actuation choice and kinematic design

The initial phase of the design process involves developing a kinematic model capable of achieving the intended output. The kinematic system should be designed in such a way that the eigenmode of the stride mechanism is a full body eigenmode. Designing a mechanism that utilises a full body eigenmode instead of higher eigenmodes of individual parts, such as feet, can offer several benefits. First, employing a full body eigenmode allows for the use of a single actuator to drive the desired motion of all four feet. By ensuring that the energy source operates at the eigenfrequency of the system, the robot can exhibit the intended motion. Second, from a manufacturing perspective, a full body resonance is advantageous, particularly in relation to production tolerances. Eigenfrequencies are sensitive to manufacturing errors, making it challenging for individual components to have precisely matching resonance frequencies[18, 2]. In contrast, utilising a full body resonance ensures that all four feet move at the same frequency, even if it differs slightly from the intended frequency due to manufacturing imperfections. This avoids undesirable running behaviour and facilitates consistent performance. Moreover, a full body eigenmode

with a greater generalised mass has the ability to store more energy in a resonant motion at the desired eigenfrequency and motion amplitude. Compared to individually resonating parts, a full body resonance has a higher generalised mass, which leads to increased kinetic and potential energy. This enhanced energy storage capacity contributes to improved performance. At last, the increase in kinetic and potential energies corresponds to greater inertial and elastic forces within the system. This characteristic makes the system relatively less sensitive to damping forces. As a result, the robot becomes more robust against energy dissipation due to damping, allowing for sustained motion and improved overall performance[19].

A linear solenoid generates the force required to enable one of the full body modes of the system. These kinds of solenoids are available in different sizes. As a rule of thumb, larger solenoids yield higher force capabilities, but they are also accompanied by increased weight due to their size. The solenoid used in the FARbot-s is designed to be used at 12 volts and 950 mA. Also, these kinds of solenoids generally do not have internal stiffness. Having zero stiffness allows for smoother and more responsive motion, improving accuracy and efficiency. The solenoid consists of a static coil and a moving pin.

The kinematic design consists of two parallelogram linkages, see Figure 4. The first four-bar linkage has bars 1, 5, 6 and 3, this is called the left stage. The second linkage has bars 2, 7, 8 and 3, this linkage is called the right stage. The linkages both have bar 3, which is called the base. The four-bar linkages prevent bars 1 and 2 from rotating and insures a rotational movement of bars 5, 6, 7 and 8 around the centre of the rotational joints. The moving pin is connected to the base with a translational spring. The static solenoid part is integrated in part 3 and the moving pin is part 4.

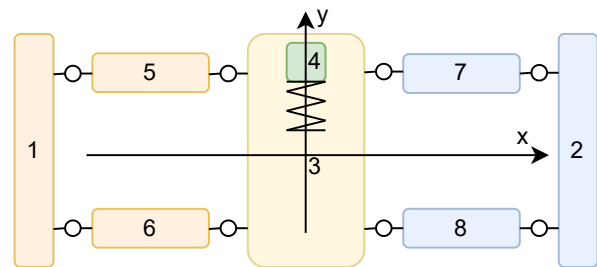
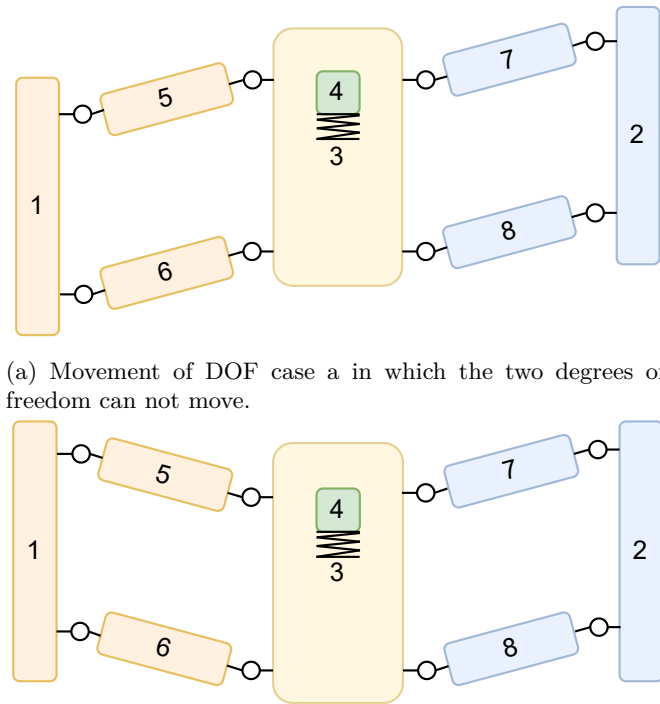


Figure 4: The kinematic model of the FARbot-s. The model consists of two parallelogram linkages (1,5,6 and 3) and (2,7,8, and 3). The bars are connected with rotational joints. The moving pin (4) is connected with a translational spring to the base bar (3).

The four-bar linkages can move in the negative and positive y-direction. So, the kinematic mechanism has two internal degrees of freedom (DOF), the left stage and the right stage. The two DOF of the kinetic mechanism are visible in Figure 5. Only one DOF configuration can be actuated since the stage can only move in the opposite

direction of the moving pin.



(a) Movement of DOF case a in which the two degrees of freedom can not move.

(b) Movement of DOF b in which the two degrees of freedom can move.

Figure 5: Only the movement visible in Subfigure b is possible since the stages only move in the opposite direction of the moving mass due to the accelerating forces.

### 2.2.2 Steering mechanism

Creating an asymmetry in the system as described in Subsection 2.1.2 will not result in a turn of the robot if the leg length is equal for both feet. Thus, the FARbot-s is equipped with asymmetric legs, as seen in Figure 6.

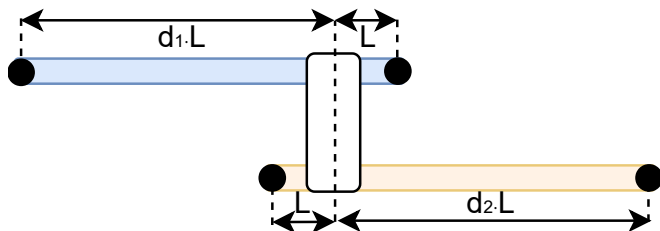


Figure 6: Asymmetric legs to create an asymmetry in the stride. The front feet pair is illustrated in orange and the hind feet pair is in blue. The black dot marks the position of the feet. The front left foot has a length of  $L$  and the front right foot has a length of  $d_1 \cdot L$ . This leg configuration is mirrored on the hind side. The hind left foot has a length of  $L$  and the hind right foot has a length of  $d_2 \cdot L$ .  $d_1$  and  $d_2$  are greater than 1 in order to create the asymmetry between the left and right side.

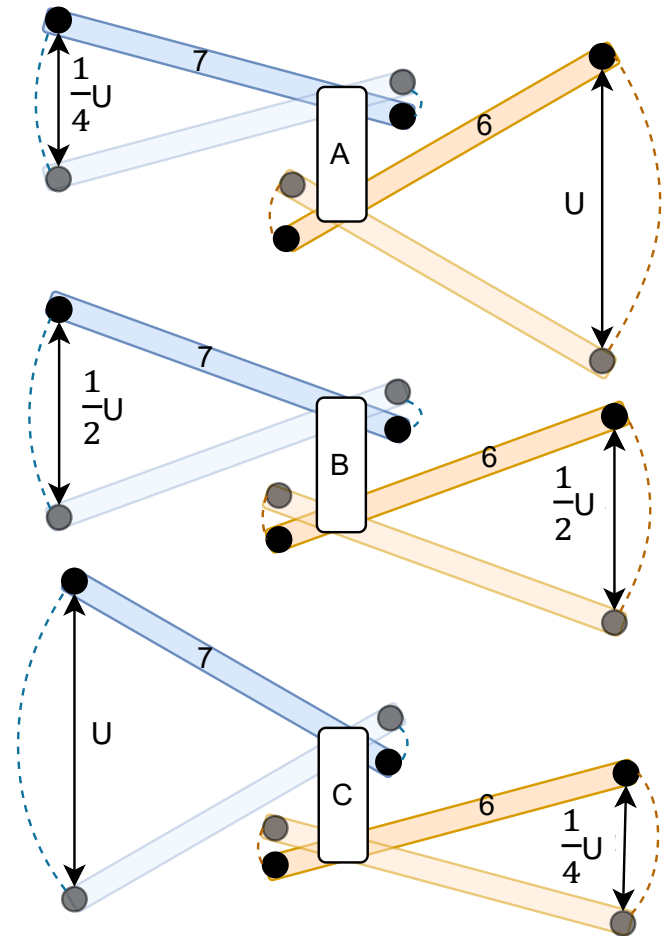


Figure 7: The front feet pair is connected to part 7 and the hind feet pair is connected to part 6. A) The periodic force is applied with a frequency equal to the natural frequency of the left stage. As a result, the displacement of the feet connected to the orange leg is greater than the displacement of the feet connected to the blue leg. B) the periodic force is applied with a frequency equal to the intermediate frequency. As a result, the displacement of the feet connected to the blue leg is equal to the displacement of the feet connected to the orange leg. C) The periodic force is applied with a frequency equal to the natural frequency of the right stage. As a result, the displacement of the feet connected to the blue leg is greater than the displacement of the feet connected to the orange leg.

With these asymmetric feet pair at the front and asymmetric feet pair at the back, the FARbot-s can make a turn if the actuator applies a periodic force with the same frequency as the natural frequency of the side. Figure 7 illustrates the legs combined with  $f$  resulting in a turn.

### 2.2.3 Forward locomotion mechanism

The forward locomotion mechanism of the FARbot-s is inspired by the locomotion mechanism of the Brushbot by Notomista et al.[16]. Notomista presents two models to

achieve forward locomotion, Regime I and Regime II. The Regime II model is valid for light robots and robots with stiff brushes i.e. not deformable feet, like in the case of the FARbot-s's feet. So, Regime II is most interesting for the forward locomotion design of FARbot-s. The Regime II model is based on on research work of Vartholomeos and Papadopoulos[21, 22].

The Regime II model is a mechanism used in brushbots to achieve forward locomotion. It is characterised by the use of light robots with stiff brushes that do not deform but rather act as pivot points for the robot to rotate. During the stick phase the robot body rotates around a pivot point, whereas in the slip phase the robot body rotates back to its initial orientation while sliding towards the desired direction. The motion provided by Regime II dominates when the robot has a high brush stiffness and a low mass. The model for Regime II predicts the robot's motion under the assumption that the robot body and the brushes are rigid bodies. The rotational inertia of the robot body around a point is used to simulate the interaction with the ground. The range of applicability of the model depends on the physical characteristics of the robot, such as the rigidity of the brushes, the mass of the robot, and the inclination of the brushes.

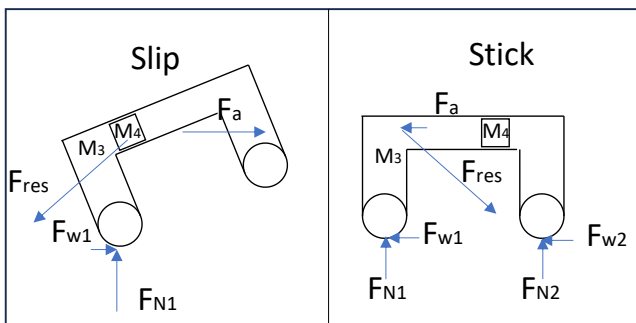


Figure 8: Free body diagrams of slip and stick phase.

In contrast to the conventional approach of employing rotational mass for the locomotion of Brushbots, this study presents an alternative mechanism by introducing a translating mass. The developed model replaces the rotational mass with a translating mass, taking into account the physical properties of FARbot and its interactions with the ground. A dynamic force analysis of the expected behaviour of the Regime II model with a translating mass is depicted in Figure 8.  $F_{res}$  is the resultant force resulting from the inertial force of mass  $M_4$ , the gravitational force of mass  $M_4$ , and the gravitational force of the rest of the robot. During the slip phase, the robot rotates around the front foot and skids along the ground, leading to a large inertial force,  $F_a$ , acting on the robot itself. Conversely, in the stick phase, the robot rotates back to its normal position. As it no longer slips, the friction forces increase, resulting in a smaller inertial force,  $F_a$ , acting on the robot itself. The process is repeated and as a result, a net displacement can

be expected.

Simulations to validate the proposed model are made using Working Model 2D software[5]. The 2D model can be seen in Figure 9. The simulations facilitate an analysis of the FARbot-s dynamics and performance, taking into account the translating mass. Visualisations and data analysis provided by the software offers valuable insights into the behaviour of the FARbot-s under different operating conditions.

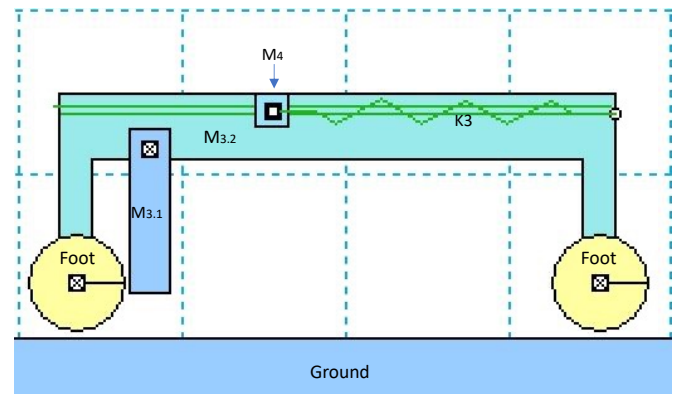


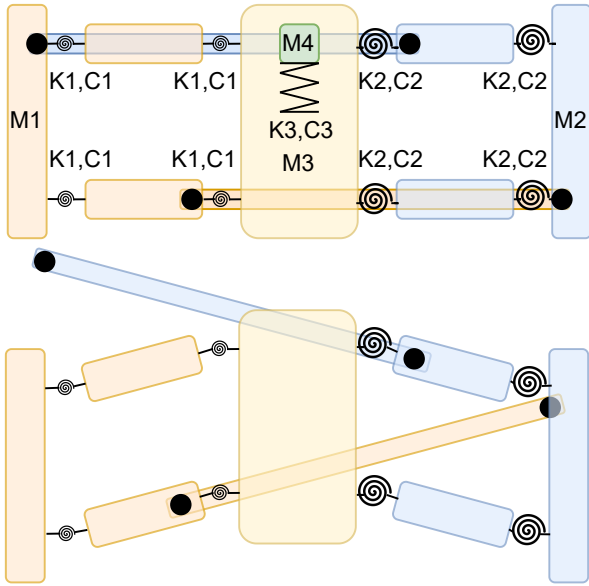
Figure 9: The 2D model has round feet that act as pivot points and are fixed to the body  $M_{3.2}$  so they can not rotate.  $M_{3.2}$  is the base and represents the geometry of the robot.  $M_{3.1}$  is used to change the centre of mass.  $M_4$  is the moving pin and is connected to Body  $M_{3.2}$  with a linear slider and spring  $K_3$ . A force whose magnitude is a sinus is applied to  $M_4$ .

## 2.2.4 Compliant design

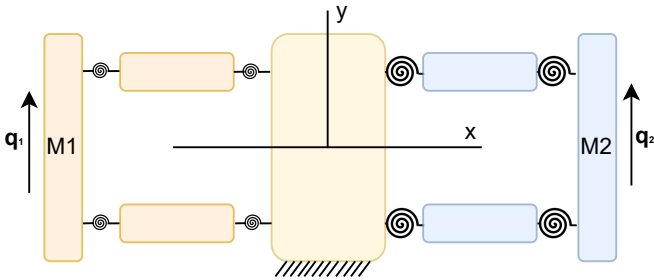
Converting the kinematic model into a compliant design has been achieved by replacing the kinematic joints with compliant flexures. Compliant leaf springs have been chosen, as they enable motion in the desired direction while providing stiffness for out-of-plane translation and rotation. Moreover, leaf springs possess a high stiffness-to-weight ratio. Additionally, leaf springs are straightforward to design for specific stiffness requirements and are easy to manufacture.

## 2.2.5 Derivation of the eigenmodes

The fifth part of the design process is to make a model which is able to calculate the eigenfrequencies. This model is made in Simulink[6] and the output shows the time and frequency response of the system. Using the frequency response, the output can be optimised to get the three frequencies desired for forward locomotion and the steering mechanism. The dynamic, model is based on the kinematic model described in Subsubsection 2.2.1. It consists of two sets of four rotational springs ( $K_1$  and  $K_2$ ) and four masses ( $M_1$ ,  $M_2$ ,  $M_3$  and  $M_4$ ), see Figure 10a.



(a) The top model is a visualisation of the dynamical model used to calculate the eigenfrequencies. The model is based on the kinematic model, but the rotational joints have been replaced with rotational springs. The masses of 1, 5, 6 and two feet are merged to a single mass M1, likewise for 2, 7, 8, and two feet. The mass of 3 is M3 and the mass of moving pin 4 is M4. The model is added to show how the stages move and the feet pair rotate.



(b) Changed version of the dynamical model so there are only two coordinates. Mass 4 and the spring are removed for clarification. Mass 3 is fixed to the ground. It is assumed there is no damping in the rotational springs.

Figure 10: Two versions of the dynamical model. Subfigure a is used to determine the Simulink model. Subfigure b is used to calculate the generalised stiffness matrix.

To create a Simulink model (Figure 11) of the dynamical system, the model has been simplified. The four rotational springs on each side have been simplified to one translational spring, named K1 and K2 in Figure 11. To calculate the values of K1 and K2, the generalised stiffness matrix has to be calculated. The generalised stiffness matrix results in the values of K1 and K2. In order to calculate the generalised stiffness matrix, the dynamical model is changed, such that there are only two generalised coordinates, see Figure 10b. This is done by fixing mass M3 to the ground and assuming there is no damping between the bars and the springs. Then the only two generalised coordinates are the horizontal

y-displacement of the left mass M1 and the horizontal y-displacement of the right mass M2. The generalised coordinates are  $q_1$  and  $q_2$ , respectively.

**Kinetic energy** The kinetic energy  $T$  of the system can be calculated with the following equation:

$$T = \frac{1}{2} \dot{\mathbf{x}}^T \mathbf{M} \dot{\mathbf{x}} \quad \text{with} \quad \dot{\mathbf{x}} = \dot{\mathbf{x}}(\mathbf{q}, \dot{\mathbf{q}}) \quad (1)$$

Here  $\mathbf{M}$  is the diagonal mass matrix. There is no inertia component in the mass matrix since mass M3 is fixed and both masses M1 and M2 only have translational DoF.  $\dot{\mathbf{x}}$  is a function of the position vector  $\mathbf{q}$  and the first time-derivative of the position vector.

**Potential energy** The gravitational energy does not influence the potential energy of the system, because gravitational forces do not act in the horizontal plane. Therefore, only the elastic potential energy is considered. To calculate the elastic potential energy the stiffness of the springs has to be determined. As mentioned before in Subsubsection 2.2.4, the FARbot-s is compliant and has flexures that act as leaf springs. The stiffness of a flexure can be approximated with the pseudo-rigid-body model (PRBM) as described by Howel et al.[11]. The torsional stiffness of a flexure can be calculated with the following equation:

$$K_\theta = \frac{EI}{L} \quad (2)$$

Where  $E$  is Young's modulus,  $I$  is the moment of inertia of a rectangle, and  $L$  is the length of the flexure. The potential energy can be calculated with the following equation:

$$V = \frac{1}{2} 4\theta^T \mathbf{K}_\theta \theta \quad \text{with} \quad \theta = \theta(\mathbf{q}) \quad (3)$$

Where  $\theta$  is the angle of the displacement of the generalised coordinate and can be calculated with the following equation:

$$\theta = \arcsin\left(\frac{q}{L_i}\right) \quad (4)$$

$K_\theta$  is the diagonal torsional stiffness matrix.  $L_i$  is the length of the horizontal bar plus twice half the length of the flexure.

**Equation of motion** The equation of motions of the system can be calculated with the Lagrange equation:

$$\mathbf{f} = \frac{d}{dt} \frac{\partial T}{\partial \dot{\mathbf{q}}} - \frac{\partial T}{\partial \mathbf{q}} + \frac{\partial V}{\partial \mathbf{q}} = 0 \quad (5)$$

**Generalised stiffness matrix** The Lagrange Equation 5 can be used to calculate the generalised stiffness matrix:

$$\mathbf{K}_g = \left. \frac{\partial \mathbf{f}}{\partial \mathbf{q}} \right|_{\dot{\mathbf{q}}=\ddot{\mathbf{q}}=0} \quad (6)$$

The generalised stiffness matrix is calculated by taking the partial derivative of  $\mathbf{f}$  with respect to the generalised coordinate  $\mathbf{q}$ . Since the kinetic energy is only dependent on the derivative of  $\mathbf{q}$  Equation 6 can be simplified to:

$$\mathbf{K}_g = \left. \frac{\partial}{\partial \mathbf{q}} \frac{\partial V}{\partial \dot{\mathbf{q}}} \right|_{\dot{\mathbf{q}}=\ddot{\mathbf{q}}=\mathbf{q}=0} \quad (7)$$

The diagonal of the generalised stiffness matrix results in the value K1 and K2 which can be used as the stiffness of the springs of the Simulink model in Figure 11.

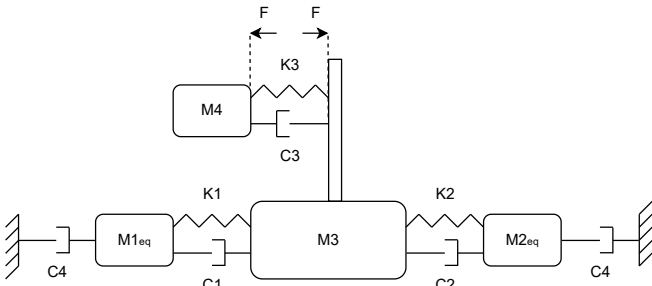


Figure 11: Simplified 1D dynamical simulink model. The base mass M3 has two stages M1<sub>eq</sub> and M2<sub>eq</sub> connected with springs and dampers. The moving mass M4 is also connected with a spring and damper. The force excited by the solenoid acts between the mass M3 and M4. The damper C4 represents the friction between the ground and the robot.

The coordinates of moving masses do not align with the location of the generalised coordinate. The location of the CoM can either increase or decrease the effect on the equivalent mass. Additionally, the parts between the rotational springs and the feet have an inertia component due to their rotation, which introduces an additional mass element. By considering both translations and the mass moment of inertia, an equivalent mass can be calculated, representing the accurate mass of the physical model. The values of the equivalent mass M1<sub>eq</sub> and M2<sub>eq</sub> can be found in Table 1. The calculation of the equivalent masses can be found in Appendix G.

The input of the applied force F can be set to a chirp signal. When measuring the displacement of all the masses as an output signal, the time response will be the output. The frequency response can be calculated by applying the Fast Fourier Transform (FFT) to the time response output. The frequency response shows the range of frequencies and the amplitude, at the location of the peak there is an eigenfrequency.

The damping coefficients, denoted as C1, C2, and C3, have been selected as such to optimize the interpretability and clarity of the results obtained from the Simulink model. Their respective values can be seen in Table 1.

## 2.2.6 Couple motion and optimise parameters

The steering mechanism of the robot operates on three distinct frequencies, each associated with the eigenfrequencies of the individual stages. The first frequency corresponds to the eigenfrequency of the left stage, while the second frequency represents an overlapping frequency between the eigenfrequency peak of the left and right stage. The third frequency corresponds to the eigenfrequency of the right stage. By selectively switching between these eigenfrequencies, the robot can achieve trajectory changes during its motion.

To find the optimal design parameters of the FARbot-s, several parameter sweeps are carried out. This iterative process identifies the most influential parameters affecting the frequency response. These influential parameters are then used to determine the optimal parameter configuration through an iterative process.

To fully harness the capabilities of the steering mechanism, it is combined with the forward locomotion mechanism of Regime II. The Regime II mechanism, characterised by the use of stiff feet as pivot points, offers an efficient and reliable means of achieving forward motion. By integrating the steering mechanism with the Regime II mechanism, the robot can simultaneously control its trajectory while maintaining forward locomotion. This combination enables the robot to exhibit not only the ability to change direction but also the capability to continue moving forward during trajectory adjustments.

The optimisation of integrating the steering mechanism with the Regime II forward locomotion is carried out by examining the rotation of the robot resulting from the Regime II mechanism. Simultaneously, a parameter sweep analysis is conducted using the Simulink model to explore the effect of different parameter sets on the robot's performance. By systematically varying the parameters related to mass distribution, flexure stiffness, and leg length, the Simulink model together with the working 2D model allows for a comprehensive evaluation of the robot's behaviour under various configurations. The optimisation process involved iteratively testing different parameter combinations and determining their impact on the robot's trajectory. By identifying the parameter set that yields the best results, considering both the rotation induced by the Regime II mechanism and the Simulink model simulations, the optimised design and parameter values are determined, ensuring the robot's optimal performance and manoeuvrability.

## 2.3 FARbot-S design and experiments

The 3D design of the FARbot-s can be seen in Figure 12. The blue flexures are the right stage, the orange flexures are the left stage. The final parameters of FARbot-s are shown in Table 1.

Table 1: Overview of the final parameters of the final design of the FARbot-s

Name	Value	Unit	Description
$T_{flex1}$	0.100	mm	Thickness flexure 1
$T_{flex2}$	0.150	mm	Thickness flexure 2
$H_{flex1}$	6.00	mm	Height flexure 1
$H_{flex2}$	5.10	mm	Height flexure 2
$L_{flex1}$	5.00	mm	Length flexure 1
$L_{flex2}$	5.00	mm	Length flexure 2
$E_{steel}$	183e9	Pa	Young's modules flexure
$L_{intermediate}$	30.0	mm	Length of the intermediate part
$d_1$	8.00	-	Length of feet 1
$d_2$	9.33	-	Length of feet 3
$L$	7.5	mm	Length of feet 2 and 4
$M1_{eq}$	15.6	g	equivalent mass of left stage
$M2_{eq}$	20.0	g	equivalent mass of right stage
$M_3$	17.0	g	Mass of base
$M_4$	10.2	g	Mass of moving pin
$C_1$	0.0100	Ns/m	Damping coefficient spring mechanism 1
$C_2$	0.0150	Ns/m	Damping coefficient spring mechanism 2
$C_3$	0.250	Ns/m	Damping coefficient spring mechanism 3
$C_4$	0.750	Ns/m	Damping coefficient of ground on FARbot-s
$K_3$	130	N/m	Stiffness spring 3

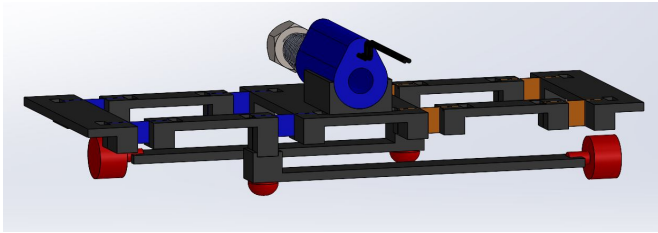


Figure 12: View of the final 3D design of the FARbot-s. The blue flexures indicate the stiffer flexures. The orange flexure indicates the softer flexures. The solenoid static part is illustrated in blue and the moving pin is indicated with light grey. The feet are mounted underneath the intermediate part.

An experiment must be carried out to validate whether or not the Simulink model is a adequate representation of the physical model. The Simulink and physical model input is a chirp signal. The displacement of the two stages and the base is measured with three ptoNCDT ILD1302-20 lasers. The physical model is mounted in the test setup in such a way that the only permissible motion is in the direction of the solenoid actuation direction, while the other five degrees of freedom (DoF) are constrained. The results of the Simulink model are compared to the results of the Physical model. A picture of the experimental setup can be seen in Figure 13.

The validation of the Simulink model is carried out with the physical model in the air. Because, if the physical model would be on the ground the robot would want to start walking and this behaviour is not modelled in the Simulink model. Therefore, another experiment

has been designed in order to find the relation between damping and friction and input gain and voltage. An aluminium plate is pressed perpendicular to the feet to emulate the ground. A mass connected to the plate can be varied in order to increase or decrease the friction force. This experiment is described in Appendix B and led to the value of the damping coefficient  $C_4$  which can be seen in Table 1.

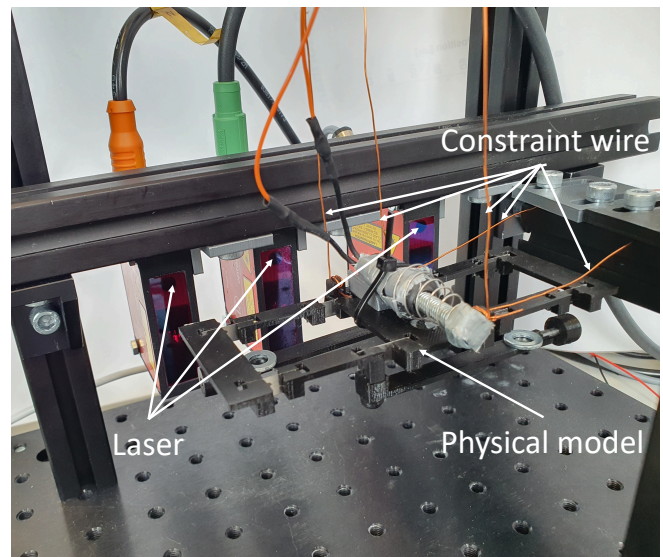


Figure 13: Test setup to compare Simulink results to the physical model. The setup contains three laser modules used to measure the displacement and the physical model constrained by wires.

The performance of FARbot-s depends on two tasks.

The first and most important task is its ability to adjust its trajectory in response to the actuation frequency of the solenoid. The second task is to achieve forward locomotion.

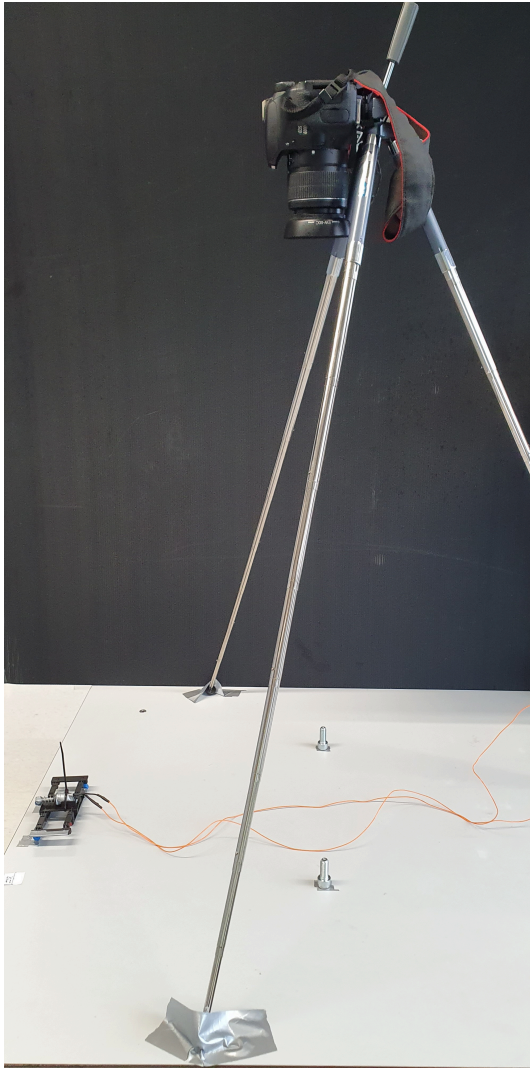


Figure 14: Picture of the experimental setup to test trajectory of FARbot-s. The camera is mounted on a tripod and points perpendicular to the surface. The starting position of the trajectory plot is marked so the FARbot-s starts walking from the same starting position. The two bolts are added to emulate obstacles.

An experiment is designed to assess the performance of the FARbot-s in executing these tasks. To track the trajectory of the FARbot-s, a camera is positioned above the surface on which the robot walks, pointing perpendicular to the surface, see Figure 14. The solenoid is set to a specific frequency, generating a sinusoidal input. Recording starts when power is supplied to the FARbot-s. The experiment is carried out at specific frequencies with increments of 1 Hz. The trajectory tracking of the FARbot-s is achieved by video tracking software which analyses the recordings. The video tracking software used is Kinovea[12]. This software will

enable the full trajectory spectrum to be determined. This analysis helps determine if the FARbot-s can achieve forward locomotion and make turns. Additionally, obstacles were added, around which the FARbot-s has to navigate, emulating rough terrain.

Furthermore, considering the FARbot-s is designed to operate at its eigenfrequency an experiment is carried out to measure the velocity of the FARbot-s for different frequencies.

### 3 Results

The result section is divided into five subsections, which present the physical model (Subsection subsection 3.1), the validation of the Simulink model (Subsection 3.2), the findings of the Simulink model (Subsection 3.3), the results of the working model in 2D along with the visualisation of forward locomotion (Subsection 3.4), and the outcomes of the trajectory experiment (Subsection 3.5).

#### 3.1 Physical model

The physical model can be seen in Figure 15. The black parts are 3D-printed with a Fused Deposition Modeling (FDM) printer. The parts are connected with leaf springs made from spring steel. The solenoid is Heschon HS-0530B and is modified to save mass. The modifications made to the solenoid are the removal of the metal casing, the replacement of the standard spring with a stiffer spring and the fabrication of a new moving pin.

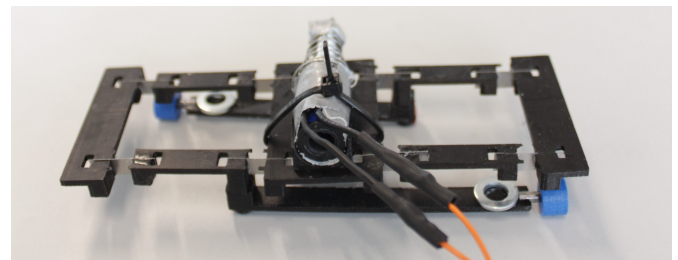


Figure 15: Picture of the physical model. The rigid parts are black and the solenoid is grey.

#### 3.2 Model validation

The output of the Simulink model and the physical model are both a time response. However, for the design of the FARbot-s, it is important to know the frequency response. Therefore, the output data of both results have been transferred with a FFT. Furthermore, the results of the physical model have been filtered with a moving average filter, because it increases the readability of the results. The window length of the moving average filter is 100 points. The results of both experiments can be seen in Figure 16. Both chirp signals start at 1 Hz and go up to 25 Hz.

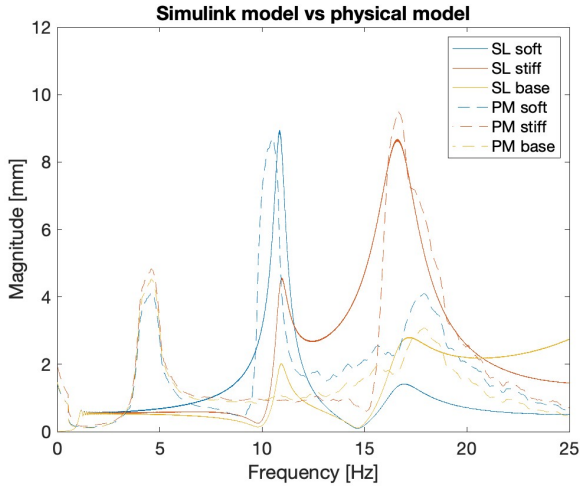


Figure 16: Frequency response of chirp signal of Simulink results and frequency response of chirp signal of the physical model. A magnitude amplification can be observed around 5 Hz, 10 Hz and 17 Hz.

### 3.3 Parameter selection

An optimal parameter configuration has been found by iterating the parameters and looking at the output of the Simulink model. The frequency response of the feet for the parameters given in Table 1 can be seen in Figure 17. A magnitude amplification can be observed from 15 to 35 Hz.

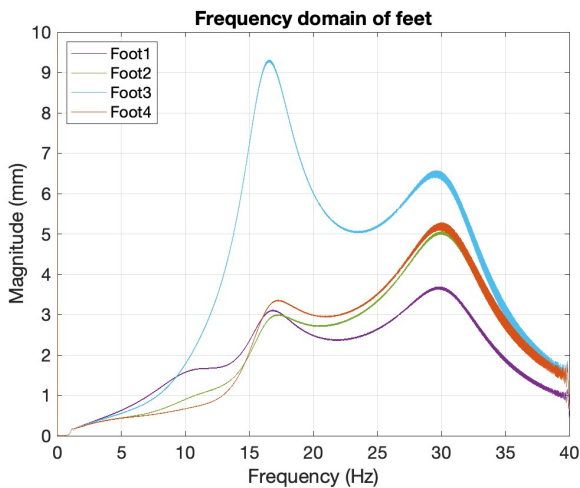


Figure 17: Frequency response of feet FARbot-S

The results of the damping versus friction and the gain versus voltage experiments can be found in the supplementary materials.

### 3.4 Results forward locomotion

The Working Model 2D model results can be seen in Figure 18. In the figure, two solenoid periods have been depicted. The top figure shows the net displacement of the model. This is in general a linear dissent which represents a constant velocity. The results are similar to

the Regime II model described by G. Notomista et al.[16]. The bottom figure shows the net rotation of the model. It shows a periodic movement. The masses of the model are based on the parameters mentioned in Table 1.

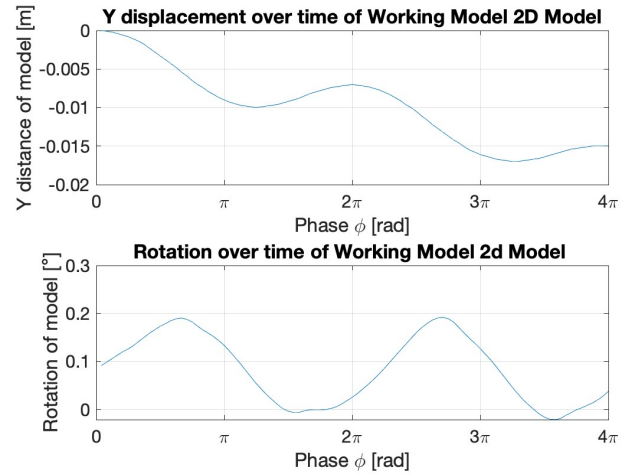


Figure 18: Output of Working Model 2D model. The top figure shows the y-displacement of the model over the phase. The bottom figure shows the rotation of the model.

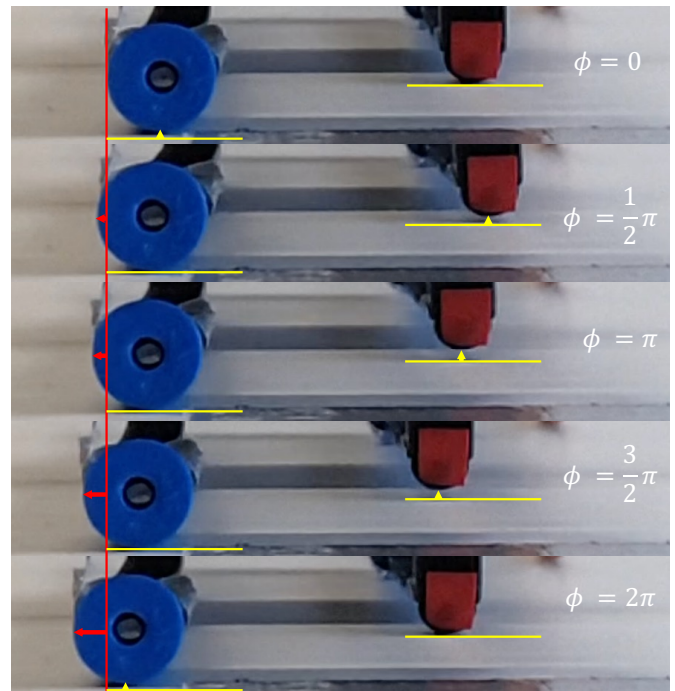


Figure 19: One period of the solenoid sinus at phase 0,  $\frac{1}{2}\pi$ ,  $\pi$ ,  $\frac{3}{2}\pi$ , and  $2\pi$  at  $f=21$  Hz, ordered from top to bottom. Showing the forward motion and rotation of the physical model. The red arrows indicate horizontal displacement, and the yellow arrows indicate vertical displacement.

The forward locomotion of the FARbot-s is also observed with the physical model. Figure 19 shows one

period of the solenoid sinus ( $0$ ,  $\frac{1}{2}\pi$ ,  $\pi$ ,  $\frac{3}{2}\pi$ , and  $2\pi$ ) at  $f=21$  Hz. The five time frames of the figure are taken from video recordings. The recordings were taken at 960 frames per second (fps), which is well above the input frequency of  $f=21$  Hz. The video is slowed down 32 times in order to analyse the video. The figure shows that within one period there is forward displacement and a rotation of the physical model. The rotation can be observed by the vertical displacement of the front feet during the time frame  $\frac{1}{2}\pi$  and the vertical displacement of the hind feet during the time frame of  $\frac{1}{2}\pi$ ,  $\pi$ , and  $\frac{3}{2}\pi$ .

### 3.5 FARbot-s performance results

The experimental setup to track the trajectory can be seen in Figure 14. The setup contains the FARbot-s, a tripod and a camera. The solenoid wire is held by hand during the experiment. To ensure there is minimum influence of the wire on the trajectory, the wire length is long and is held roughly above the robot during movement. The starting position of the FARbot-s during the experiment is in the identical location for every frequency, marked on the table by tape. The experiments are carried out on the same high pressure laminate (HPL) surface. The surface finish of this material is smooth.

The result of the first experiment can be seen in Figure 20. The figure shows trajectories of different frequencies. The trajectories are the output of the video tracking. It is clear that the trajectory changes according to the input frequency. However, the direction of the measured trajectory is mirrored compared to the designed direction. This will be further discussed in Subsection 4.3.

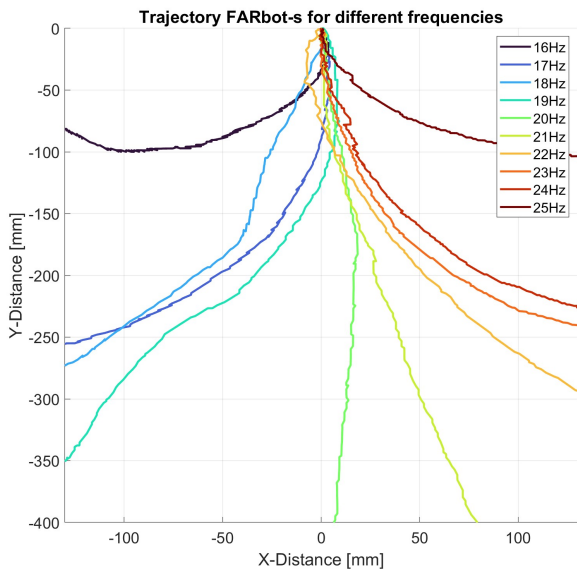


Figure 20: Trajectory of FARbot-S on HPL for different solenoid input frequencies. The frequency ranges from 16 to 25 Hz in steps of 1 Hz.

The results of the second experiment can be seen in Figure 21. The experiment contained the objective of

FARbot-s completing the obstacle course. The obstacle course has two bolts and the FARbot-s has to make a right turn around one bolt and a left turn around the other.

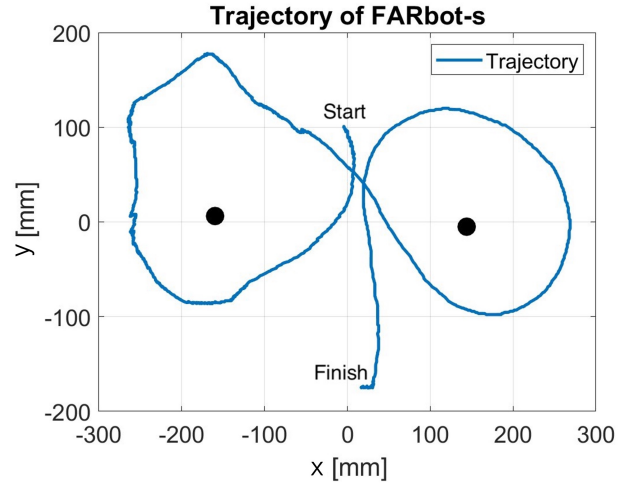


Figure 21: Trajectory of FARbot-S on the obstacle course, containing one left turn and one right turn. The black dots mark the obstacle.

The results of the third experiment can be seen in Figure 22 and show the average velocity for different frequencies. The experiment contains more data points around the eigenfrequency range to achieve a better resolution. The maximum velocity is  $80 \text{ mm}\cdot\text{s}^{-1}$ , which is equal to 1.5 body lengths per second (BLs<sup>-1</sup>).

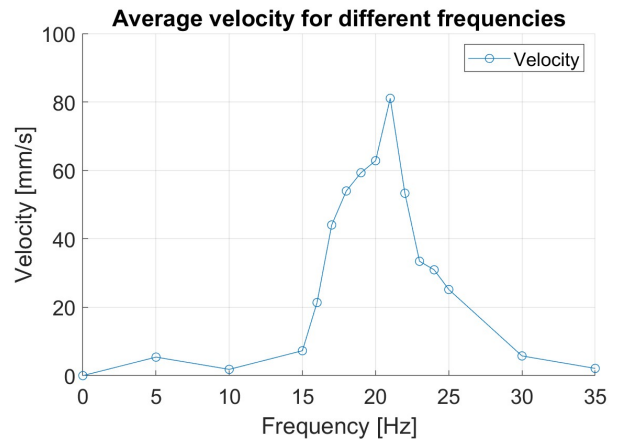


Figure 22: Velocity of FARbot-s for different frequencies. Overall the frequency step size is 5 Hz. However, between 15 and 25 Hz the step size is 1 Hz.

## 4 Discussion

This section discusses the results of the FARbot-s parameter selection (Subsection 4.1). Furthermore, the model validation is discussed (Subsection 4.2). Additionally, the steering mechanism is analysed (Subsection 4.3). Furthermore, the performance of the

FARbot-s is discussed (Subsection 4.4). Finally, potential improvements and future work are discussed (Subsection 4.5 and 4.6).

## 4.1 Parameter selection

During the parameter selection phase, multiple parameter sweeps are conducted, revealing the varying degrees of importance among different parameters. Notably, changes in the mass of the base have a less significant impact on the frequency response compared to alterations in the mass of one of the stages. The parameter sweep shows that the eigenfrequency of the moving pin exerted the most influence on the system, which is to be expected as it is the mass responsible for initiating the vibrations in the system. To provide context, when the eigenfrequency of the solenoid closely matches that of one of the stages, the amplitude peak of the stage becomes significantly amplified compared to cases where the eigenfrequency of the solenoid is much higher or lower than the one of the stage. This observation leads to the design choice of designing the remaining parameters around the mass of the moving pin and the stiffness of the spring connecting the pin to the base. This results in the tuning of the eigenfrequency of the stages, taking into account the necessary mass of the rigid components to be stiff, as well as the stiffness of the springs i.e. flexure stiffness.

## 4.2 Model validation

The results presented in subsection 3.2 show an overlap between the Simulink model and the physical model. The resonance peak of the left stage at around 10 Hz and the right stage at around 17 Hz, match the Simulink model. However, the resonance peak at 5 Hz can not be seen in the Simulink model. This resonance peak is due to the resonance of the constraining method.

## 4.3 Steering mechanism

As mentioned in subsection 3.5 the measured trajectory is mirrored compared to the designed direction. It is possible that the steering mechanism functions differently than originally expected. A change in mass moment of inertia might be a possible explanation for the behaviour of the steering mechanism. For one solenoid period, the moving pin moves in and out. The mass moment of inertia is smaller when the pin is inwards compared to when the pin is outwards. The net contribution of the other inertia forces during one solenoid period is zero. However, for the first half of the solenoid period ( $0$  to  $\pi$ ) the mass moment of inertia of the robot is lower making it easier for the robot to rotate, compared to the second half of the solenoid period when the mass moment of inertia is higher.

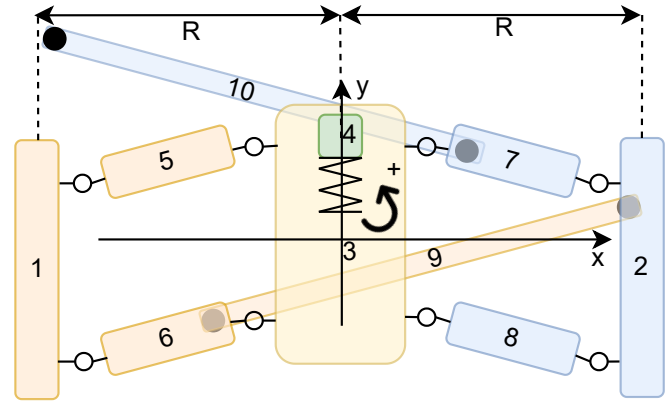


Figure 23: Illustration used to calculate the inertia forces. The inertia forces of parts 1, 2, 9 and 10 are used because the other forces are very small or do not contribute to a net moment in the horizontal plane.

To further validate this hypothesis a force analysis has been carried out using the Simulink model. The analysis is done at the three most distinct trajectory frequencies, 16, 20 and 25 Hz. All the moving parts experience inertia force during movement (1 till 10), see Figure 23. However in order to simplify the analysis the small inertia forces are neglected, therefore the inertia forces of parts 5, 6, 7 and 8 are neglected. Furthermore, only the inertia forces that contribute to a net moment in the horizontal plane are considered, thus the inertia forces of parts 3 and 4 are not considered. The force analysis consists of the inertia force 1, 2, 9 and 10. The moment generated by the inertia force of parts 1 and 2 can be calculated with the following equation:  $M = maR$  since these masses have a translational acceleration. Here  $m$  is the mass of the part itself and  $a$  is the acceleration of the part. The acceleration can be calculated by taking the second derivative of the displacement, given by the Simulink model. Multiplying the force  $F$  by the length  $R$ . The moment around the centre of the base can be calculated. The inertia moment of parts 9 and 10 can be calculated with the following equation:  $M = I\alpha$  since these masses have a rotational acceleration. Here  $I$  is the mass moment of inertia of the part and  $\alpha$  is the rotational acceleration, which is the second derivative of the rotation. The rotation is given by the Simulink model.

The four moments during one solenoid period can be seen in Figure 24. The input frequency of the solenoid is 16 Hz. By taking the integral of the moment lines from  $0$  to  $\pi$  and summing the four moments the net moment can be calculated for the first half of the solenoid period. For 16 Hz the net moment over half a solenoid period is  $T_{16Hz} = -0.1017 \text{ e-3 Nm}$ . This negative moment corresponds with a clockwise rotation.

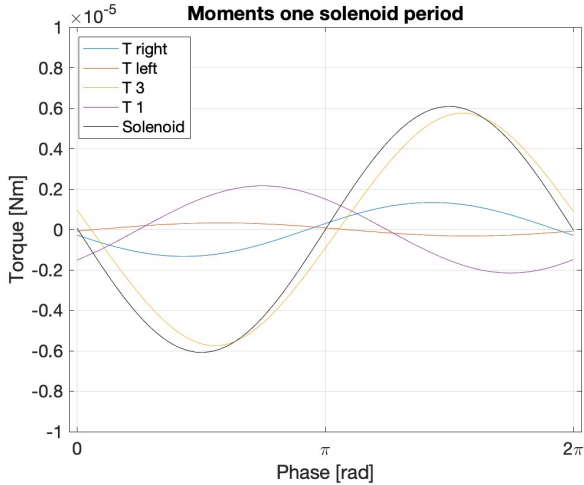


Figure 24: The four moments generated by inertia of the feet and stages over one solenoid period. The input frequency of the solenoid is 16 Hz.

The same process can be repeated for the frequency of 20 Hz and 25 Hz. For 20 Hz the sum of the net moment over half a solenoid period is equal to  $T_{20Hz} = -0.4522e-04$  Nm, which corresponds to a clockwise rotation, but with a reduced magnitude compared to the moment of 16 Hz. The sum of the net moment at 25 Hz over one solenoid period is  $T_{25Hz} = 0.2166e-05$  Nm, which corresponds to a counterclockwise rotation.

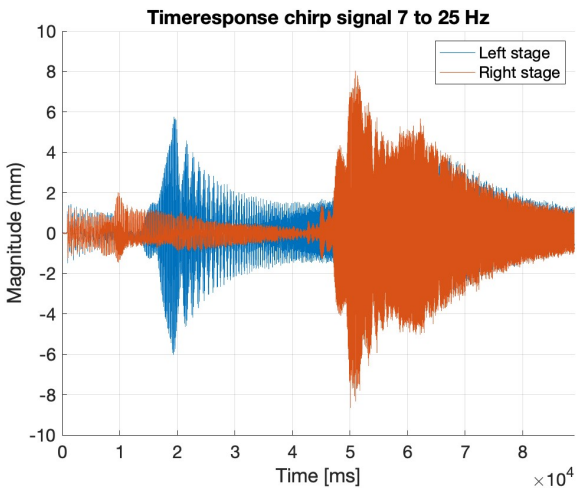


Figure 25: Time response of the physical model of a chirp input to the solenoid. The left stage and right stage are measured.

The hypothesis can further be validated by an additional experiment showing that inertia forces can be the main cause of steering the robot. It is possible to see this phenomenon when looking at the time response of the physical model. The time response can be seen in figure Figure 25. The figure shows the time response of the left stage and the right stage of an applied chirp signal. The eigenfrequency peak of the left stage is around  $2.0 e4$  ms

and the eigenfrequency peak of the right stage is around  $5.1 e4$  ms. Summing the magnitude of both stages for the time frame of the peak can give an indication if the FARbot-s is rotating i.e. there is a change in net moment. The results of the summation can be seen in Table 2.

Table 2: Results of summation time response for a specific time frame.

Time frame [ms]	Sum left stage [mm]	Sum right stage [mm]
$1.7e^4 - 2.1e^4$	-36.2	0.887
$4.9e^4 - 5.5e^4$	65.3	-46.9

The results show a clockwise rotation at the eigenfrequency of the left stage and a counterclockwise rotation at the eigenfrequency of the right stage. The same rotational directions as the results from the Simulink model. The direction of rotation generated by the inertia forces matches the trajectory direction of the physical model.

However, it is essential to note that in the Simulink model and in the experiment with the physical model influence of friction is not considered. It remains unknown if the interaction with the ground has an influence on the trajectory of the FARbot-s. In further research, an experiment which also tests the influence of friction would further validate the hypothesis. For this experiment, the FARbot-s still has to be constrained because the laser modules have to measure the displacement of the stages. However, the feet are going to allow for a net displacement so the ground surface has to move. This can be done with a surface which moves parallel to the forward locomotion direction, for example, a small treadmill.

#### 4.4 FARbot-s performance

The results presented in subsection 3.5 demonstrate that the FARbot-s is capable of adjusting its trajectory based on different input frequencies. Notably, the FARbot-s exhibits distinct turning radii, which can be effectively utilised, as evident in the obstacle scenario. The robot demonstrates proficient navigation around objects. Additionally, the results indicate that the FARbot-s' walking frequency aligns with its eigenfrequency, as there is a significant increase in velocity around this frequency.

The performance and dimensions of the FARbot-s are compared to other walking robots with similar dimensions. The comparison can be seen in Table 3. The FARbot-s scores well when looking at the size-to-weight ratio. The turning radius is also small compared to robots of the same size, which is preferred. FARbot-s is the only small walking robot which uses a single actuator. The forward velocity of the FARbot-s is a lot less compared to other walking robots. However, achieving high  $BLs^{-1}$  was not the focus of this research.

Table 3: Comparison of small walking robots with steering mechanism. \* is an unknown parameter.

Robot	Size [L-W-H] [mm]	Mass [g]	Turning radius [mm]	Actuators	Velocity [BLs <sup>-1</sup> ]
ROACH [9]	30-*-*	2.40	25	2	1
DASH[3]	100-100-50	16.0	200	2	15
octoROACH[17]	100-45-30	35.0	330	2	3.8
Mini-Whegs[15]	90-68-20	146	178	2	10
MEDIC[13]	55-53-18	55.0	27	4	*
i-Sprawl[4]	155-116-70	300	230	3	15
FARbot-s	55-135-32	41.6	100	1	1.5

## 4.5 Wire influence

The wire connecting the solenoid to the power source plays a crucial role in determining the performance of the FARbot-s. The wire possesses inherent characteristics such as mass and stiffness that can significantly influence the trajectory of the FARbot-s when subjected to rotation or translation. In an attempt to understand the impact of the wire, various experiments are conducted.

Initial trials involve fixing the wire at a high point or allowing it to rest on the ground, which unexpectedly results in an inferior performance of the FARbot-s. These findings lead to the realisation that the wire's positioning and movement during the experiments are critical factors. To address this, it was decided that the wire will be held by hand to ensure greater control and stability.

However, it is important to note that even during manual handling, any unintended movement or rotation of the wire in a direction contrary to the desired trajectory of the FARbot-s can potentially alter the outcome of the experiments. Hence, maintaining a synchronized motion between the wire and the FARbot-s' intended path is essential to minimise any disruptive effects.

To further minimise the influence of the wire on the FARbot-s' performance, a longer wire length is chosen. By increasing the wire length, it is expected to reduce the likelihood of abrupt changes in trajectory caused by any slight disturbances or vibrations along its path. This decision aims to enhance the reliability and consistency of the experimental results, allowing for a more accurate analysis and evaluation of the FARbot-s' performance.

When considering the future design of the FARbot-s, the feasibility of incorporating the power source and control mechanisms onboard is deliberated. This approach eliminates the need for an external wire connection and provides greater autonomy to the robots. However, for the current design, this option is not pursued due to the potential increase in weight. Adding the power source and control mechanisms onboard can significantly impact the FARbot-s' agility and manoeuvrability, which is crucial for its performance. Therefore, for the sake of maintaining optimal weight-to-performance ratios, it is decided to retain the external wire connection in the present design while acknowledging the possibility of exploring alternative power and control solutions in future iterations. For the research, it was clearer to have

the power external. However, for the real application of an autonomous robot, it makes sense if the power is internal.

## 4.6 Actuation

During the experiments of the FARbot-s the solenoid and moving pin can get quite hot, around 60 °. At this temperature, the PLA starts to deform a little bit when the solenoid is on for a long period. One of the primary causes of solenoid overheating is a result of either a high applied current or an inadequate current rating for the solenoid. The increased current generates heat within the coil, leading to elevated temperatures that can adversely affect the solenoid's performance and lifespan. This is very likely since the rated voltage is 12 volts and the FARbot-s requires 17 volts. Additionally, continuous operation without sufficient cooling or rest periods can contribute to solenoid overheating. Furthermore, operating a solenoid beyond its recommended duty cycle can also result in overheating due to insufficient rest periods for heat dissipation. This is also likely to be a cause of overheating since the solenoid is operated at a range between 16 and 25 Hz, sometimes for more than a minute.

In future designs, it is recommended to incorporate a solution such as a heat sink or select a better-suited solenoid which is rated for higher currents. However, careful consideration must be given to the added mass of these solutions to ensure it does not negatively impact the overall performance and manoeuvrability of the robot. Striking the right balance between effective cooling and minimal additional mass would be crucial in ensuring the reliability and longevity of the solenoid's operation without compromising the robot's performance.

## 5 Conclusion

In this paper, a design process and physical model of the FARbot-s are presented. The physical model successfully performs the set tasks of forward locomotion and steering. Therefore, it can be concluded that the physical model is successful in achieving the intended objectives, which are, achieving forward locomotion and steering function while using only a single actuator.

Methods to increase performance in future research by achieving better heat dissipation and installing all

electronics internal are discussed. Furthermore, a possible explanation for the mirrored steering direction is discussed and tested with experiments. Additionally, an experiment to validate this hypothesis in future research is proposed.

The FARbot-s stands out as the only small walking robot with a steering mechanism that utilises only one actuator, according to the authors' knowledge. This design choice offers several advantages compared to using multiple actuators, including ease of assembly, simplified control, and reduced cost.

The successful realisation of a walking robot with steering functionality and a single actuator is made possible by leveraging resonance frequencies. The results clearly demonstrate an increase in velocity when the robot operates near its resonance frequency. The forward locomotion and steering mechanism, designed using resonance, is further validated through a series of experiments that demonstrate the mechanism is working.

## References

- [1] Andrew T. Baisch et al. 'HAMR3: An autonomous 1.7g ambulatory robot'. In: *2011 IEEE/RSJ International Conference on Intelligent Robots and Systems*. IEEE, Sept. 2011, pp. 5073–5079. ISBN: 978-1-61284-456-5. DOI: 10 . 1109 / IROS . 2011 . 6095063.
- [2] Andrew T. Baisch et al. 'High speed locomotion for a quadrupedal microrobot'. In: *The International Journal of Robotics Research* 33.8 (July 2014), pp. 1063–1082. ISSN: 0278-3649. DOI: 10 . 1177 / 0278364914521473.
- [3] P. Birkmeyer, K. Peterson and R. S. Fearing. 'DASH: A dynamic 16g hexapedal robot'. In: *2009 IEEE/RSJ International Conference on Intelligent Robots and Systems*. IEEE, Oct. 2009, pp. 2683–2689. ISBN: 978-1-4244-3803-7. DOI: 10 . 1109/IROS . 2009 . 5354561.
- [4] Jonathan E Clark et al. *iSprawl: Design and Tuning for High-speed Autonomous Open-loop Running*. *iSprawl: Design and Tuning for High-Speed Autonomous Open-Loop Running*. Tech. rep. 2006. URL: <https://www.researchgate.net/publication/220121764>.
- [5] Design Simulation. *Working Model 2D*. 2004.
- [6] Simulink Documentation. *Simulation and Model-Based Design*. 2022.
- [7] Robert J. Full and Michael S. Tu. 'Mechanics of A Rapid Running Insect: Two-, Four-and Six-Legged Locomotion'. In: *Journal of Experimental Biology* 156.1 (Mar. 1991), pp. 215–231. ISSN: 0022-0949. DOI: 10.1242/jeb.156.1.215.
- [8] Duncan W. Haldane et al. 'Animal-inspired design and aerodynamic stabilization of a hexapedal millirobot'. In: *Proceedings - IEEE International Conference on Robotics and Automation*. 2013, pp. 3279–3286. ISBN: 9781467356411. DOI: 10 . 1109/ICRA.2013.6631034.
- [9] A.M. Hoover, E. Steltz and R.S. Fearing. 'RoACH: An autonomous 2.4g crawling hexapod robot'. In: *2008 IEEE/RSJ International Conference on Intelligent Robots and Systems*. IEEE, Sept. 2008, pp. 26–33. ISBN: 978-1-4244-2057-5. DOI: 10.1109/IROS.2008.4651149.
- [10] Aaron M. Hoover et al. 'Bio-inspired design and dynamic maneuverability of a minimally actuated six-legged robot'. In: *2010 3rd IEEE RAS and EMBS International Conference on Biomedical Robotics and Biomechanics, BioRob 2010*. 2010, pp. 869–876. ISBN: 9781424477081. DOI: 10.1109/BIOROB.2010.5626034.
- [11] Larry L. Howell, Spencer P. Magleby and Brian M. (Brian Mark) Olsen. *Handbook of compliant mechanisms*. ISBN: 9781119953456.
- [12] Kinovea. *Kinovea*. 2016.
- [13] Nicholas J. Kohut et al. 'MEDIC: A legged millirobot utilizing novel obstacle traversal'. In: *Proceedings - IEEE International Conference on Robotics and Automation*. 2011, pp. 802–808. ISBN: 9781612843865. DOI: 10 . 1109 / ICRA . 2011 . 5980360.
- [14] Kohut N. J. et al. 'Aerodynamic Steering of a 10 cm High-Speed Running Robot'. In: (2013). URL: <https://ieeexplore.ieee.org/document/6697167>.
- [15] Jeremy M. Morrey et al. 'Highly Mobile and Robust Small Quadruped Robots'. In: *IEEE International Conference on Intelligent Robots and Systems*. Vol. 1. 2003, pp. 82–87. DOI: 10.1109/iros.2003.1250609.
- [16] Gennaro Notomista et al. 'A Study of a Class of Vibration-Driven Robots: Modeling, Analysis, Control and Design of the Brushbot'. In: (Feb. 2019). URL: <http://arxiv.org/abs/1902.10830>.
- [17] A. O. Pullin et al. 'Dynamic turning of 13 cm robot comparing tail and differential drive'. In: *Proceedings - IEEE International Conference on Robotics and Automation*. Institute of Electrical and Electronics Engineers Inc., 2012, pp. 5086–5093. ISBN: 9781467314039. DOI: 10 . 1109 / ICRA . 2012 . 6225261.
- [18] Shannon A. Rios, Andrew J. Fleming and Yuen Kuan Yong. 'Miniature Resonant Ambulatory Robot'. In: *IEEE Robotics and Automation Letters* 2.1 (Jan. 2017), pp. 337–343. ISSN: 2377-3766. DOI: 10.1109/LRA.2016.2614837.

- [19] J K Schonebaum. *Challenge the future Department of Precision and Microsystems Engineering The design of a monolithic, compliant, resonant running robot at insect scale*. Tech. rep. 2019.
- [20] P S Sreetharan et al. ‘Monolithic fabrication of millimeter-scale machines’. In: *Journal of Micromechanics and Microengineering* 22.5 (May 2012), p. 055027. ISSN: 0960-1317. DOI: 10.1088/0960-1317/22/5/055027.
- [21] Panagiotis Vartholomeos and Evangelos Papadopoulos. *Analysis, Design and Control of a Planar Micro-robot Driven by Two Centripetal-Force Actuators \**. Tech. rep.
- [22] Panagiotis Vartholomeos and Evangelos Papadopoulos. ‘Dynamics, design and simulation of a novel microrobotic platform employing vibration microactuators’. In: *Journal of Dynamic Systems, Measurement and Control, Transactions of the ASME* 128.1 (Mar. 2006), pp. 122–133. ISSN: 00220434. DOI: 10.1115/1.2168472.
- [23] R.J. Wood, E. Steltz and R.S. Fearing. ‘Optimal energy density piezoelectric bending actuators’. In: *Sensors and Actuators A: Physical* 119.2 (Apr. 2005), pp. 476–488. ISSN: 09244247. DOI: 10.1016/j.sna.2004.10.024.



# 4

## Conclusion

The literature study presented in Chapter 2 provides great insight into existing and non-existing steering mechanisms. The overview shown in this chapter discusses the advantages and limitations of these mechanisms. One aspect that stands out for this project is the number of actuators, as more actuators will increase control complexity and energy consumption. This leads to the project goal: designing a forward locomotion and steering mechanism for a small compliant resonant walking robot without the addition of extra actuators.

In the research paper presented in Chapter 3, the work conducted to achieve this goal is outlined. The results of the research paper showcase a functioning robot that can not only change its trajectory by adjusting the input frequency but is also capable of making fast wide turns and slow sharp turns. The robot achieves this manoeuvrability without needing more than one actuator.



# A

## Simulink and generalised stiffness

The Simulink model can be seen in Figure A.1. A legend of all the blocks used in the model can be seen in Figure A.2. The code used to calculate the generalised stiffness matrix can be found in Figure A.3.

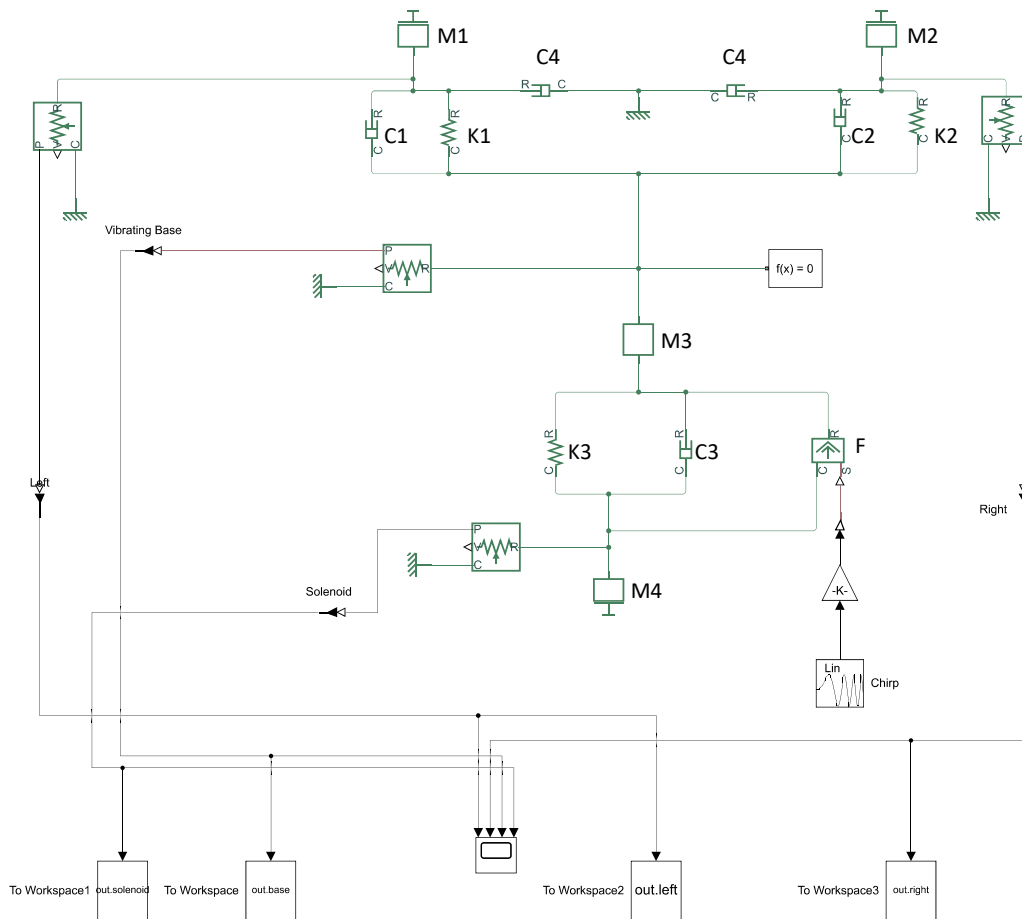


**Figure A.1:** Simulink model of the simplified dynamical model.

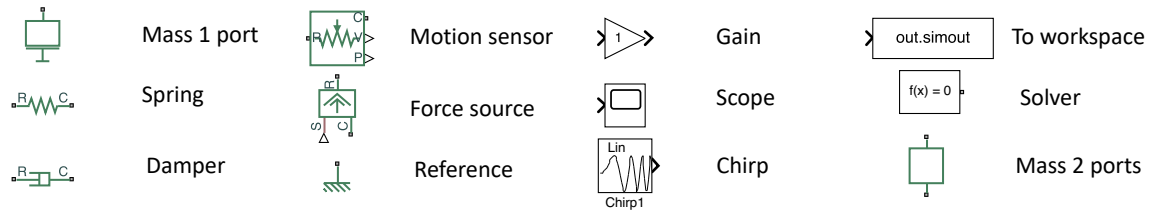


Figure A.2: Legend of Simulink blocks used in the Simulink model.

01/07/23 9:38 AM .../Model\_doublefrequency\_leftonly\_v1.m 1 of 1

```
clear all
close all
clc

syms q1 q2 dq1 dq2 dddq1 dddq2

q = [q1 q2] ;
dq = [dq1 dq2] ;
ddq = [dddq1 dddq2] ;

%% Initializing
% Getting Parameters
Parameters

%% Mapping
X=[X_com1+q(1),Y_com1 ,X_com1+q(2),Y_com1]';
dX=jacobian(X,q)*dq.';
Phi = asin(q(1)/(L_intermediate+2*L_flexure/2));
Phi2 = asin(q(2)/(L_intermediate+2*L_flexure/2));
%% Energy
M =diag([Mtot1,Mtot1,Mtot1,Mtot1]);
T = (1/2)*dX.'*M*dX;
V = (1/2)*4*k1*Phi^2+(1/2)*4*k2*Phi2^2;

%% Equations of motion
dT = jacobian(T, q).';
dV = jacobian(V, q).';
dTq = jacobian(T, dq).';
ddT = jacobian(dTq, dq)*ddq.' + jacobian(dTq, q)*dq.';

EoM = ddT - dT + dV;

%% Matrices %%
K_syms = jacobian(EoM, q);
K = double(subs(K_syms,[q],[0 0]));

M_syms = jacobian(EoM,ddq);
M = double(subs(M_syms));

%% Eigenvectors & Eigenmodes
[eigvec, omega_sq] = eig(M\K);
omega_sq(omega_sq<1E-10) = 0;
EigenFreqs_unsorted_rads = omega_sq.^(0.5)*ones(1,1);
EigenFreqs_unsorted = EigenFreqs_unsorted_rads/(2*pi);
[EigenFreqs, ind] = sort(EigenFreqs_unsorted)
```

Figure A.3: Code to calculated generalised stiffness

# B

## Friction and voltage experiments

The FARbot-s needs to walk on a surface, so friction is going to be an important factor. Many types of walking robots walk by exploiting friction[2]. To find the influence of friction on the eigenmodes of the FARbot-s design an experiment is constructed. The purpose of the experiment is to give insight into the influence of friction on the system, but more importantly, if friction can be modelled as damping in the Simulink model. Additionally, the experiment gives insight if the input voltage that can be modelled as gain in the Simulink model. The chapter is structured as follows: section B.1 contains the methodology, section B.2 contains the results, B.3 contains the discussion, and section B.4 contains the conclusion.

### B.1. Methodology

The experimental setup is designed for two experiments. The first experiment aims to test the relationship between applied friction on the test model and the damping coefficient in the Simulink model. The second experiment focuses on testing the relationship between the input voltage on the test model and the gain in the Simulink model. During the experiment, a chirp signal is used as the input for the solenoid, and the displacement of the stages is measured.

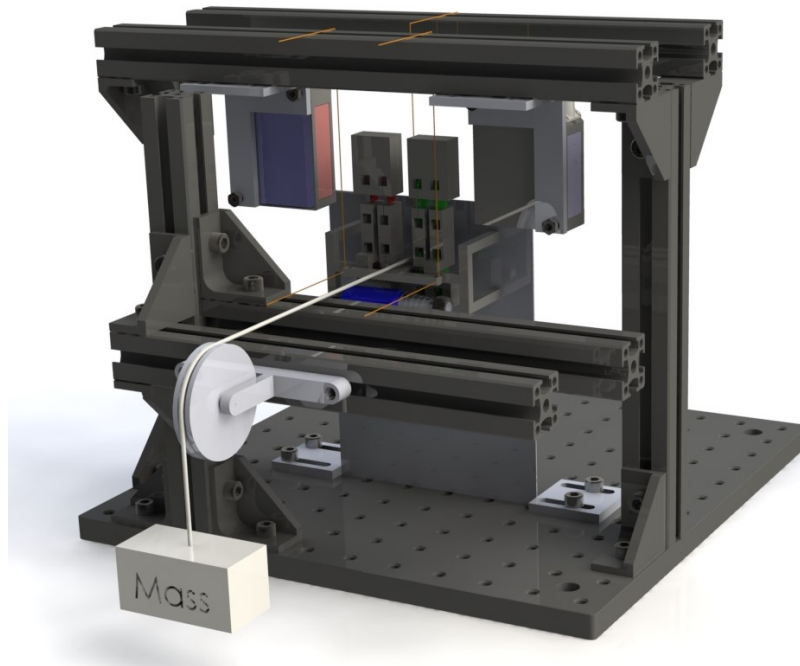


**Figure B.1:** CAD model of the experimental setup to test the influence of friction and input voltage.

For the first experiment, to apply friction, a surface is placed against the feet of the test model, and a mass is attached to it. The mass is connected by a wire and routed with a pulley to minimise additional friction. Since the surface is perpendicular to the test model, the mass directly applies a normal force on the test model and normal force times the friction coefficient equals friction force. The friction experiment consists of six tests where the attached mass is increased by five grams starting from zero. So, the first test will show if the Simulink model matches the results of the test setup. In the Simulink model, a chirp signal is also applied to the input force, along with a parameter sweep involving several friction coefficients, also starting from zero. The results of the test setup closely match those of the Simulink model.

For the second experiment, the attached mass is kept at 25 grams, while the voltage input is increased by one volt for each test, starting from 7 volts. Therefore, the last test of the friction experiment serves as the first test of the voltage experiment. Once again, in the Simulink model, a chirp signal is applied to the input force, along with a parameter sweep involving several gain multipliers. The results of the test setup are consistent with the results obtained from the Simulink model.

Lastly, an additional experiment is conducted to determine a damping coefficient that matches that of the final FARbot-s design.

The CAD model of the experimental setup can be seen in Figure B.1. During the experiments the test model of the FARbot-s has to be constrained in 5 degrees of freedom (DoF) and a permissible translation in the same direction of the movement of the solenoid moving mass. The Freedom and Constraint Topology (FACT) method by J. B. Hopkins[3] is used. The constrain type can be seen in Figure B.2.

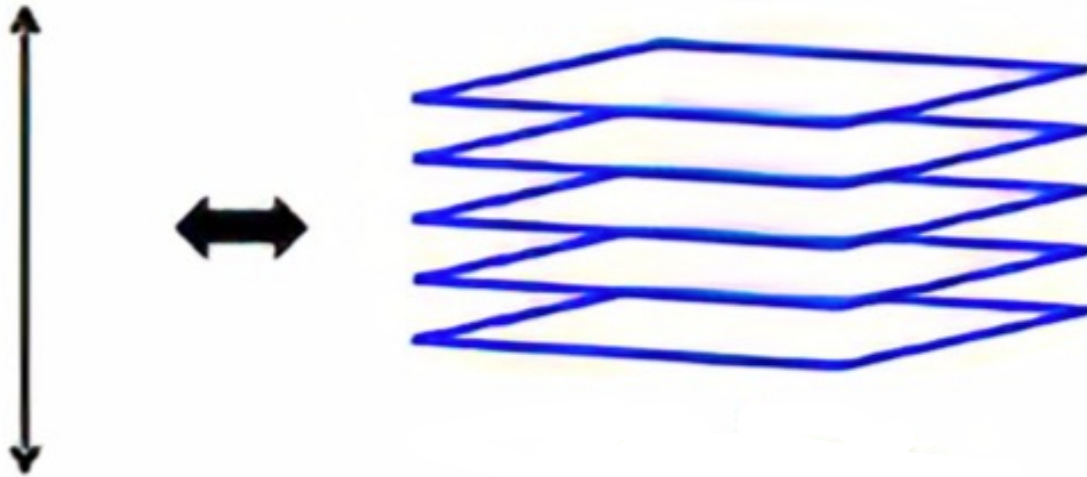


**Figure B.2:** Freedom and constrain topology (FACT). Any line that lies within any plane that belongs to a set of parallel A-planes is a constraint line. A single permissible translation in a direction that is normal to the parallel planes of constraint lines [3], [4].

## B.2. Results

The experimental setup can be seen in Figure B.3. The results of the friction experiments in Figure B.5, the results of the voltage experiments in Figure B.6 and the results of additional experiment in Figure B.7.

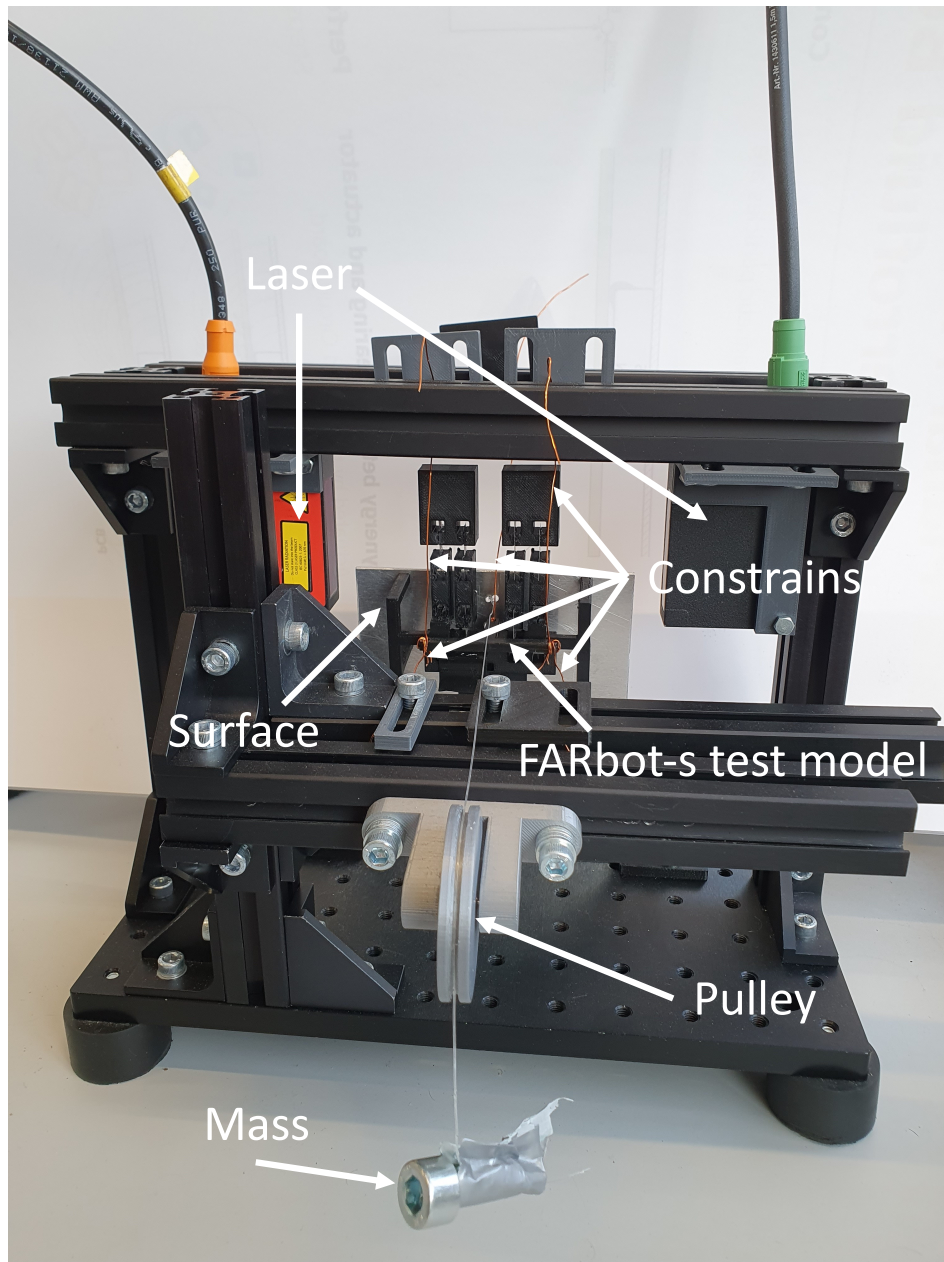
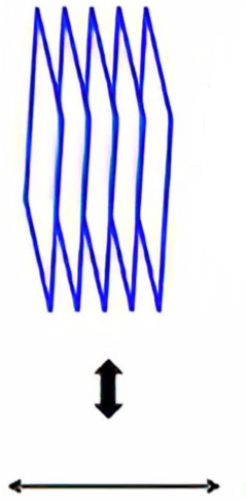


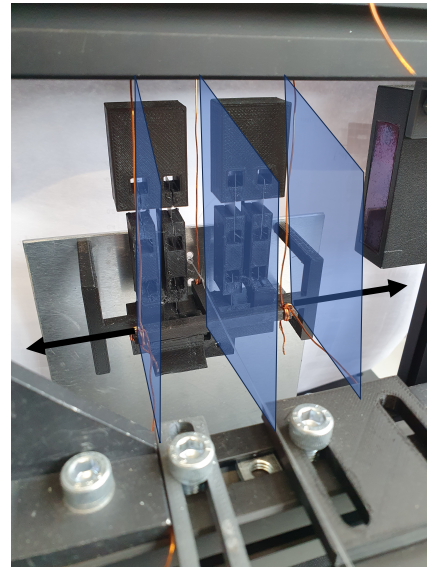
**Figure B.3:** The FARbot-s test model is attached to the test setup with constrain wires. The constrain wires are designed with the FACT method, see Figure B.4. The aluminium surface is perpendicular to the feet and friction is applied via a wire holding a mass. To prevent friction on the wire the wire is routed via a pulley. The two optoNCDT ILD1302-20 lasers are used to measure the position of the stages.

The implementation of the FACT method into the setup can be seen in Figure B.4. Five DoF have to be constrained so, only five wires can be used to prevent the model from being overconstrained.

The Simulink and laser data output are both in the time domain. With a Fast Fourier transform (FFT) the output data is transformed to a frequency domain. The output of the test has a lot of noise, so in order to make the data more clear it is fitted with a moving average filter. The k-point value of the moving average filter is 100.



(a) Five DoF constrained, only DoF permissible is translation perpendicular to the parallel planes[4].



(b) Three parallel planes constraining the FARbot-s test model. The left plane contains two wires (horizontal and vertical), the middle plane contains one wire (vertical), and the right plane contains two wires (horizontal and vertical).

**Figure B.4:** a) shows the theoretical FACT constrain type and b) shows the implementation of the constrain type in the test setup.

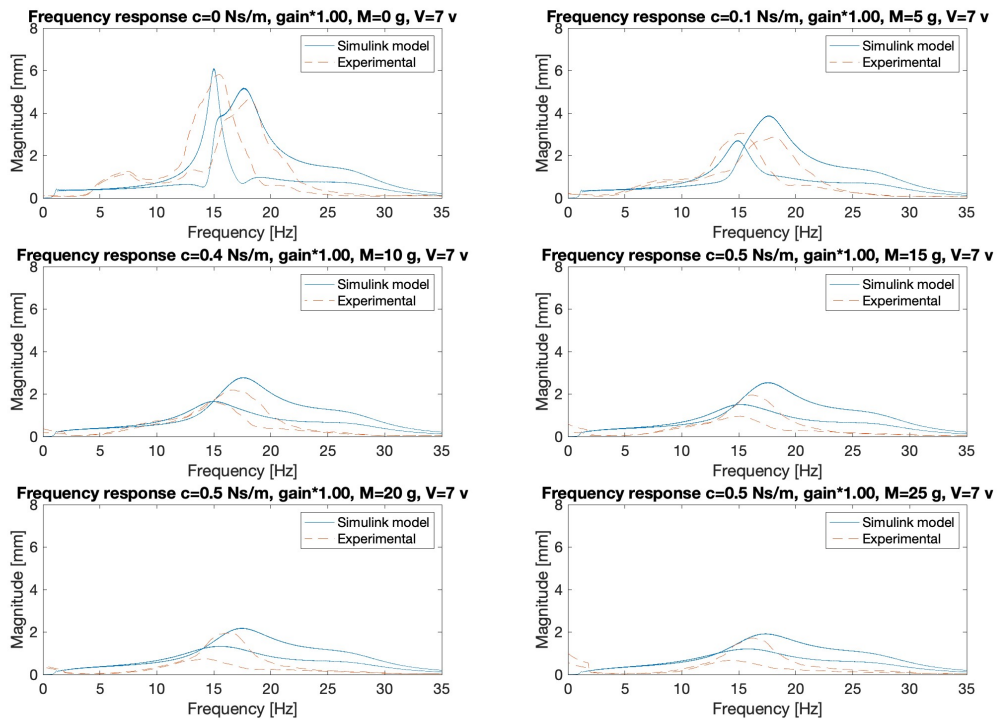


**Figure B.5:** Results friction experiment. From top left to bottom right five gram is added to the additional mass. The blue solid line shows the Simulink results, the orange striped line shows the experimental results.

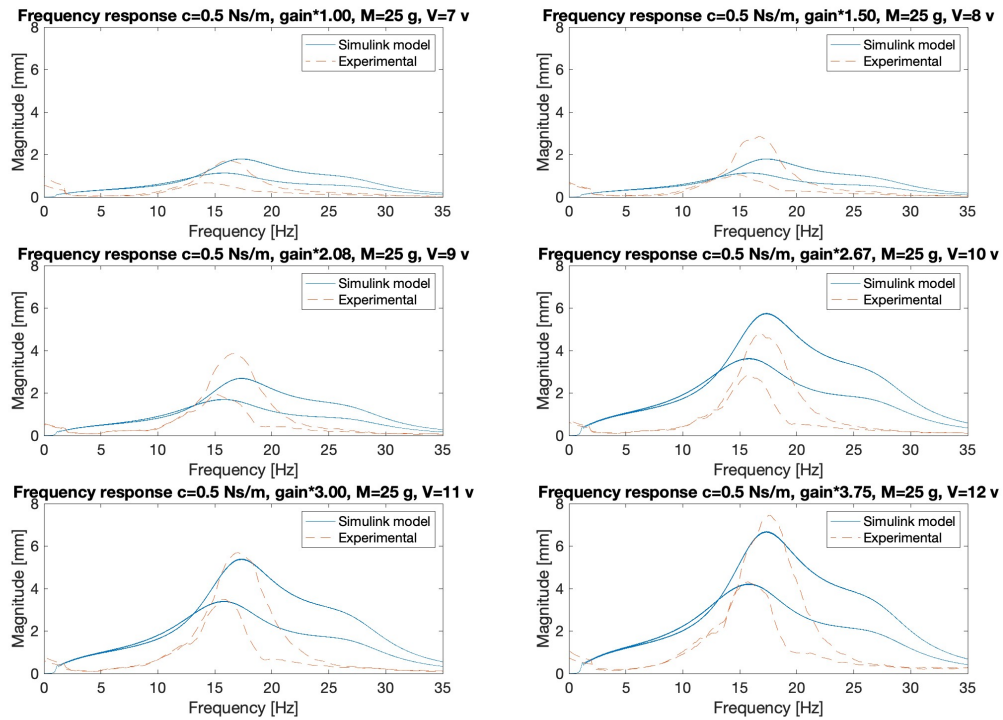


**Figure B.6:** Results voltage experiment. From top left to bottom right 1 volt is added to the input voltage. The blue solid line shows the Simulink results, the orange striped line shows the experimental results.

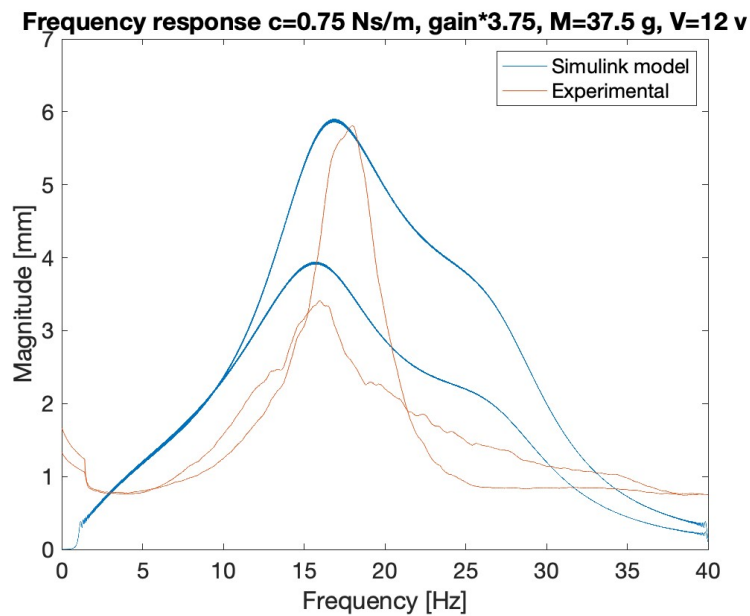


**Figure B.7:** Result of the additional experiment. For the test setup, an additional mass of 37.5 g was added and a twelve-volt input voltage. For the Simulink model damping coefficient is  $0.75$  Nsm<sup>-1</sup> and gain multiplied by 3.75.

### B.3. Discussion

The results of the top left plot in Figure B.5 exhibit a significant overlap between the experimental tests and the Simulink output. The peaks occur at the same frequency; however, the first peak appears wider, suggesting a broader range of frequencies contributing to the response. Additionally, there is a slight magnitude amplification around seven Hz, indicating a resonance effect. This can be attributed to the eigenfrequency of the constraint system, which acts like a swinging motion. Furthermore, the increase in damping exhibits similar behaviour to the increase in friction, although the damping does not increase linearly.

This nonlinearity may be a result of damping being velocity-dependent, while friction is not. Another factor could be that the static friction forces are higher than the dynamic friction force. This can be observed at the beginning of the plots, where the magnitude remains zero for a longer duration as the friction increases. Further investigation into the relationship between friction and damping could provide insights into the system's dynamic behaviour.

The second experiment also demonstrates a similar trend to the Simulink model. As shown in Figure B.6, the resonance peak remains in the same location, but the amplitude increases as the voltage and gain increase, indicating a stronger response. The increase in gain exhibits a linear relationship, which implies a proportional amplification of the input signal. However, it is worth noting that at higher gain levels, there may be a point of diminishing returns or potential instability that should be investigated.

In the additional experiment, it is observed that for a mass of 37.5 grams and an input voltage of 12 volts, the Simulink model produces similar results with a damping coefficient of  $0.75 \text{ Nsm}^{-1}$  and a gain multiplication of 3.75. These findings suggest that the chosen parameters effectively replicate the desired system response. However, further validation and optimisation of these parameters should be conducted to ensure robust performance across a wider range of operating conditions and to account for potential variations in the system's behaviour.

### B.4. Conclusion

In conclusion, the experimental setup consists of two distinct experiments aimed to investigate the relationships between applied friction, damping coefficient, input voltage, and gain in the Simulink model of the test system. The results demonstrate a remarkable overlap between the experimental tests and the Simulink output, indicating a good agreement between the physical system and the model.

The first experiment focuses on the relation between applied friction and the damping coefficient. It is observed that the peaks in the frequency response of the experimental and Simulink data aligned, although with a slight difference in peak width. A small magnitude amplification of around seven Hz is attributed to the eigenfrequency of the constrained system. Furthermore, the increase in damping shows a similar trend to the increase in friction, suggesting a correlation between these two factors. However, it is noted that the relationship between damping and friction was nonlinear, possibly due to the velocity-dependent nature of damping and the disparity between static and dynamic friction forces.

The second experiment investigates the relation between input voltage and gain. The resonance peak in the frequency response remains consistent across different voltage levels, indicating the robustness of the system. Moreover, the amplitude of the response increases proportionally with both the input voltage and gain, supporting the linear relationship between these parameters.

The additional experiment aims to identify a damping coefficient that matches the desired performance of the FARbot-s design. By comparing the experimental and Simulink results for specific mass and voltage values, a damping coefficient of  $0.75 \text{ Nsm}^{-1}$  and a gain multiplication of 3.75 is found to yield similar outcomes. These findings suggest the suitability of these parameter values for optimising the FARbot-s system.

Overall, this study provides valuable insights into the relationships between friction, damping, input voltage, and gain in the test system. The experimental results aligns closely with the Simulink model, affirming its accuracy and reliability. Further research can build upon these findings to refine the system's performance and explore potential applications in various domains, such as robotics and control systems.

# C

## Parameter optimisation

In order to find good parameters for the FARbot-s design an iterative parameter optimisation is conducted. The Simulink model in Appendix A is used and the output is optimised. To find how each parameter influences the eigenfrequencies of the masses, a parameter sweep is carried out. The results of the parameter sweep are shown below in Figure C.1, C.2, C.3, C.4, C.5 and C.6. During the parameter sweep only one parameter is changed the other stays the same, except for Figure C.6. The parameters can be found in Table C.1.

**Table C.1:** Parameters of the parameter sweep. The underlined block names are the varied parameters and can be found in the figures.

Block name	<u>M1</u>	<u>M2</u>	<u>M3</u>	<u>K1</u>	<u>K2</u>	<u>K3</u>	C1	C2	<u>C4</u>
Unit	g	g	g	N/m	N/m	N/m	Ns/m	Ns/m	Ns/m
Value	7.7	13.1	10.2	60	170	130	0.05	0.05	0.75

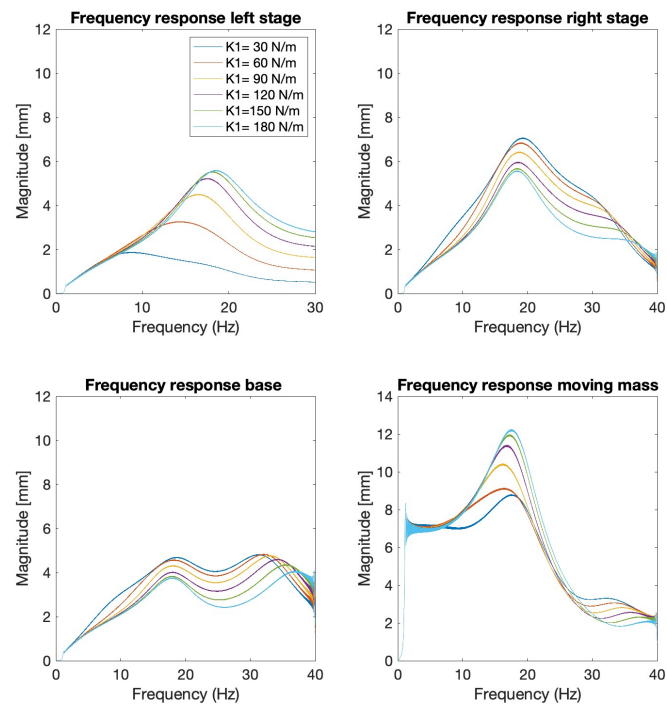


**Figure C.1:** Parameter sweep of spring K1.

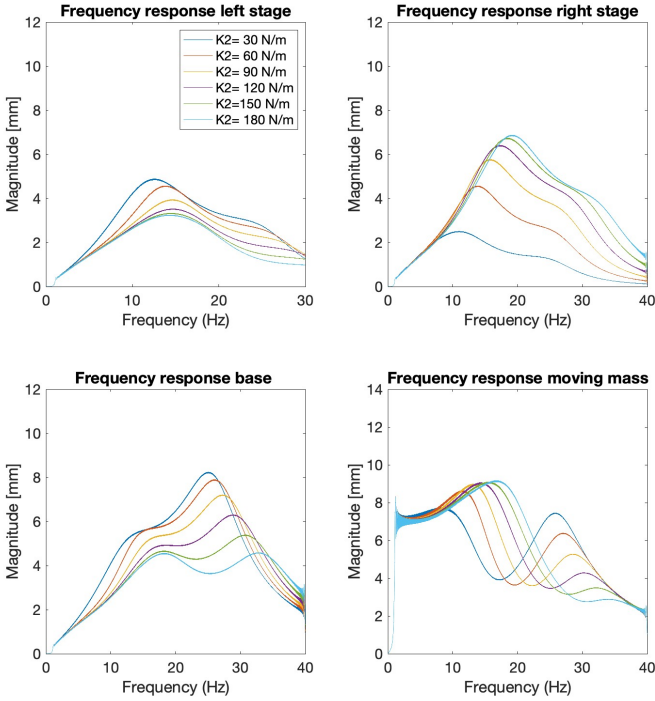


Figure C.2: Parameter sweep of spring  $K_2$ .

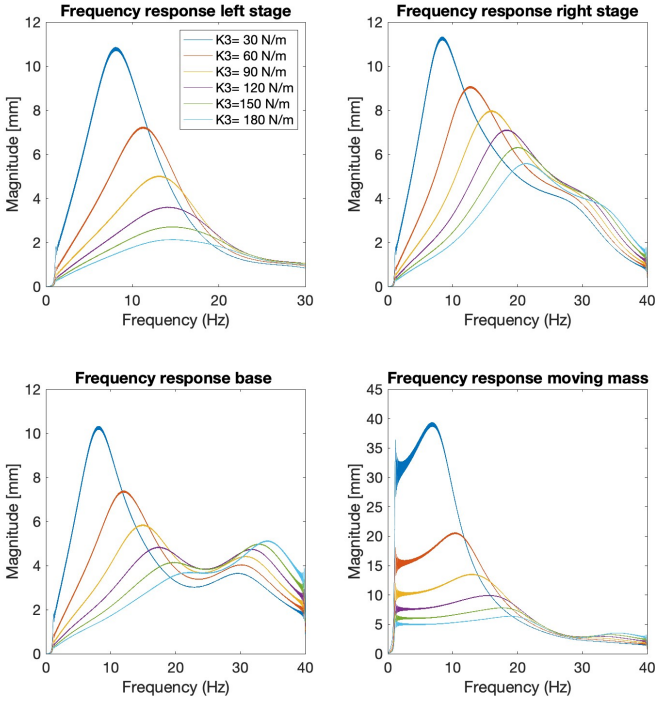


Figure C.3: Parameter sweep of spring  $K_3$ .

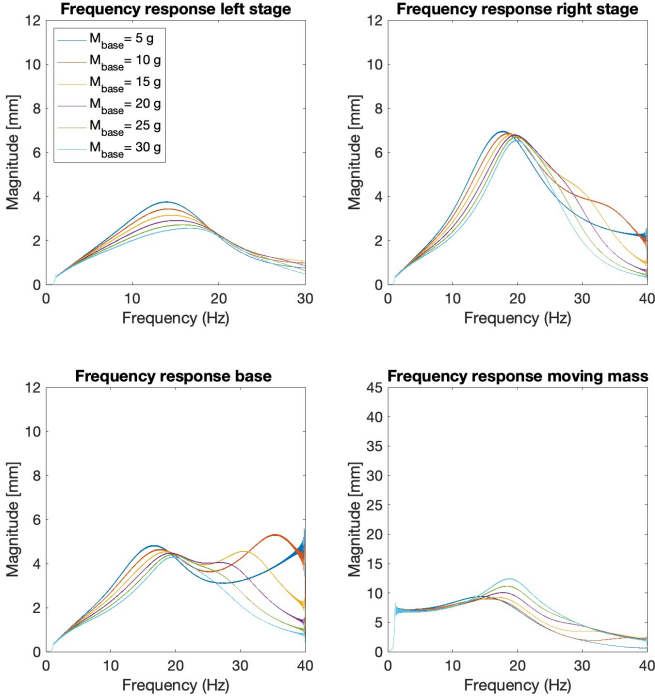


Figure C.4: Parameter sweep of mass M2.

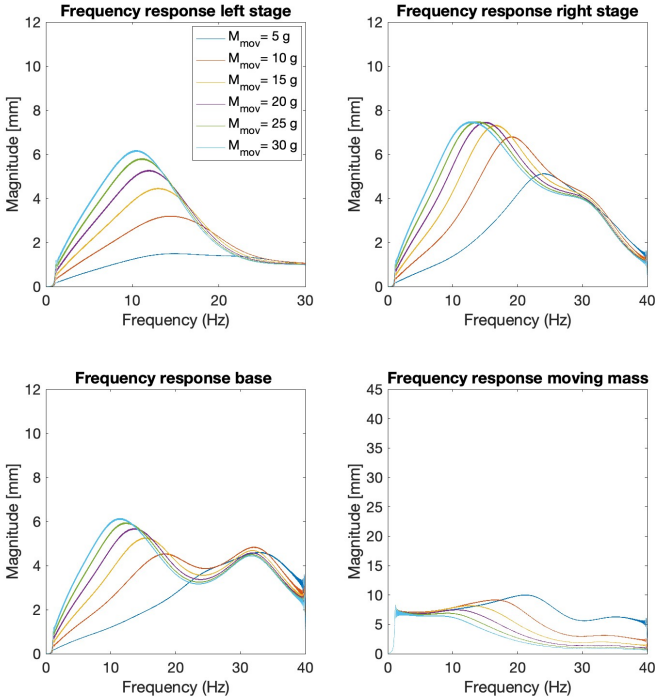


Figure C.5: Parameter sweep of mass M3.

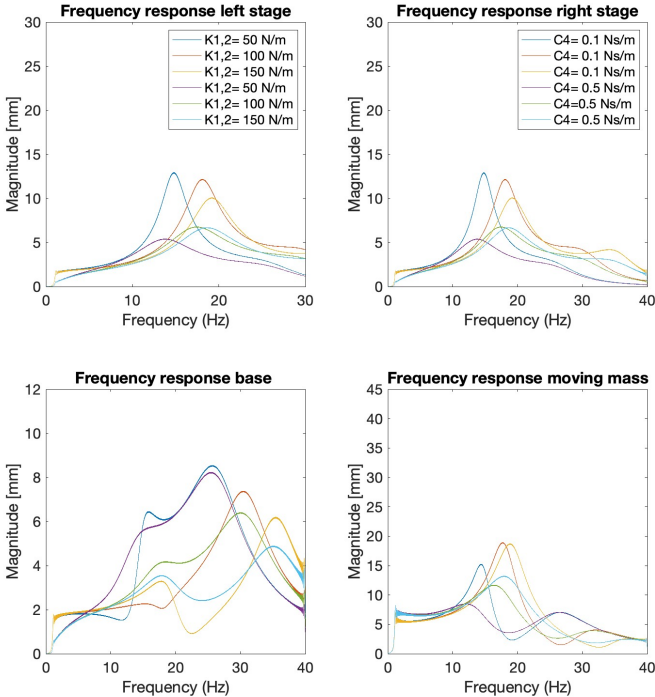
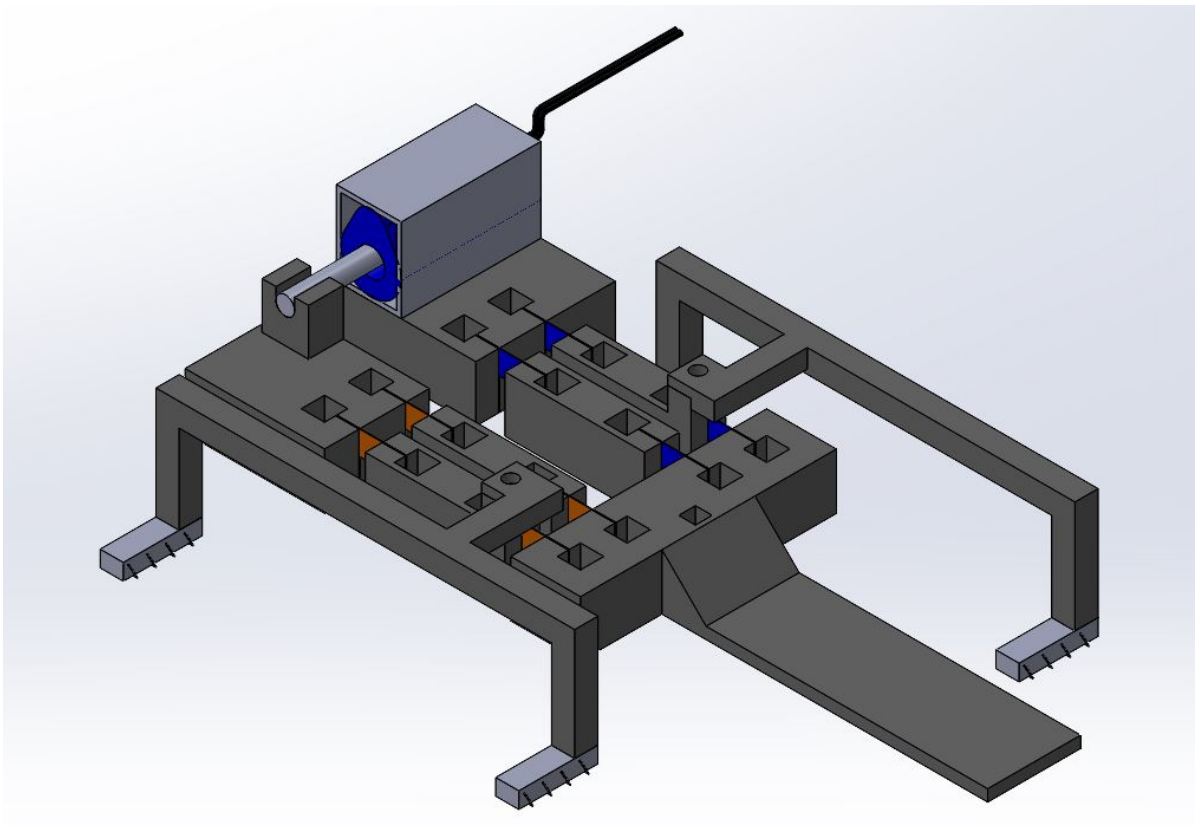


Figure C.6: Parameter sweep of spring  $K_1$  and  $K_2$  and damping coefficient  $C_4$ .

# D

## Other designs

Two alternative kinematic CAD designs are presented. The designs are fabricated as prototypes and tested but do not work in the intended way. The alternative design in Figure D.1 has the solenoid at a different position, the stages at the same side and asymmetric friction feet as a method to propel itself forward. The alternative design in Figure D.2 has the solenoid at the same position as the final design however, it has the stages on the same side and one-way bearings to propel itself forward.



**Figure D.1:** This alternative design has the stages on the same side of the base. The solenoid is mounted on one of the stages, and the moving pin is mounted on the other. This actuation method did not work because the eigenfrequency of the stages was always the same, and it was not possible to distinguish between the two stages. After testing with a Simulink model designed for this kinematic design, it is revealed that the eigenfrequency of the stages is the same. The forward locomotion mechanism of this design is based on creating more friction at the feet in the backward direction than in the forward direction. With this mechanism, the robot is able to propel itself forward, but the mechanism is sensitive to fabrication imperfections.

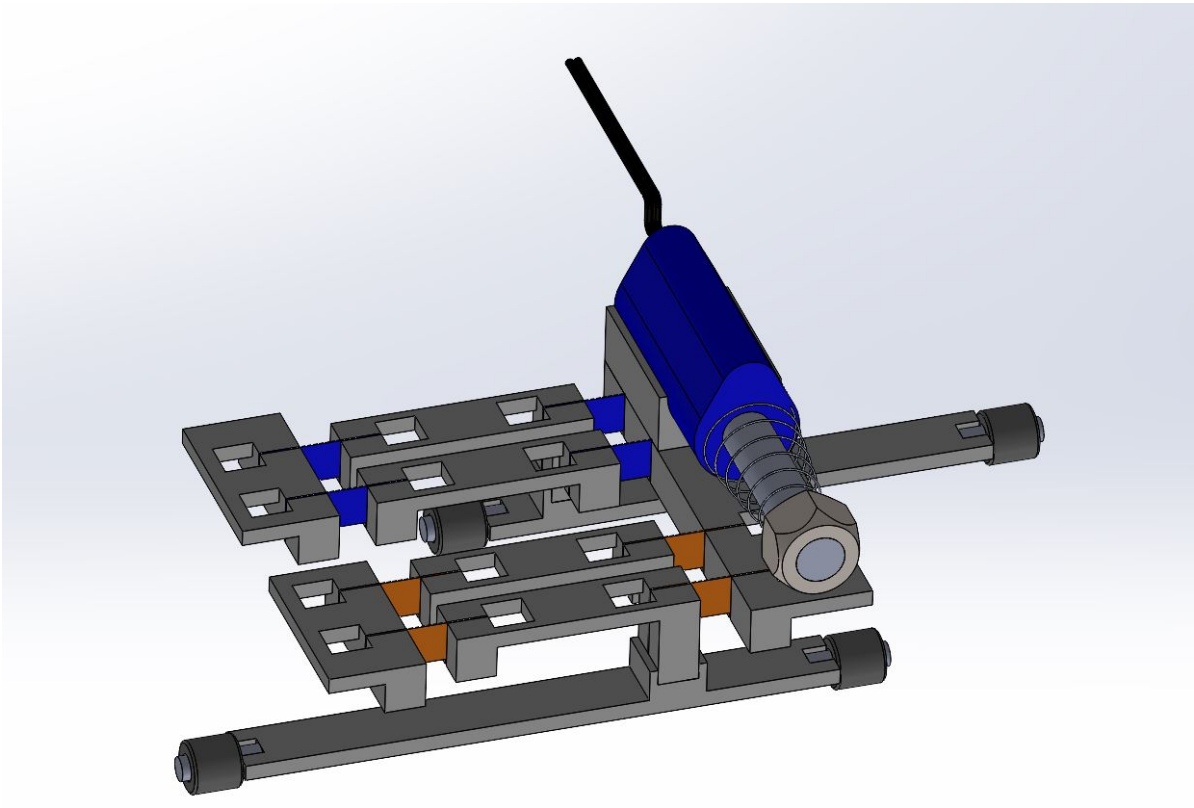


**Figure D.2:** This alternative design is more similar to the actual FARbot-s design compared to the model in Figure D.1. The position of actuation is the same, on the base. However, the stages are on the same side, which makes it difficult to balance the centre of gravity and distribute the normal force evenly on all four feet. The forward locomotion mechanism in this design uses one-way bearings as feet. These bearings are capable of rotating in one direction, but not in the other. The prototype is unable to propel itself forward using this method because a required pre-stress on the bearing was necessary, and the mass of the model is not sufficient to achieve this. Increasing the model's weight is not an option as it has a significant impact on the eigenfrequencies.

# E

## Steering analysis

For the steering analysis conducted in the discussion of the research paper a moment plot is made. In order to save space and not mention the same process twice the plots are left out of the research paper. However, to make the report complete the plots are added in the appendix. The moment plot of 20 Hz can be seen in Figure E.1 and the moment plot of 25 Hz can be seen in Figure E.2

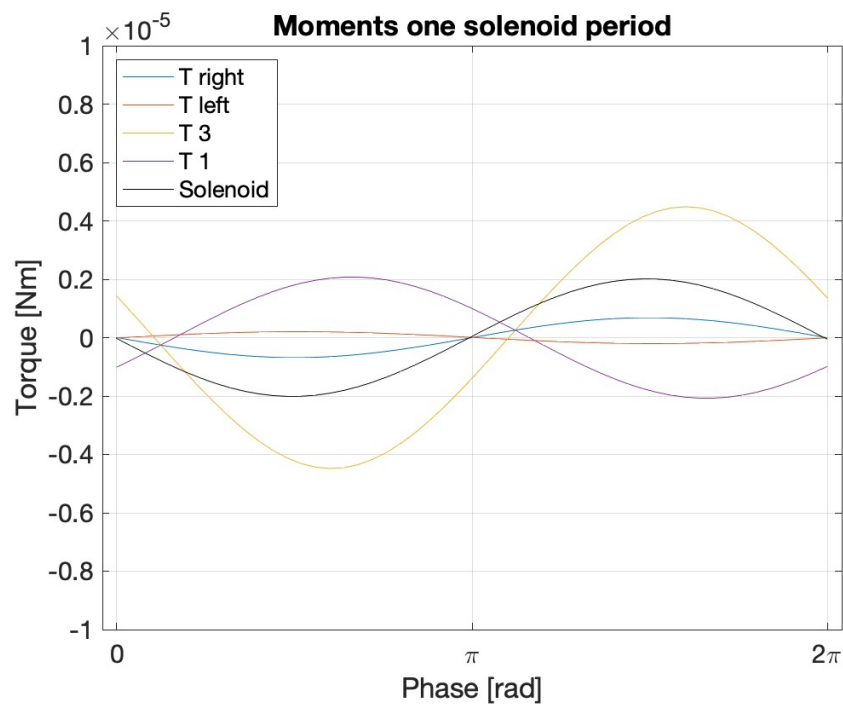


**Figure E.1:** The four moments generated by inertia of the feet and stages over one solenoid period. The input frequency of the solenoid is 20 Hz

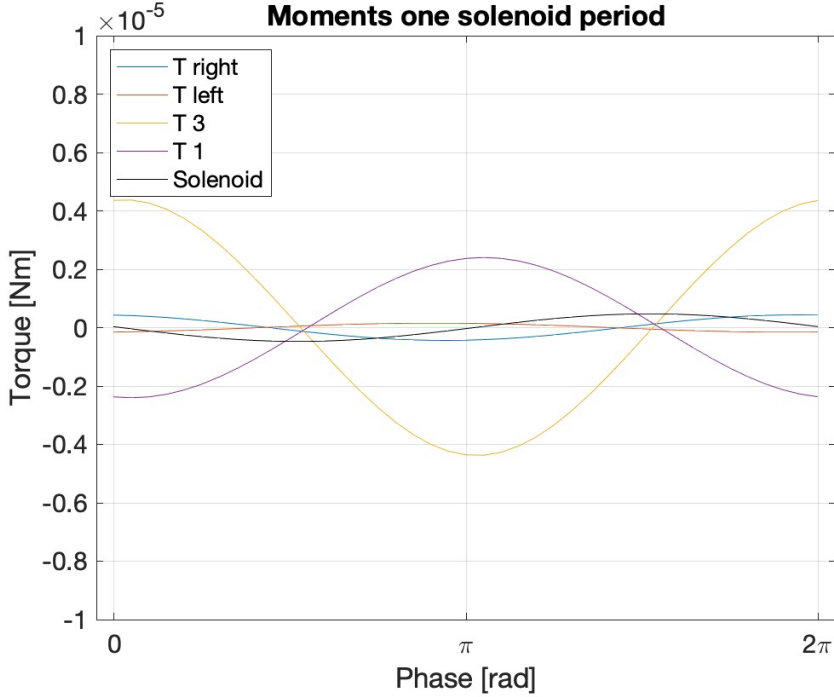


Figure E.2: The four moments generated by inertia of the feet and stages over one solenoid period. The input frequency of the solenoid is 25 Hz

# F

## Extra experimental results

Section F.1 contains two trajectory experiments. In one experiment the cable is fixed to the tripod. In the other experiment, the surface on which the FARbot-s is walking is concrete. Section F.2 contains the time response of the physical model with a chirp signal applied.

### F.1. Additional trajectory experiments

The experiments of the trajectory tracking presented in the research paper are conducted by holding the wire by hand. Before those tests, the experiment was conducted by fixating the wire to the tripod. In Figure F.1 the experiment results with the fixed wire can be seen. It is clear that the wire has a significant influence on the trajectory of the FARbot-s

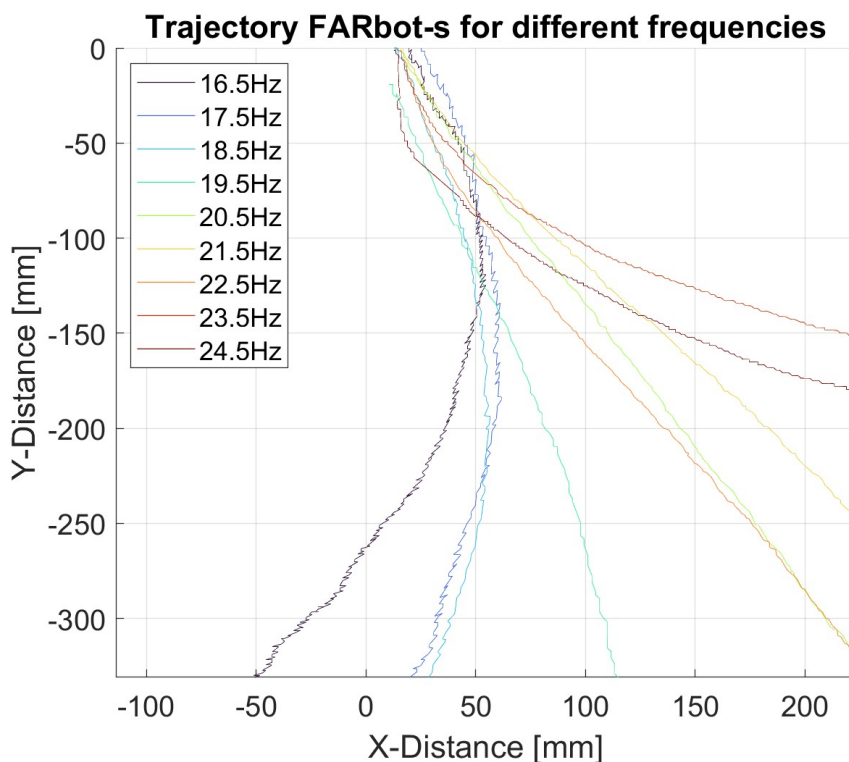


**Figure F.1:** Trajectory of FARbot-S on HPL for different solenoid input frequencies. The frequency ranges from 16.5 to 24.5 Hz in steps of 1 Hz

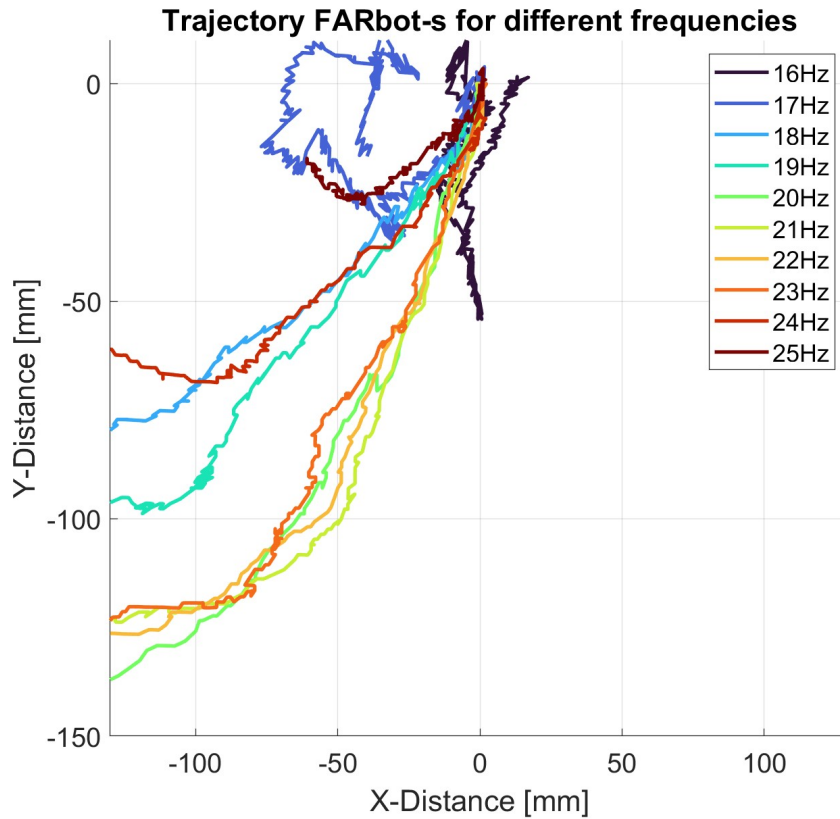


**Figure F.2:** Trajectory of FARbot-S on concrete for different solenoid input frequencies. The frequency ranges from 16 to 25 Hz in steps of 1 Hz

## F.2. Time response of physical model

Time response of the physical model of a chip signal up and chip signal down, from 1 to 25 Hz.

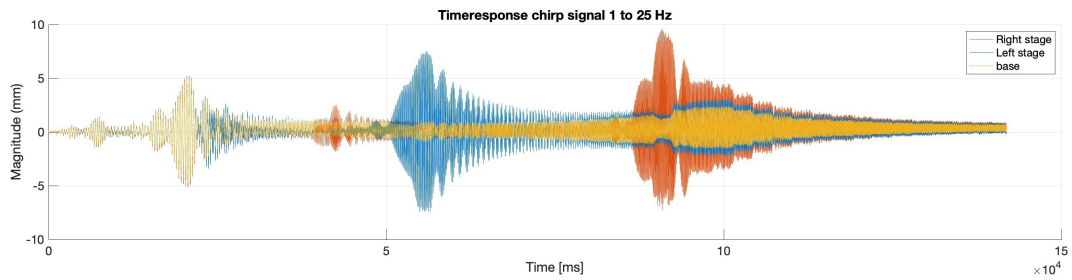


**Figure F.3:** Time response of the base and two stages for up chirp signal from 1 to 25 Hz.

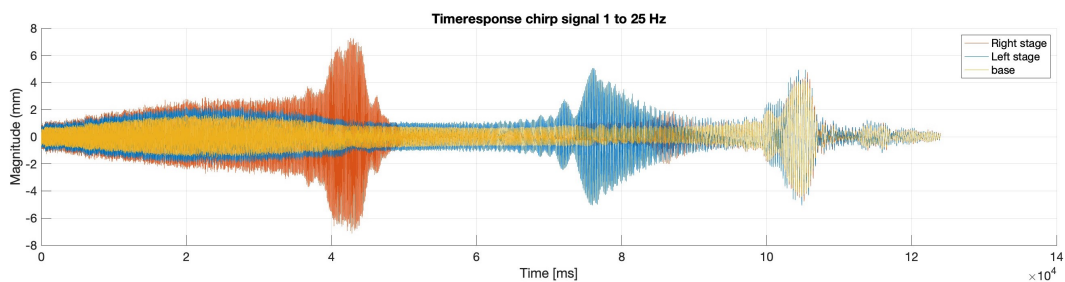
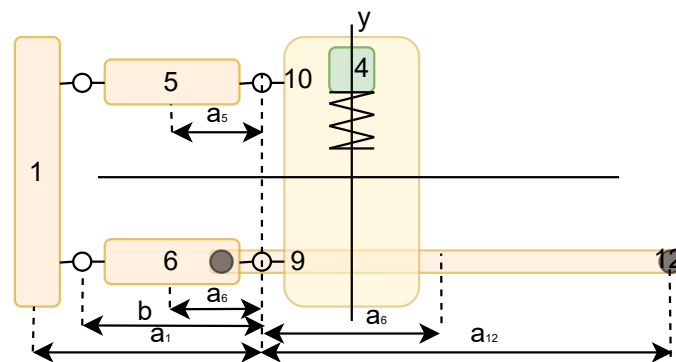


**Figure F.4:** Time response of the base and two stages for down chirp signal from 25 to 1 Hz.

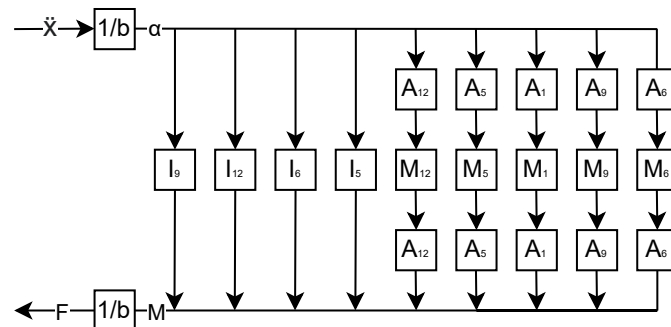
# G

## Equivalent mass calculation

In order for the Simulink model to represent the physical model the mass connected to each of the stages need to be on the same x coordinate. Since the Simulink model is only one-dimensional all masses need to be translated and their mass moment of inertia also needs to be taken into account. The parts and distance names of the left stage can be seen in Figure G.1a. The parts and distance names of the right stage can be seen in Figure G.2a. The equivalent mass can then be calculated with the flow carts where Figure G.1b corresponds with the left stage and Figure G.2b corresponds with the right stage. The equivalent mass is dependent on distance, mass and mass moment of inertia. The distance, mass and mass moment of inertia of all the parts can be found in Table G.1.

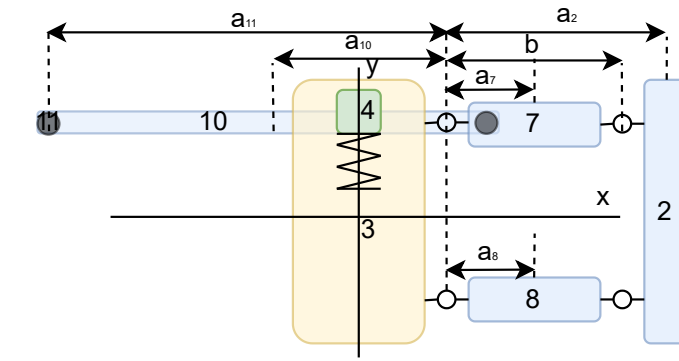


(a) Model to calculate the equivalent mass of the left stage.

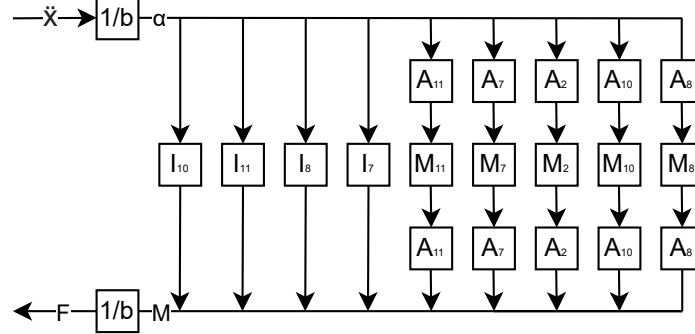


(b) Flow chart used to calculate the equivalent mass of the left stage.

**Figure G.1:** low chart and model to calculate the equivalent mass of right stage



(a) Model to calculate the equivalent mass of the right stage.



(b) Flow chart used to calculate the equivalent mass of the right stage.

**Figure G.2:** Flow chart and model to calculate equivalent mass of right stage

The equivalent mass of the left and right stage can be calculated with Equation G.1 and Equation G.2, respectively.

$$Meq_{left} = \frac{J_{12}}{b^2} + \frac{J_9}{b^2} + \frac{J_6}{b^2} + \frac{J_5}{b^2} + \frac{a_{12}^2}{b} M_{12} + \frac{a_1^2}{b} M_1 + \frac{a_6^2}{b} M_6 + \frac{a_5^2}{b} M_5 + \frac{a_9^2}{b} M_9 \quad (G.1)$$

$$Meq_{right} = \frac{J_{11}}{b^2} + \frac{J_{10}}{b^2} + \frac{J_7}{b^2} + \frac{J_8}{b^2} + \frac{a_{11}^2}{b} M_{11} + \frac{a_2^2}{b} M_2 + \frac{a_7^2}{b} M_7 + \frac{a_8^2}{b} M_8 + \frac{a_{10}^2}{b} M_{10} \quad (G.2)$$

**Table G.1:** Parameters to calculate equivalent mass

Parameter	Value	Unit	Description
b	35.0	mm	Distance from rotation point to mass location
a1	45.0	mm	Distance from CoG M1 to rotation point
a2	45.0	mm	Distance from CoG M2 to rotation point
a5	15.7	mm	Distance from CoG M5 to rotation point
a6	17.5	mm	Distance from CoG M6 to rotation point
a7	15.7	mm	Distance from CoG M7 to rotation point
a8	17.5	mm	Distance from CoG M8 to rotation point
a9	19	mm	Distance from CoG M9 to rotation point
10	24	mm	Distance from CoG M10 to rotation point
a11	65	mm	Distance from CoG M11 to rotation point
a12	55	mm	Distance from CoG M12 to rotation point
M1	2	g	Mass of part 1
M2	2	g	Mass of part 2
M5	0.7	g	Mass of part 5
M6	0.9	g	Mass of part 6
M7	0.9	g	Mass of part 7
M8	0.7	g	Mass of part 8
M9	2.2	g	Mass of part 9
M10	2.2	g	Mass of part 10
M11	2	g	Mass of part 11
M12	2	g	Mass of part 12
I5	310	$\text{gmm}^2$	Mass moment of inertia of part 5
I6	335	$\text{gmm}^2$	Mass moment of inertia of part 6
I7	335	$\text{gmm}^2$	Mass moment of inertia of part 7 on rotation point
I8	310	$\text{gmm}^2$	Mass moment of inertia of part 8 on rotation point
I9	1462	$\text{gmm}^2$	Mass moment of inertia of part 9 on rotation point
I10	2233	$\text{gmm}^2$	Mass moment of inertia of part 10 on rotation point
I11	8028	$\text{gmm}^2$	Mass moment of inertia of part 11 on rotation point
I12	5748	$\text{gmm}^2$	Mass moment of inertia of part 12 on rotation point

# Bibliography

- [1] J. K. Schonebaum, “Challenge the future Department of Precision and Microsystems Engineering The design of a monolithic, compliant, resonant running robot at insect scale,” Tech. Rep., 2019.
- [2] V. Radhakrishnan, “Locomotion: Dealing with friction,” *Proceedings of the National Academy of Sciences*, vol. 95, no. 10, pp. 5448–5455, May 1998, ISSN: 0027-8424. DOI: 10.1073/pnas.95.10.5448.
- [3] J. B. Hopkins and M. L. Culpepper, “Synthesis of multi-degree of freedom, parallel flexure system concepts via Freedom and Constraint Topology (FACT) – Part I: Principles,” *Precision Engineering*, vol. 34, no. 2, pp. 259–270, Apr. 2010, ISSN: 01416359. DOI: 10.1016/j.precisioneng.2009.06.008.
- [4] J. Hopkins, “Synthesis through Freedom and Constraint Topologies,” in *Handbook of Compliant Mechanisms*, Oxford, UK: John Wiley & Sons Ltd, Feb. 2013, pp. 77–92. DOI: 10.1002/9781118516485.ch6.